THESIS

LATENT HEATING AND AEROSOL-PRECIPITATION INTERACTIONS WITHIN MESOSCALE CONVECTIVE SYSTEMS

Submitted by

Peter James Marinescu

Department of Atmospheric Science

In partial fulfillment of the requirements

For the Degree of Master of Science

Colorado State University

Fort Collins, Colorado

Spring 2016

Master's Committee:

Advisor: Susan C. van den Heever
Co-Advisor: Sonia M. Kreidenweis

Richard Eykholt
Russ S. Schumacher

ABSTRACT

LATENT HEATING AND AEROSOL-PRECIPITATION INTERACTIONS WITHIN MESOSCALE CONVECTIVE SYSTEMS

Two studies are presented in this thesis that focus on understanding cloud processes within simulations of two mesoscale convective system (MCS) events that occurred during the Midlatitude Continental Convective Clouds Experiment (MC3E). Simulations are conducted with the Regional Atmospheric Modeling System (RAMS) and are compared with a suite of observations obtained during MC3E. It is concluded that the simulations reasonably reproduce the two MCS events of interest. Both studies provide information that can assist in the advancement of cloud process parameterizations in atmospheric models.

The first study details the microphysical process contributions to latent heating profiles within MCS convective and stratiform regions and the evolution of these profiles throughout the MCS lifetime. Properly representing the distinctions between the latent heating profiles of MCS convective and stratiform regions has significant implications for the atmospheric responses to latent heating on various scales. The simulations show that throughout the MCSs, condensation and deposition are the primary contributors to latent warming, as compared to riming and nucleation processes. In terms of latent cooling, sublimation, melting, and evaporation all play significant roles. Furthermore, it is evident that throughout the MCS lifecycle, convective regions demonstrate an approximately linear decrease in the magnitudes of latent heating rates, while the evolution of latent heating within stratiform regions is associated with transitions between MCS flow regimes.

The second study addresses the relative roles of middle-tropospheric and lower-tropospheric aerosol particles on MCS precipitation during the mature stage. A suite of sensitivity simulations for each MCS event is conducted, where the simulations are initialized with different aerosol profiles that vary in the vertical location of the peak aerosol particle number concentrations. Importantly, the total integrated aerosol mass remains constant between the different initialization aerosol profiles, and therefore, differences between the simulated MCS precipitation characteristics can be more directly attributed to the varied vertical location of the aerosol particles**.** The simulations from both MCS events demonstrate that during the mature stage, the concentrations of lower-tropospheric aerosol particles are the primary factor in determining the intensity of precipitation near the cold pool leading edge, while middle-tropospheric aerosol particles were entrained within convective updrafts, thus altering the cloud droplet properties. However, the aerosol effects on total surface precipitation is not consistent between the two simulated MCS events, suggesting that the MCS structure and environmental conditions play important roles in regulating the impacts of middle-tropospheric and lower-tropospheric aerosol particles on MCS precipitation. Lastly, changes in precipitation processes can result in dynamical feedbacks that further modify, and hence complicate, the net effect of aerosol particles on MCS precipitation. One such feedback process involving the MCS cold pool intensity and updraft tilt is discussed.

ACKNOWLEDGEMENTS

There are many people who have been instrumental to the completion of this document. First, I would like to the thank my advisors, Dr.'s Susan van den Heever and Sonia Kreidenweis for the opportunity to pursue this research at Colorado State University. Their insights, encouragement, and guidance have been made me a better researcher, and their patience throughout the process has been greatly appreciated. They have both taught me a great deal from specific details about the science we study to universal life lessons, and I am grateful for this. I would also like to thank Stephen Saleeby for working closely with me on this research and assisting me with the model simulations and Dr. Paul DeMott for his assistance in determining ice nuclei concentrations used in the simulations. Susan van den Heever, Stephen Saleeby, Sonia Kreidenweis, and Paul DeMott are co-authors on the work presented here, and I would like to thank them all for their suggestions throughout this process. I am also grateful to Dr. Russ Schumacher and Dr. Richard Eykholt for their time, flexibility, and efforts as my Master's Committee members. I would also like to acknowledge Dr. Brenda Dolan and Alyssa Matthews for providing me with radar data from the Midlatitude Continental Convective Clouds Experiment that was used in Chapter 2 of this thesis.

The van den Heever and Kreidenweis research groups have also been boundless resources from which I have learned a great deal throughout this process, and I would like to thank all the members of these two groups, both past and present. I would especially like to acknowledge Leah Grant, Adele Igel, Aryeh Drager, and Stephen Saleeby, who have all spent a great deal of time thinking through problems with me, giving me excellent advice, being patient with my countless questions, and simply being there for me on the day-to-day.

As I switched careers, moved across the United States, and ventured into an area that was relatively unknown to me, my family and friends have always supported me and given me the strength to pursue my dreams. I would especially like to acknowledge my grandparents, Emilia and Mircea Marinescu and Laura and Dorian Costin, my parents, Radu and Michaela Marinescu, my brother, Mark Marinescu, and my girlfriend, Leah Grant – without their examples and sacrifices, I would not be where I am today.

The research presented in this document was financially supported by the Department of Energy, under grant DE-SC0010569, the National Science Foundation Science and Technology Center for Multi-Scale Modeling of Atmospheric Processes (CMMAP), managed by Colorado State University under cooperative agreement No. AGS-0425247, and the American Meteorological Society's graduate fellowship program.

TABLE OF CONTENTS

Abstract ii

Acknowledgements iv

Chapter 1: Introduction 1

Chapter 2: The Microphysical Contributions to and Evolution of Latent Heating Profiles in Two MC3E Mesoscale convectice systems 5

2.1 Introduction 5

2.2 Case Overviews 9
2.2.1. 20 May 2011 Event 9
2.2.2. 23-24 May 2011 Event 11

2.3 Data 13
2.3.1. Simulations 13
2.3.2. Observations 17
2.3.2.1. Precipitation 17
2.3.2.2. Convective Updraft Strength 17
2.3.2.3. MCS Cloud Regions 18

2.4 Simulation-Observation Comparisons 18
2.4.1. Precipitation 18
2.4.2. Convective Updraft Strength 20
2.4.3. MCS Cloud Regions 22

2.5 Regional Microphysical Process Contributions to Latent Heating 25
2.5.1. Convective (CONV) Regions 26
2.5.2. Stratiform (STRA) Regions 28
2.5.3. Anvil (ANVL) Regions 29

2.6 Time Evolution of Latent Heating 30
2.6.1. Convective (CONV) Regions 33
2.6.2. Stratiform (STRA) Regions 37
2.6.3. Anvil (ANVL) Regions 40

2.7 Conclusions and Implications 40

Chapter 3: The Relative Roles of Middle- and Lower-Tropospheric Aerosol on Mature MCS Precipitation Rates 45

3.1 Introduction 45

3.2 Experimental Design 50
3.2.1. Model Description 50
3.2.2. Aerosol Sensitivity Profiles 52
3.2.3. Cross Section Analysis 55

3.3 MCS Event on 20 May 2011 57
3.3.1. Precipitation Cross Section 57
3.3.2. Initial Convective Cells 58
3.3.3. Convective Updrafts 60
3.3.4. Stratiform and Convective Precipitation Processes 62
3.3.5. Cold Pool Feedbacks 66

3.4 Comparisons to the 23-24 May 2011 event 71

3.5 Conclusions 76

Chapter 4: Concluding Remarks 80

4.1 Main Conclusions 80

4.2 Applications 83

4.3 Future Work 84

References 87

CHAPTER 1: INTRODUCTION

From 22 April through 6 June 2011, the Midlatitude Continental Convective Clouds Experiment (MC3E) transpired in the south central United States [*Jensen et al.*, 2015]. This field campaign was jointly led by the U.S. Department of Energy's Atmospheric Radiation Measurement Program and the National Aeronautics and Space Administration and utilized both remote sensing and in-situ measurement platforms. One of the primary goals of MC3E was to improve the representation of convective clouds within models that use a variety of microphysical parameterizations to represent cloud-scale processes.

Convective clouds fall into a spectrum from isolated convective cells (~1 km in the horizontal scale) to expansive mesoscale convective systems (~100s-1000 km in the horizontal scale). On the high end of this size spectrum, mesoscale convective systems (MCSs) often evolve from individual convective cells that amalgamate and grow upscale into these large cloudy areas. MCSs also are typically organized with convective and stratiform regions, and this organization is frequently maintained for over six hours. *Fritsch and Forbes* [2001], *Houze* [2004], and *Cotton et al.* [2011] provide comprehensive reviews of MCSs.

MCSs can significantly impact both local and global weather and climate due to their large sizes and long lifetimes. On a global scale, MCSs have been shown to be one of the most important weather systems in terms of vertically redistributing air, heat, and moisture from the surface to the upper troposphere, which has significant implications for Earth's energy and hydrological cycles [*Cotton et al.*, 1995]. Properly representing the structure and intensity of convection within MCSs has been shown to impact global scale circulations [*Hartmann et al.*, 1984; *Schumacher et al.*, 2004]. Furthermore, *Nesbitt et al.* [2006] demonstrated that MCS

precipitation is the major component of tropical rainfall globally. MCSs also play very important roles in local weather and climate. In the central United States, where MC3E occurred, MCSs have been observed to produce the majority of warm season precipitation [*Fritsch et al.*, 1986], as well as various types of severe weather [e.g., *Houze et al.*, 1990; *Tollerud and Collander*, 1993].

Simulating and predicting MCSs and their effects on the Earth system have been challenging [*Fritsch and Carbone*, 2004; *Zhang and Song*, 2009; *Del Genio et al.*, 2012]. Since the computations associated with simulating atmospheric processes over large model domain sizes are costly, most global operational models and global climate models (GCMs) have been unable to explicitly resolve convective clouds due to large grid spacings. These models have relied upon convective parameterizations to represent convective cloud processes. Such parameterization schemes use prognosed large-scale conditions to determine regions where convection should exist and then, diagnose the effects of moist convection based on predetermined relationships. However, convective parameterizations cannot represent the evolving organization of MCSs (e.g., the development of a stratiform rain region), which requires additional prognosed variables [*Davis et al., 2003; Futyan and Del Genio*, 2007; *Del Genio et al.*, 2012]. Although advancements in computing and innovations in model development have allowed for some global-scale, convection-allowing simulations that do not require convective parameterizations [e.g., *Randall et al.,* 2003; *Satoh et al.*, 2008], these global-scale simulations are computationally expensive and have certain limitations. Therefore, there is an ongoing need to better represent MCSs with convective parameterizations within these large-scale modeling frameworks. To better evaluate, constrain, and further develop model parameterizations, observations are needed with which simulations can be compared and

substantiated as properly reproducing the phenomena of interest. With such observations, parameterizations can also be tested and adjusted appropriately.

Two well-observed MCS events that occurred on 20 May 2011 and 23-24 May 2011 during MC3E are simulated with the Regional Atmospheric Modeling System [RAMS; *Myers et al.*, 1997; *Cotton et al.*, 2003; *Saleeby and Cotton*, 2004; *Saleeby and van den Heever*, 2013]. Both events produced an MCS with a leading convective line and trailing stratiform region (LLTS), which is the most common type of MCS in the central United States [*Houze et al.*, 1990; *Parker and Johnson*, 2000]. Detailed descriptions of the two events and simulation-observation comparisons are provided in Chapter 2. Studying the same features and relationships using two separate MCS events gleans information about the generality of the results found in this research. Using these simulations, two aspects of MCS cloud processes, 1) latent heating and 2) aerosol-cloud interactions, are examined in this thesis.

In Chapter 2, latent heating microphysical process budgets for the two MCS events are presented. These microphysical budgets are related to the current MCS conceptual model, and this comparison can be used to evaluate and further develop the RAMS microphysical parameterization. The evolution of latent heating with MCS lifecycle is also reported and quantified from the model simulations, which can assist in the development of convective parameterizations that incorporate mesoscale organization (i.e., MCS convective and stratiform regions). Chapter 2 of the thesis has been submitted for publication to the *Journal of Geophysical Research*.

The relative roles of cloud-nucleating aerosol particles in the lower and middle troposphere on MCS precipitation processes are explored in Chapter 3. There are abundant measurements of aerosol particles at the surface [e.g., *Holben et al.*, 1998], as compared to the

free troposphere, where aerosol particles are frequently transported from distant sources [e.g., *Berg et al.*, 2016]. As the parameterizations of aerosol-cloud interactions continue to be augmented and improved in both CRMs and GCMs [*Tao et al.*, 2012], an understanding of the relative importance of upper troposphere aerosol particles on cloud systems will be useful for further model development. Chapter 3 of this thesis is being prepared for submission to the *Journal of the Atmospheric Sciences.*

Both latent heating and aerosol-cloud interactions are atmospheric processes that are extremely challenging to directly observe, and therefore, CRM simulations have been used to provide much of the current understanding of these processes. Collectively, Chapters 2 and 3 of this thesis examine two CRM simulations with the goals of augmenting the knowledge of latent heating and aerosol-cloud interactions within MCSs and providing useful data that can benefit the development of cloud process parameterizations.

CHAPTER 2: THE MICROPHYSICAL CONTRIBUTIONS TO AND EVOLUTION OF LATENT HEATING PROFILES IN TWO MC3E MESOSCALE CONVECTIVE SYSTEMS

2.1 Introduction

The vertical structure of latent heating within midlatitude, continental mesoscale convective systems (MCSs) has been shown to vary between convective and stratiform regions by both observational [*Kuo and Anthes*, 1984; *Gallus and Johnson*, 1991] and modeling [*Tao et al.*, 1993] studies. Convective regions have latent warming (i.e., positive latent heating) throughout the majority of the vertical profile and more intense latent warming rates than stratiform regions. Stratiform regions tend to have latent warming above and latent cooling (i.e., negative latent heating) below a mid-tropospheric cloud base [Fig. 4a in *Houze*, 2004].

The distinction between the shape and magnitude of midlatitude, continental MCS convective and stratiform latent heating profiles has important implications over a range of temporal and spatial scales. For example, on the synoptic scale, the vertical location and magnitude of latent heating can play a significant role in the enhancement of upper-tropospheric jet winds [*Wolf and Johnson*, 1995; *Hamilton et al.*, 1998], the development of mesoscale convective vortices (MCVs) that can persist for days and generate new convection [*Zhang and Fritsch*, 1987; *Rogers and Fritsch*, 2001], and the formation and propagation of synoptic-scale troughs that can impact downstream weather forecasting [*Stensrud and Anderson*, 2001; *Rodwell et al.,* 2013].

Idealized numerical experiments have shown that latent heating and its induced buoyancy perturbations create gravity waves that propagate outward from their source and force regions of

enhanced rising and sinking motions [*Bretherton and Smolarkiewicz*, 1989]. *Nicholls et al.* [1991] further reported that the shape and magnitude of the vertical profiles of heating in both convective and stratiform regions impact gravity wave propagation speeds, as well as the environmental response to the gravity waves (i.e., perturbations to horizontal wind, vertical wind, pressure, and buoyancy). These changes to the mesoscale environment can consequently alter MCS behavior. For example, using a numerical simulation, *Adams-Selin and Johnson* [2013] demonstrated that latent heating-induced gravity waves resulted in increased pressure ahead of an MCS convective line, which assisted in forcing a bowing region. The vertical structure and magnitude of latent heating are also critical to a variety of internal MCS processes, including the development of the mesoscale circulation within the MCS [e.g., *Raymond and Jiang*, 1990; *Pandya et al.*, 1996] and the propagation of the MCS [e.g., *Raymond*, 1984; *Cram et al.*, 1992].

Many of these latent-heating-dependent features are poorly reproduced in large-scale models that do not explicitly resolve the cloud processes that impact latent heating [e.g., *Hartman et al.*, 1984; *Davis et al.*, 2002; *Schumacher et al.*, 2004]. While several convective parameterizations have been developed to account for the different processes associated with MCS convective and stratiform regions [*Donner,* 1993; *Alexander and Cotton*, 1998; *Donner et al.*, 2001], few have been incorporated into large-scale models. Further, these parameterizations do not incorporate the time evolution of MCS processes, which has been argued to be important for the improvement of parameterization results [*Futyan and Del Genio*, 2007; *Del Genio et al.*, 2012].

One obstruction to the understanding and parameterization of MCS latent heating and its time evolution is the inability of current observing platforms to directly obtain latent heating

rates, although observations, such as those from rawinsondes and radars, can been used in conjunction with simplifying assumptions to diagnose estimated heating rates [*Yanai et al.*, 1973]. Using this diagnostic analysis, early studies disentangled MCS stratiform latent heating from its convective counterpart in tropical MCSs [*Leary and Houze*, 1979; *Johnson and Young*, 1983], and midlatitude, continental MCSs [*Kuo and Anthes*, 1984; *Gallus and Johnson*, 1991; *Braun and Houze*, 1996]. These studies, and others that have focused on the kinematics of MCSs [e.g., *Smull and Houze*, 1985], have provided numerous insights into MCS processes and corroborated the general shapes of the idealized convective and stratiform latent heating vertical profiles, as shown in *Houze* [2004]. Collectively they have shown that convective region latent warming is primarily driven by condensational growth within updrafts and that it peaks in the middle-to-upper troposphere. Hydrometeors are advected from the convective regions into the developing stratiform regions, where depositional growth onto ice hydrometeors dominates latent heating production above the stratiform cloud base. As ice hydrometeors precipitate, sublimation, evaporation, and melting all appear to play important roles in creating a latent cooling peak below the stratiform cloud base.

While a few of these studies were able to diagnose estimated latent heating rates at a few times during a specific MCS event [*Gallus and Johnson*, 1991; *Braun and Houze*, 1996], they were unable to fully resolve the evolution of MCS latent heating. Furthermore, estimates of convective region latent heating from many observation-based studies are susceptible to aliasing biases, as the spatial sampling of observations is typically too coarse for the calculation of the finer scale processes within the convective region. Some of these issues have been resolved with increased radar observations [*Braun and Houze*, 1996]. For these reasons, the time evolution of MCS latent heating may currently best be studied using cloud resolving model (CRM)

simulations, provided the simulations can reasonably reproduce MCS events. Furthermore, should the simulations be reasonably accurate, CRMs can then provide details regarding the microphysical processes related to latent heating. However, relatively few modeling studies [e.g., *Tao et al.*, 1993; *Caniaux et al.*, 1994] have focused on the evolution of latent heating within MCS convective and stratiform regions.

Satellites have also been used to estimate latent heating rates within MCSs. The Tropical Rainfall Measurement Mission [TRMM; *Simpson et al.*, 1988] increased the spatial and temporal extent of latent heating estimation in tropical regions, and the Global Precipitation Measurement [GPM; *Hou et al.*, 2014] is now extending these estimates to the mid-latitudes. Many TRMM latent heating retrieval algorithms have been developed, all of which are rooted in data from CRM simulations [*Tao et al.*, 2006; *Shige et al.*, 2009]. Advancements in computing power have allowed recent CRM simulations to better reproduce many features of MCSs, due to the use of more sophisticated microphysics parameterizations [*Morrison et al.*, 2009; *Li et al.*, 2009; *Adams-Selin et al.*, 2013; *Lang et al.*, 2014]. A renewed and enhanced focus on understanding CRM simulations of MCS latent heating would thus be useful for algorithm improvements in satellite applications.

The goals of this study are therefore (1) to assess the microphysical process contributions to latent heating profiles within MCS regions and (2) to evaluate the time evolution of latent heating within MCS regions. These goals are accomplished through conducting CRM simulations of two MCS events that occurred during the Midlatitude Continental Convective Clouds Experiment [MC3E; *Jensen et al.*, 2015]. From 22 April through 6 June 2011, the National Aeronautics and Space Administration (NASA) and the Department of Energy (DOE) collaborated on MC3E, which transpired in the Southern Great Plains of the United States. One

of the major goals of the field project was to provide details of the physical processes that drive convective clouds [*Jensen et al.*, 2015]. Two of the best-sampled events occurred on 20 May 2011 and 23-24 May 2011, both of which involved an MCS with a leading convective line and trailing stratiform precipitation region (LLTS), the most common MCS type in the central United States [*Parker and Johnson*, 2000]. These MC3E MCS events have been the focus of numerous studies on various aspects of convection [*Tao et al.*, 2013; *Lang et al.*, 2014; *Fan et al.*, 2015; *Liu et al.*, 2015]. Summaries of these two MCS events are provided next with a more in-depth analysis of the May 23-24 event, since there has been less focus on this event in the current literature.

2.2 Case Overviews

2.2.1. 20 May 2011 Event

During the early morning hours of 20 May 2011, a linear MCS traversed eastward across southern Kansas, Oklahoma, and northern Texas. Between the hours of 0600 UTC and 1800 UTC (Fig. 2.1a-d), localized rainfall rates of over 2 inches per hour were observed. Convection initiated around 0300 UTC (not shown) along a dryline in western OK and TX and grew upscale into an LLTS MCS. Around 1000 UTC (Fig. 2.1b), the leading convective line assumed a bowing structure, and new convective cells began to initiate several hundred kilometers ahead of the leading convective line. The MCS continued to move eastward across OK (Fig. 2.1c) and weakened when entering Arkansas around 1800 UTC (Fig. 2.1d). At this time, the convective line began to break apart, losing its continuous region of high radar reflectivities. From 0300 UTC through 1800 UTC, this system produced in excess of 1 inch of accumulated precipitation over the majority of OK and the surrounding regions. Around 1800 UTC, a second linear MCS

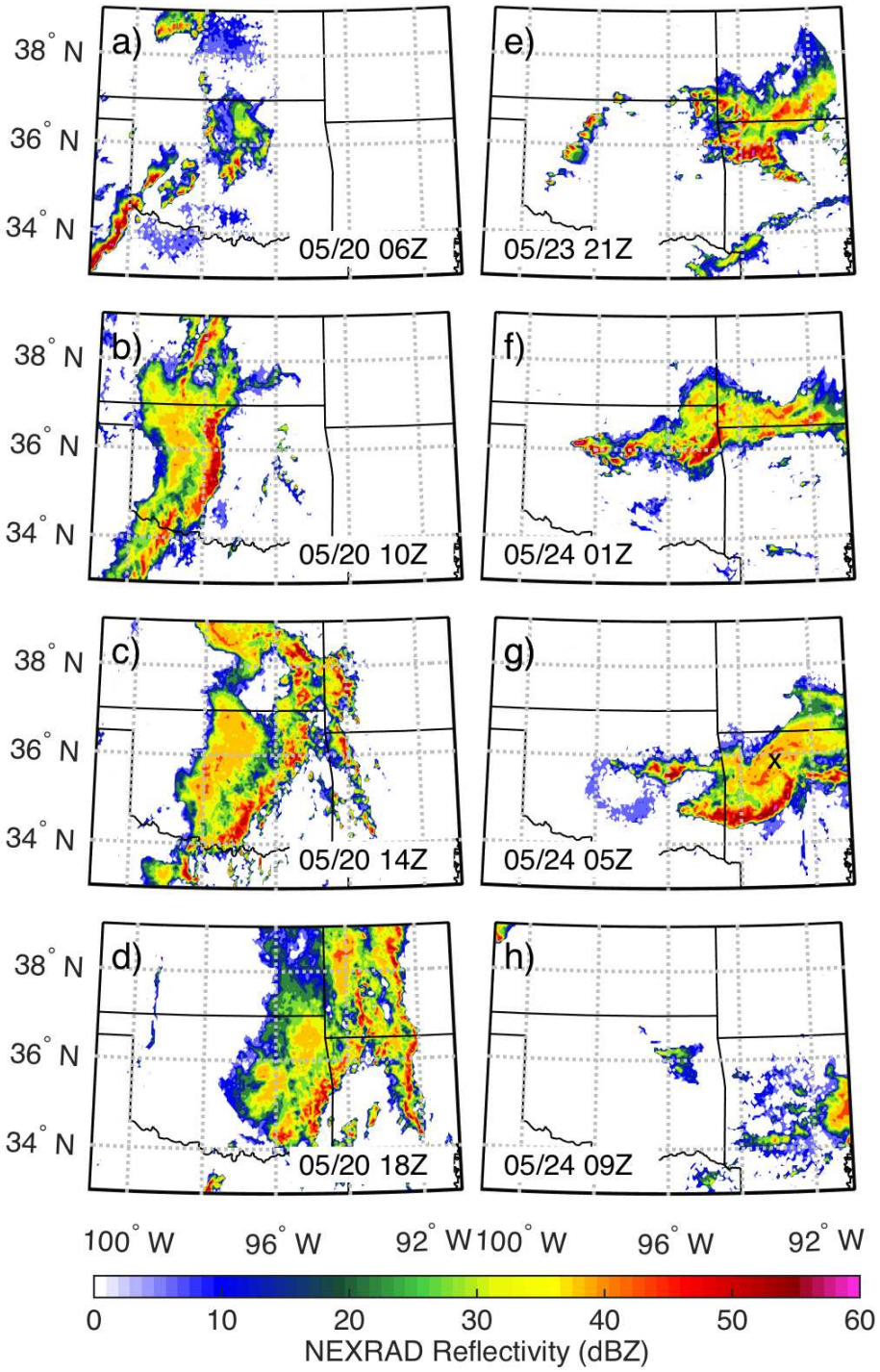

Figure 2.1. Next-Generation Weather Radar (NEXRAD) radar reflectivity (dBZ) at 2.5 km AGL for the two MCS events of interest. (a-d) represent data from 20 May 2011 at 0600 UTC, 1000 UTC, 1400 UTC, and 1800 UTC, respectively. (e-h) represent data from 23-24 May 2011 event at 2100 UTC, 0100 UTC, 0500 UTC, and 0900 UTC, respectively. The "x" in (g) represents the approximate location of a bookend vortex.

developed in southern OK and northern TX, immediately behind the MCS described above. This second MCS quickly grew upscale and merged with the decaying, original MCS in the hours following 1800 UTC (not shown). For this reason, the decaying stage of this MCS event was not easily assessed in both the observational and simulation datasets. Descriptions of the synoptic precursors and additional mesoscale features of this event are provided in *Tao et al.* [2013] and *Lang et al.* [2014].

2.2.2. 23-24 May 2011 Event

At 23 May 2011 2000 UTC, individual thunderstorms began forming in west-central Oklahoma along a dryline (Fig. 2.1e). A weak short -wave trough (Fig. 2.2a) and strong diurnal heating near the dryline (Fig. 2.2b,c) helped to initiate this storm development. These initial storms produced severe hail and several tornadoes in central OK according to data published by the National Oceanic and Atmospheric Administration's Storm Prediction Center (SPC Reports, retrieved from http://www.spc.noaa.gov/climo/reports/). The storms became more numerous in the following hours and edged eastward into central OK. At these early stages of the May 23-24 event, a separate MCS that formed the prior night was present in southern Missouri, northern Arkansas, and extreme northeast OK and southeast Kansas (Fig. 2.1e).

In the evening hours of 23 May 2011, the southern dryline storms dissipated, but the northernmost dryline storms, which were more widespread, were sustained through continued development of convection along outflow boundaries. This northern region of dryline storms merged with the pre-existing MCS in the southern MO region around 24 May 0100 UTC (Fig. 2.1f). An intensifying south-southwesterly low-level jet (LLJ), whose most intense branch was in eastern OK and western AR (Fig. 2.2b), as well as strong outflow boundaries from this merged

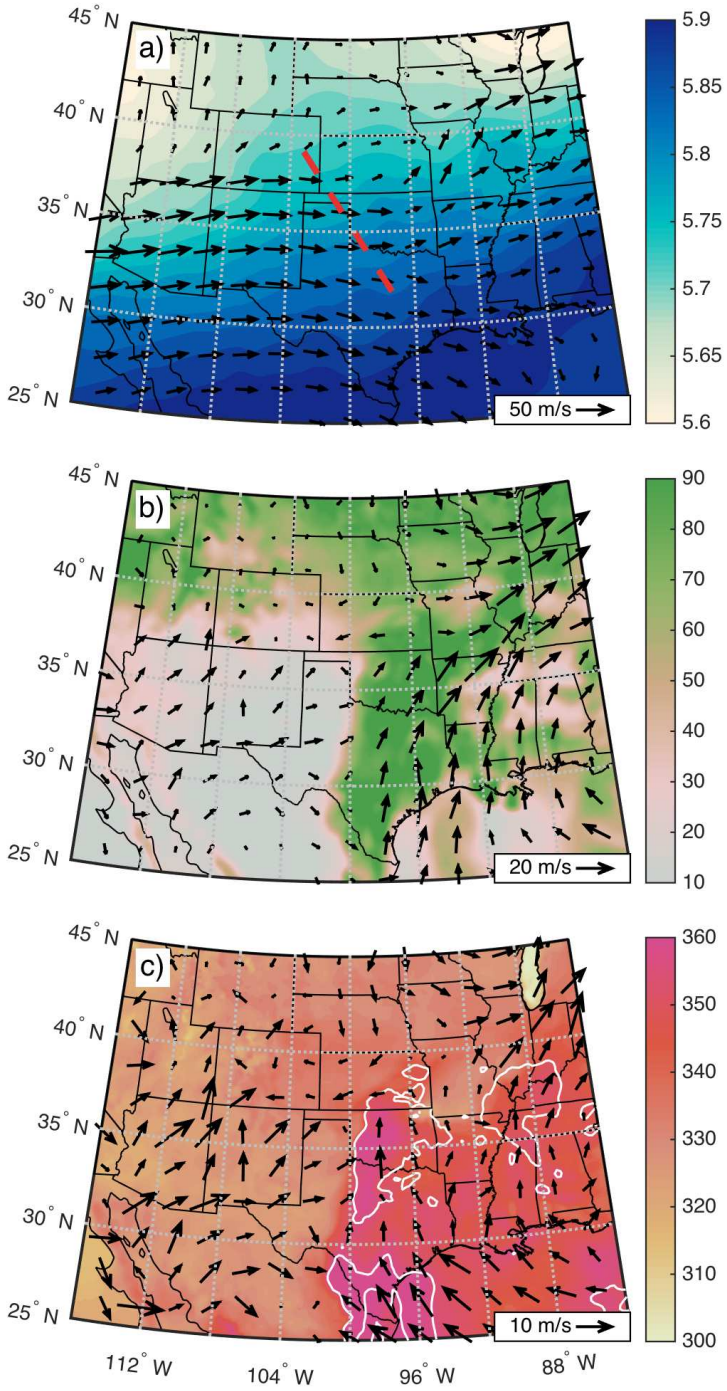

Figure 2.2. Synoptic-scale conditions at 2000 UTC on 23 May 2011 from the Rapid Update Cycle model/analysis. (a) represents 500 hPa geopotential heights (gpkm) and 300 hPa wind vectors. (b) represents 850 hPa relative humidity (%) and 850 hPa wind vectors. (c) represents near-surface equivalent potential temperature and near-surface wind vectors. Red, dashed line in (a) shows the approximate location of the short-wave trough. White contour in (c) denotes mixed layer convective available potential energy (MLCAPE) of 3000 J kg^{-1}.

region of precipitation, created a favorable environment for a southward propagating LLTS MCS [*Augustine and Caracena*, 1994].

By 24 May 0100 UTC, the strongest convection was located along the southern end of the MCS precipitation region, and this leading convective line began to propagate to the southeast (Fig. 2.1f,g). The region of stratiform rain extended hundreds of kilometers north and northeast of the convective line. This asymmetric, northeastward extension of stratiform rainfall remained throughout the lifetime of the MCS. During the next several hours, the convective line bowed

and a bookend vortex formed on the northeastern end of the leading convective line in west-central AR (Fig. 2.1g). During this time period, an ongoing severe wind event caused many reports of downed trees and power lines and roof damage along the convective line (SPC Reports). The MCS continued its southeastward propagation until ~0600 UTC. Around this time, the convective line began to dissipate in central AR. By 0900 UTC (Fig. 2.1h), mostly only light stratiform precipitation was present in central and eastern AR. 500 hPa absolute vorticity suggests that an MCV may have developed from the bookend vortex and asymmetric stratiform precipitation region (Fig. 2.1g) and assisted in initiating convection in Tennessee and Kentucky during the 1400-1800 UTC period on 24 May.

2.3 Data

2.3.1. Simulations

The May 20 and May 23-24 MCS events were simulated with the three-dimensional, non-hydrostatic Regional Atmospheric Modeling System [RAMS; *Cotton et al.*, 2003; *Saleeby and van den Heever*, 2013]. RAMS has successfully simulated the microphysical and dynamical

features of MCSs in many prior studies [e.g., *Olsson and Cotton*, 1997; *Alexander and Cotton*, 1998; *Cheng and Cotton*, 2004; *Seigel and van den Heever*, 2013; *Seigel et al*., 2013]. The RAMS microphysics scheme incorporates a bin-emulating, two-moment bulk cloud microphysical parameterization that tracks three liquid hydrometeor (cloud, drizzle, and rain) and five ice hydrometeor (graupel, hail, pristine ice, snow, and aggregates) species [*Meyers et al.,* 1997; *Saleeby and Cotton*, 2004].

In order to appropriately account for the synoptic conditions while still being able to simulate cloud-scale processes, the simulations were set up with three nested grids with horizontal grid spacings of 30 km, 6.0 km, and 1.2 km (Fig. 2.3). All of the simulation analysis was performed over a subset of grid 3 ("analysis domain" in Fig. 2.3), which was approximately bounded by 33°N, 38°N, 101°W, and 90°W, as the overwhelming majority of both MCSs fell within this bounding box (compare Fig. 2.1 and Fig. 2.3). The model domain was constructed

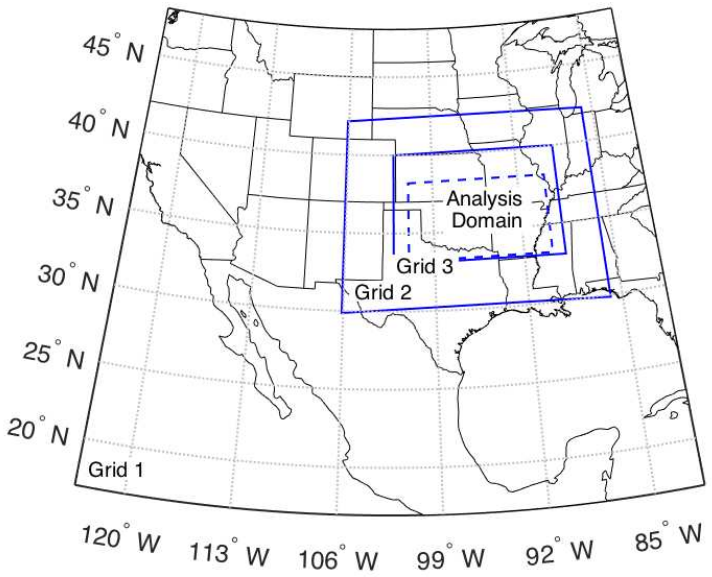

Figure 2.3. Map of the nested grids used in the RAMS simulations. Grids 1, 2, and 3 have horizontal grid spacing of 30 km, 6 km and 1.2 km, respectively. A subset of Grid 3 ("Analysis Domain") is used for all analyses presented herein.

with 60 vertical levels that were spaced 75 m apart near the surface and were stretched to 500 m by 4 km above ground level (AGL), at which point the vertical spacing remained constant to the model top at 22 km AGL.

Both simulated events were initialized several hours before the observed initiation of the convective cells that grew upscale into their respective MCSs. The May 20 simulation was initialized with the Global Data Assimilation System (GDAS-FNL) re-analysis data from 20 May 2011 0000 UTC. Due to weaker synoptic forcing associated with the May 23-24 event, as well as the presence of mesoscale features that were essential to the development of the MCS, the higher-resolution Rapid Update Cycle (RUC) model analysis data from 23 May 2011 1600 UTC was used to initialize the May 23-24 simulation. The GDAS-FNL and RUC analysis data also provided the lateral boundary conditions for the May 20 and May 23-24 simulations, respectively. The simulations were initialized with horizontally-homogeneous aerosol profiles that were based on surface measurements from the DOE's Atmospheric Radiation Measurement Program's Southern Great Plains site (ARM-SGP; 36.6^{o}N, 97.5^{o}W) at the onset of the May 20 and May 23-24 events. These profiles were formulated with aerosol particle number concentrations of 2000 cm^{-3} at the surface, and this concentration was exponentially decreased with a scale height of 7 km to the model top. These aerosol particles can serve as cloud condensation nuclei (CCN), and the number of particles activated is based on predicted environmental conditions [*Saleeby and van den Heever*, 2013]. Ice nuclei profiles were also horizontally homogenized throughout the model domain and were based on MC3E aircraft observations of number concentrations of particles with diameters larger than 500 nm. For the May 20 event, this aerosol initialization (2000 particles cm^{-3} at the surface) differs from simulations in *Fan et al.* [2015], which used much cleaner surface conditions (320 particles

cm^{-3}), as their initialization data were based on CCN observations taken after the influence of convection and precipitation at the ARM-SGP site.

RAMS prognoses the mixing ratio and number concentration of all hydrometeor species and provides output of the rates of microphysical processes (e.g., melting, riming, nucleation) and latent heating [*Saleeby and van den Heever*, 2013]. These microphysical processes are critical for understanding the evolution of latent heating throughout the two simulations. Analysis of the MCSs encompasses a 12-hour period ("analysis period") with model output every 5 minutes, beginning with the initial convective cell development, which occurs at approximately 20 May 0300 UTC and 23 May 2100 UTC for the May 20 and May 23-24 events, respectively. A summary of the simulation configurations is provided in Table 2.1.

Table 2.1. Summary of RAMS configurations and options.

Model aspect	Setting
Grid	Arakawa C grid [*Mesinger and Arakawa*, 1976] 3 nested grids: Grid 1: $\Delta x = \Delta y = 30$ km, $\Delta t = 30$ s, (130x105x60 grid points) Grid 2: $\Delta x = \Delta y = 6$ km, $\Delta t = 7.5$ s, (302x227x60 grid points) Grid 3: $\Delta x = \Delta y = 1.2$ km, $\Delta t = 3.8$ s, (997x647x60 grid points) Δz = variable (details provided in Section 2.3.1) Model top at ~22 km AGL
Initialization	GDAS-FNL re-analysis data for May 20 event RUC model analysis data for May 23-24 event Aerosol initialization described in Section 2.3.1 and based on MC3E data
Microphysics scheme	Two-moment bulk microphysics for eight hydrometeor species [*Meyers et al.*, 1997; *Saleeby and Cotton*, 2004]
Boundary conditions	Radiative lateral boundary [*Klemp and Wilhelmson*, 1978]
Cumulus parameterization	Kain-Fritsch scheme [*Kain and Fritsch*, 1993] only on Grid 1
Radiation scheme	*Harrington* [1997]
Turbulence scheme	Horizontal diffusion based on *Smagorinsky* [1963]; Vertical diffusion based on *Mellor and Yamada* [1974]
Land-surface model	LEAF-3 [*Walko et al.*, 2000]

2.3.2. Observations

A combination of satellite and surface-based measurements was used to ensure that the RAMS simulations produced MCS events similar to those observed during the MC3E field campaign. Three MCS features were selected for model evaluation and comparison: precipitation, convective updraft strength, and MCS convective, stratiform, and anvil cloud areas.

2.3.2.1. Precipitation

The National Center for Environmental Prediction's National Stage IV QPE Product (ST4) was used for the precipitation validation. This dataset uses both radar and gauge data to produce quantitative precipitation amounts on an hourly basis across the United States [*Lin and Mitchell*, 2005]. This dataset was provided on a 4 km, polar stereographic grid.

2.3.2.2. Convective Updraft Strength

During MC3E, multiple radars were strategically placed in order to retrieve information about vertical velocities (W) within convective systems [*Jensen et al.*, 2015]. Attenuation-correction and multi-Doppler techniques were used to determine W from integrating radial velocity vectors using the variational method as described in *Dolan and Rutledge* [2010]. Depending on the data availability, this analysis was conducted with data from 3 or 4 radars, including two X-band Scanning ARM Precipitation Radars (SAPR), one C-band SAPR, and a National Weather Service WSR-88D radar (KVNX). Errors in estimated W using this radial velocity integration have been shown to be on the order of several m s^{-1} [*Dolan and Rutledge*, 2010; *Collis et al.*, 2013]. Due to the limited ranges of the radars, these data were confined to a

120 x 120 km area centered at the ARM-SGP site. The quality-controlled data were mapped onto a 1.0 x 1.0 x 1.0 km grid at output intervals of ~5-15 minutes. This analysis was only available between ~0600 UTC and ~1000 UTC on 20 May 2011 and between ~2100 UTC and ~2400 UTC on 23 May 2011, which are both within the 12-hour analysis period of this study.

2.3.2.3. MCS Cloud Regions

The observed MCSs were separated into convective (CONV), stratiform (STRA), and anvil (ANVL) cloud regions. The major distinction between STRA and ANVL cloud regions is that STRA cloud regions have measureable precipitation at the surface. This observation-based MCS separation was done in a manner similar to that used in *Feng et al.* [2011; herein F11], which incorporates both the NEXRAD network data and the Geostationary Operational Environmental Satellite (GOES) satellite data.

2.4 Simulation-Observation Comparisons

2.4.1. Precipitation

For the precipitation comparisons, the RAMS simulation data were regridded to the ST4 grid using linear interpolation. In order to compare the temporal and spatial evolution of precipitation between the simulations and observations, Hovmöller diagrams were created within the analysis domain and are displayed in Figure 2.4. For the May 20 event (Fig. 2.4a,b), both the simulation and observation datasets showed initial convective development around 20 May 0600 UTC at 100^{o}W (Points 1 in Fig. 2.4), with eastward propagation of the precipitation. Furthermore, both the model and observations showed that the main MCS feature had its highest precipitation amounts between 1000 UTC and 1400 UTC between the longitudes of 98^{o}W and

96°W, followed by a slight decrease in precipitation amounts. RAMS also reproduced the convection forming ahead of the main convective line after 1200 UTC (Points 2). For the May 23-24 event (Fig. 2.4c,d), beginning around 2200 UTC, RAMS reproduced the location of precipitation associated with the dryline convection at 98°W (Points 3), as well as precipitation in the Missouri/Arkansas region between 94°W and 91°W (Points 4) at these earlier times. The main MCS precipitation feature formed around 0000 UTC (Points 5) in both the model and observations and propagated with an eastward component. To quantify the precipitation comparison, total accumulated precipitation was summed spatially across the analysis domain and temporally over the analysis period for both the simulation and observation datasets and

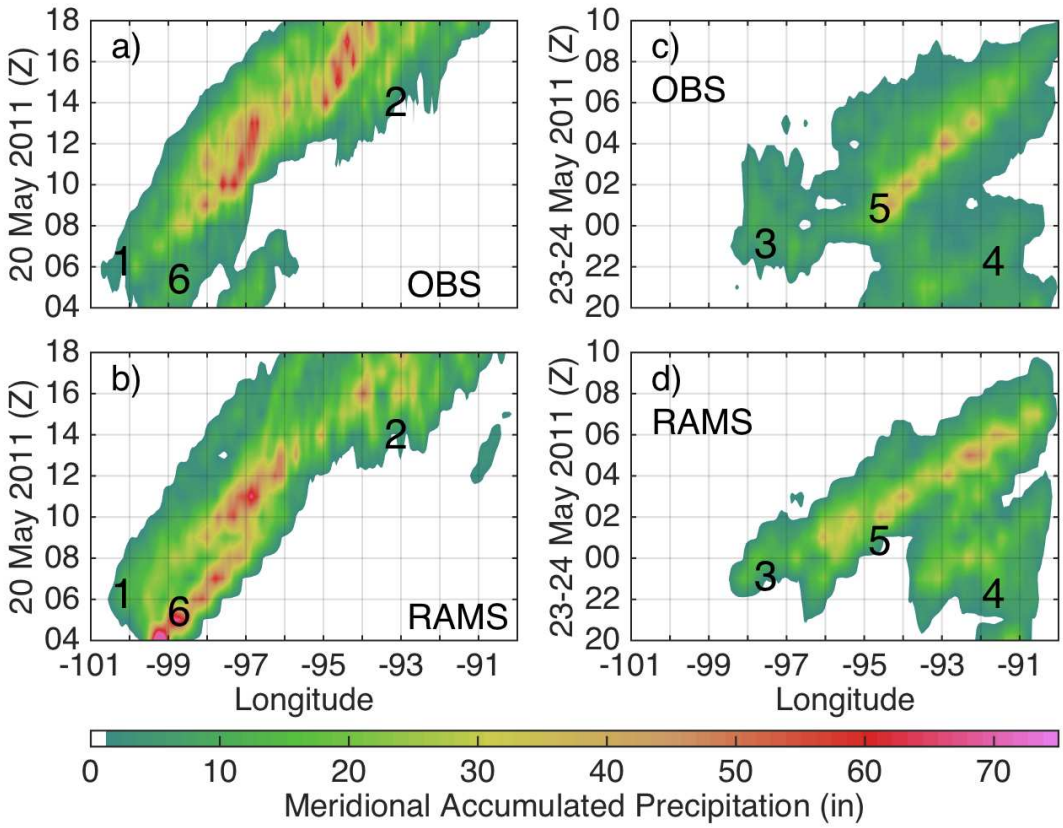

Figure 2.4. Time-longitude (Hovmöller) diagrams of meridionally summed (33°–38°N) accumulated precipitation for both the observations and RAMS model for the May 20 (a-b) and May 23-24 (c-d) events. Numbers represent corresponding key features during the MCS events, which are referenced in the text.

compared. Percentage differences of simulated domain-accumulated precipitation from observed values were -3.6% and +12.4% for the May 20 and May 23-24 events, respectively.

Some discrepancies between the simulations and the observations do appear in Figure 2.4. At the earliest times, both simulations formed too much precipitation in some regions (Points 4 and 6), before becoming more in keeping with observations once the MCSs developed. This precipitation intensity difference may be partly due to the lack of mesoscale information within the model initialization data and simulation spin-up. Another discrepancy that can be seen in Figure 2.4 is the simulations' underprediction of stratiform precipitation in the May 23-24 event. In spite of these shortfalls, the simulations do very well in reproducing most of the observed precipitation features for both events, both spatially and temporally.

2.4.2. Convective Updraft Strength

For comparisons, model W was gridded to the same vertical grid spacing as the radar data using linear interpolation. Since the convection in the simulations of both MCS events developed in a fashion (i.e., structure, timing, location) similar to observations, model data were confined to the same spatial area and temporal period as the available radar data. Convective cores were identified as three-dimensional connected regions of $W > 1$ m s^{-1} that had a depth of at least 6 km and started below the freezing level (~4 km AGL). Data from all defined convective cores were binned by altitude, and the 50^{th}, 75^{th}, and 95^{th} percentiles of convective core W were then calculated at each altitude level (Fig. 2.5). These methods are similar to other studies that have compared simulated MCS vertical velocities to radar-derived values [*Varble et al.*, 2014; *Fan et al.*, 2015].

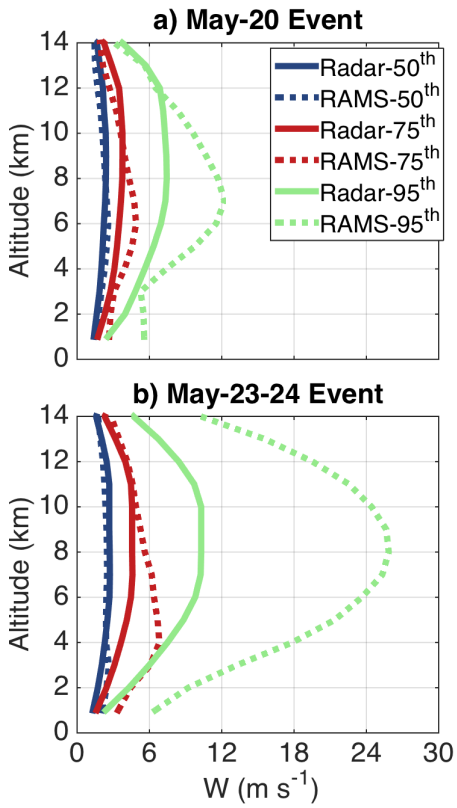

Figure 2.5. 50th, 75th, and 95th percentiles of vertical velocities within convective updrafts at each altitude level for the May 20 event (a) and for the May 23-24 event (b). Convective updrafts include all three-dimensionally connected grid points that have updrafts greater than 1 m s^{-1} and that span at least 6 km vertically, starting below the freezing level (4 km AGL).

For the relatively weak convective updrafts (50th percentiles in Fig. 2.5, blue lines), simulated vertical velocities were mostly within 0.3 m s^{-1} of the radar-derived values throughout the vertical column for both events. The differences between the 75th percentiles of the simulated and radar-derived vertically velocities (Fig. 2.5, red lines) were within ~1 m s^{-1} at all locations throughout the vertical column for both events, except between 1 and 6 km AGL for the May 23-24 event, where a mean overprediction bias of ~2 m s^{-1} occurred. With the strongest updraft velocities (Fig. 2.5, green lines), RAMS overpredicted W by at most 5 m s^{-1} and 16 m s^{-1} for the May 20 event and the May 23-24 event, respectively. Although the overprediction was larger for the May 23-24 event, the radar-derived vertical velocities for this event were also more intense than the May 20 event. A similar overprediction bias in the most intense, convective vertical

velocities has also been observed in recent simulations of both tropical and midlatitude MCSs [*Varble et al.*, 2014; *Fan et al.*, 2015]. Generally, convective W was well-captured in the RAMS simulations for the May 20 and May 23-24 events, except for overprediction biases during the May 23-24 event for the most intense updrafts.

2.4.3. MCS Cloud Regions

The observational data (i.e., NEXRAD and GOES) were broken down into convective (CONV), stratiform (STRA), and anvil (ANVL) regions, as defined in F11. While the ANVL region was further classified into thin, thick, and transitional regions by F11, this separation was not relevant to this study, and a broad ANVL area that encompasses the three ANVL subregions was used. Within the F11 algorithm, CONV and STRA regions were separated using a modified version of the radar-reflectivity-based methods used in *Steiner et al.* [1995]. The reflectivity threshold used was 43 dBZ, and the algorithm was implemented at 2.0 km altitude, which is well below the 0^{o}C isotherm level (~4 km AGL). The starting value for the reflectively difference over the background reflectivity for the peakedness criteria was changed from 10 dBZ to 20 dBZ in this study. Extensive testing demonstrated that this change lowered the frequency of stratiform regions being misclassified as convective for these two events.

In order to separate the simulation data into similar CONV and STRA regions, a convective-stratiform separation algorithm was used based on threshold values of precipitation rates, vertical velocities, and cloud mixing ratios similar to that used in many other studies [*Churchill and Houze*, 1984; *Tao et al.*, 1993; *Alexander and Cotton*, 1998]. A model column was determined to be CONV if one of the following criteria was met: (1) the instantaneous precipitation rate is greater than 25 mm hr^{-1}; (2) the absolute value of vertical velocity below the

melting level exceeds 3 m s^{-1}; (3) the absolute value of vertical velocity above the melting level exceeds 5 m s^{-1}; (4) the precipitation rate exceeds twice the background precipitation rate, which is computed from a 20 km^2 box surrounding the grid column; OR (5) cloud mixing ratios below the melting level are greater than 0.5 g kg^{-1}. Because this 5th criterion can sometimes misidentify thick, low-level stratiform clouds as CONV, it was specified that to be classified as CONV, model columns must have cloud tops above 6 km. All other precipitating grid columns – that is, grid columns with instantaneous hourly precipitation rates greater than a trace (0.254 mm) – were classified as STRA.

Simulation ANVL regions were also determined in a manner similar to F11. In F11, GOES data were used to capture the full anvil area by identifying locations with cloud tops greater than 6 km AGL, cloud bases greater than 3 km AGL, and cloud top infrared brightness temperature less than 270 K. In the RAMS simulations, the same thresholds were applied, except that cloud top temperature was used as a proxy for infrared brightness temperature. Cloud tops were determined as the highest level within a grid column with cloud mixing ratios greater than 0.1 g kg^{-1}. These cloud mixing ratio and temperature thresholds were tested amongst a range of reasonable values, and the total computed ANVL area was largely insensitive to threshold changes.

A snapshot of the CONV, STRA, and ANVL regions for both simulations and observations during the mature stage is provided in Figure 2.6. For the May 20 event, both the observation (Fig. 2.6a) and the simulation (Fig. 2.6b) datasets depicted an LLTS MCS oriented meridionally through central Oklahoma. ANVL regions spanned well to the east, west, and north of the main convective line. For the May 23-24 event, a similar LLTS MCS was present in both the observation (Fig. 2.6c) and the simulation (Fig. 2.6d) datasets. Despite simulating a smaller

region of stratiform precipitation directly behind the leading convective line, the RAMS simulation reproduced the asymmetric nature of the MCS, with a large region of stratiform precipitation, spanning northeastward from the main convective line.

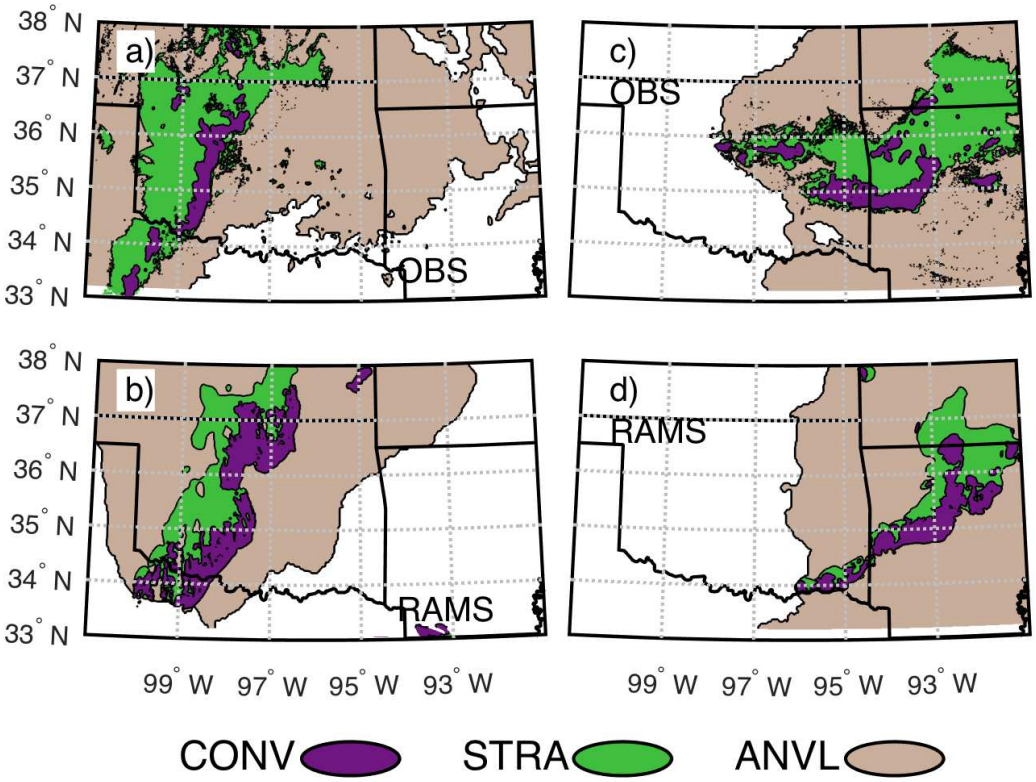

Figure 2.6. Maps of convective (CONV), stratiform (STRA), and non-precipitating anvil (ANVL) regions during the mature stages of both MCS events. (a-b) represent the observation-based and RAMS model classification for the May 20 event, respectively. (c-d) represent observation-based and RAMS model classification for the May 23-24 event, respectively.

Using precipitation, convective updraft strength, and MCS cloud regions, it has been demonstrated that, while there are some inconsistencies between the model output and the observations, the RAMS model was overall able to successfully reproduce many features of the two MC3E MCS events accurately, including their general development, evolution and propagation. Therefore, these simulations can be used to study the microphysical processes and the resulting latent heating structure associated with these two LLTS MCS events.

2.5 Regional Microphysical Process Contributions to Latent Heating

Figure 2.7 shows vertical profiles of temporally averaged, spatial means of latent heating rates (solid black lines) over the CONV, STRA, and ANVL regions, as well as the entire MCS for both simulations. These temporal averages were computed over the 12-hour analysis period, which began with the initial convective cell development for both events. The contributions to total latent heating arising from different microphysical processes are also shown (dotted and dashed lines). These microphysical processes are the net deposition-sublimation associated with existing ice hydrometeors (D-S), net condensation-evaporation associated with existing liquid hydrometeors (C-E), cloud droplet and ice crystal nucleation (NUC), melting of ice hydrometeors (MELT), and collection of liquid water by ice species (RIME). In this study, deposition refers to the growth of ice hydrometeors from water vapor, exclusively. Also shown in Figure 2.7 are the approximate cloud base heights for the convective regions (~1.2 km AGL for the May 20 event and ~1.8 km AGL for the May 23-24 event) and the freezing level heights within the MCSs (~3.7 km AGL for the May 20 event and ~3.9 km AGL for the May 23-24 event).

The magnitude and vertical structure of the microphysical processes and resulting latent heating are very similar between the two simulations, suggesting that results from this study may be applicable to other similarly structured midlatitude, continental MCSs. One of the only significant differences is that the May 23-24 CONV latent heating rates (Fig. 2.7e) are more intense than the May 20 event (Fig. 2.7a), although the vertical locations and relative distributions are similar. The more intense response in the May 23-24 event is due to stronger W, which is likely driven by differences in the environmental conditions. Mixed layer convective available potential energy (MLCAPE) values observed at the onset of the May 23-24 event were

~3000 J kg^{-1} (see Fig. 2.2) compared to ~2000 J kg^{-1} for the May 20 event. The model overprediction of the strongest W for the May 23-24 event may also be a contributing factor.

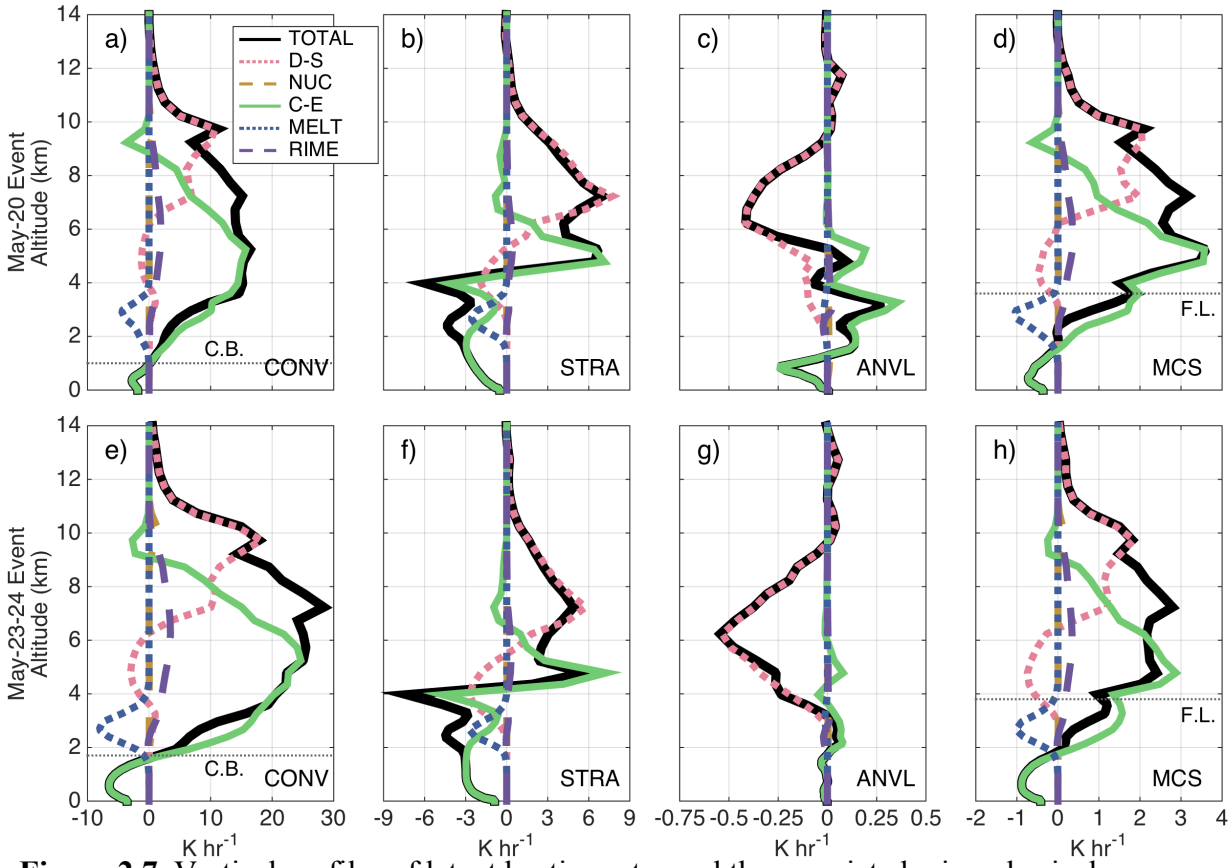

Figure 2.7. Vertical profiles of latent heating rates and the associated microphysical contributions. Key microphysical processes are descried in the text. Values shown are temporally averaged over the 12-hour analysis period and spatially averaged over classified MCS regions. (a-d) represent the CONV, STRA, ANVL, and entire MCS regions for the May 20 event. (e-h) represent the same regional and temporal averages for the May 23-24 event. Approximate cloud bases (C.B.) for convective regions are shown with dotted grey lines in (a) and (e). STRA and ANVL cloud bases are highly variable and are therefore not shown. Simulation freezing levels (F.L.) within the MCSs are indicated by the dotted grey lines in (d) and (h).

2.5.1. Convective (CONV) Regions

The CONV regions of both MCSs had net cooling below cloud base, which was caused by the evaporation of rain. From ~2 to 6 km AGL, latent warming from condensation was offset by latent cooling associated with the melting and sublimation of ice hydrometeors by up to 50%

and 10%, respectively. Between ~4 and 8 km AGL, net latent heating reached its peak levels, with mean heating rates of 15-30 K hr^{-1}. These altitudes of peak latent heating are similar to prior observational studies of midlatitude, continental MCSs [*Gallus and Johnson*, 1991; *Braun and Houze*, 1996]. Condensation was the primary driver of this warming through ~7-8 km AGL, above which vapor deposition onto ice played the dominant role. These simulations demonstrate that convective latent heating rates resulting from vapor deposition onto ice hydrometeors can almost reach the magnitude of latent heating resulting from condensational growth of liquid hydrometeors, although through a shallower layer. Around 9 km AGL, peak, net deposition-based warming and net evaporation-based cooling may represent the Wegener-Bergeron-Findeisen process. Riming produced mean latent warming rates of only 2-4 K hr^{-1} between 4 and 9 km AGL, though locally, the contribution of riming can be upward of 10 K hr^{-1} within hail cores (not shown). Nucleation had a negligible role in CONV latent heating, except near 10 km AGL, where homogeneous freezing of lofted cloud droplets was the dominant nucleation process.

Although the vertical locations of peak CONV latent heating were similar to prior observation-based, diagnostic studies [*Gallus and Johnson*, 1991; *Braun and Houze*, 1996], the magnitudes of latent heating (both warming and cooling) rates from the RAMS simulations were significantly larger than these studies, which typically showed peak latent heating rates of several degrees per hour. However, this discrepancy is in part due to aliasing caused by the inability of observational networks to resolve convective-region processes. A recent study using higher-resolution Doppler-based radar to estimate latent heating, obtained rates of up to 80 K hr^{-1} in intense tropical convective updrafts, which were in keeping with TRMM latent heating estimates for the same system [*Park and Elsberry*, 2013]. Furthermore, other recent 3D modeling studies

of MCSs have also shown convective-region latent heating rates of over 20 K hr^{-1} [*Shige et al.*, 2009; *Adams-Selin and Johnson*, 2013].

2.5.2. Stratiform (STRA) Regions

The STRA regions had net latent cooling from the surface through around the freezing level, with evaporation, melting, and sublimation all playing a significant role, depending on the altitude. The low-level cooling rates in Figure 2.7b,f were similar to observation-based studies of MCSs in the tropics and midlatitudes [*Leary and Houze*, 1979; *Gallus and Johnson*, 1991] and recent detailed modeling studies of stratiform regions [*Grim et al.*, 2009] that all estimated cooling rates of several K hr^{-1}. Given their larger and more uniform sub-cloud areas, stratiform regions are better resolved than convective regions by observational networks.

The vertical profiles in Figure 2.7b,f demonstrate that sublimation had similar cooling rates to evaporation and melting, but was more strongly masked by condensational heating at the same altitude. Furthermore, sublimation contributed ~10-20% of the decrease in latent heating that resulted in the steep latent heating gradient that formed between 4 and 5 km AGL. Some recent observations have suggested the importance of the sublimation of ice particles to latent cooling within MCS stratiform regions, especially for those processes that occur in drier environments [*McFarquhar et al.*, 2007; *Heymsfield et al.*, 2015]. Furthermore, the sublimation cooling peak near the freezing level helps to explain the presence of peak melting ~1 km below the freezing level, as sublimation will continue to cool the hydrometeors and delay the onset of melting. The most intense cooling rates were present near or directly below the freezing level, which was the case in both prior observation-based [*Leary and Houze*, 1979; *Gallus and Johnson*, 1991] and modeling [*Tao et al.*, 1993; *Shige et al.*, 2009; *Grim et al.*, 2009] studies.

Above the freezing level, condensation resulted in net warming from 4 to 6 km AGL, and above 6 km deposition dominated latent heating rates. These processes resulted in a bimodal latent warming signal evident between 4 and 10 km AGL within the STRA regions. Unlike the CONV region, the STRA latent heating rates from riming processes were negligible.

2.5.3. Anvil (ANVL) Regions

In the non-precipitating ANVL region (Fig. 2.7c,g), the mean latent heating rate magnitudes were at least one order of magnitude smaller than in the CONV and STRA regions. The main ANVL latent heating feature was the cooling from sublimation between ~3 and 9 km AGL, which peaked around 6 km. Therefore, there was more dissipation than growth of ice hydrometeors collectively within the ANVL regions.

For completion, mean latent heating profiles for the entire MCS (i.e., a combination of the CONV, STRA, and ANVL regions) are provided in Figure 2.7d,h. The entire MCS profile most closely resembles the CONV profile due to the intensity of the microphysical processes within the CONV region. Comparing the latent heating rates between the CONV, STRA, and ANVL regions, the magnitude of latent heating can vary by over 2 orders of magnitude. Understanding and quantifying such distinctions are useful for parameterizing the effects of MCS latent heating. For example, in order to assess the total MCS impact of warming or moistening in the upper troposphere, total MCS profiles may be more useful (i.e., Fig. 2.7d). However, to assess the interactions of gravity waves with the ambient environment, region-specific profiles (i.e., Fig. 2.7a-c) may be more beneficial since the structure and magnitude of latent heating in convective and stratiform regions can individually influence gravity wave properties [e.g., *Nicholls et al.*, 1991].

2.6 Time Evolution of Latent Heating

To simplify the explanation of the temporal evolution of latent heating, this section will focus on the results from the May 23-24 event, since Figure 2.7 demonstrates the general similarities between the two events. Also, all of the trends for the May 23-24 event discussed below are consistent with the May 20 event simulation, except for trends associated with the decaying stage, since the May 20 MCS was overtaken by a second, developing MCS during its decaying stage (see Section 2.2.1).

For a convenient reference, the 12-hour analysis period for the May 23-24 event was separated into 3 four-hour intervals, which approximately represent the development, mature, and decay stages of the MCS. As discussed in Section 2.2.2, during the development stage (23 May 2100 UTC to 24 May 0100 UTC), individual convective cells initiated and slowly aggregated into a widespread and intermingled region of convective and stratiform precipitation. During the mature stage (24 May 0100 UTC to 0500 UTC), the MCS began to develop a leading convective line and a trailing stratiform region, and the system began to propagate southeastward. The leading convective line also bowed during this time period. In the decay stage (24 May 0500 UTC to 0900 UTC), the convective line began to break apart, and the majority of precipitation became stratiform in nature. Figure 2.8 demonstrates the changes in latent heating within the convective and stratiform regions throughout these three lifecycle stages.

To quantify the results of Figure 2.8, temporally averaged vertical profiles of net latent heating and latent heating from specific microphysical processes were computed for each MCS lifecycle stage from the spatial means within the CONV and STRA regions. From these profiles, the arithmetic mean and maximum latent heating rates over the main regions of net warming and

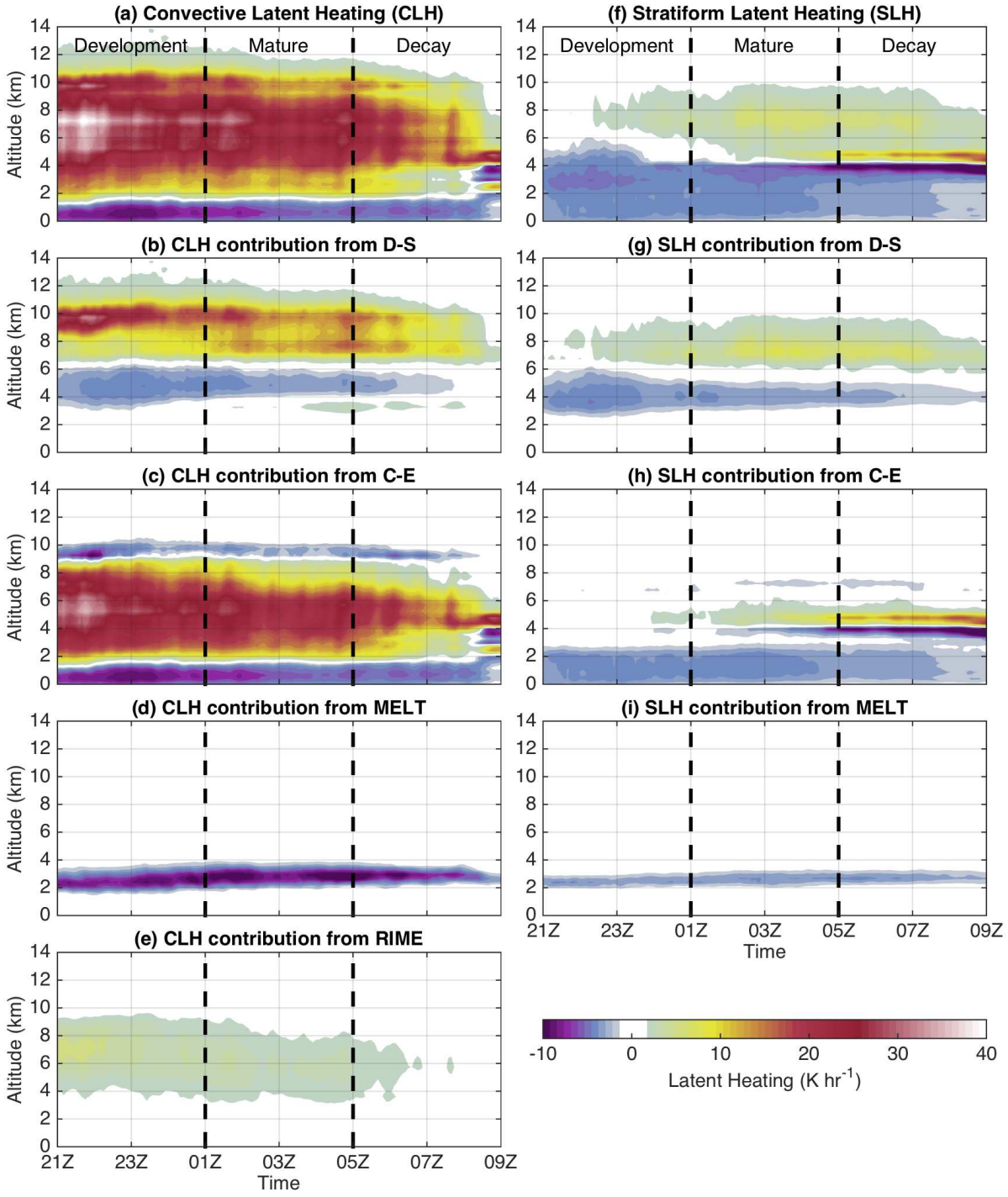

Figure 2.8. The evolution of latent heating rates and contributing microphysical processes throughout the MCS lifecycle stages. CONV latent heating (a) and contributions from key microphysical processes (b-e) are shown throughout the 12-hour analysis period. The evolution of STRA latent heating and contributions from key microphysical processes are shown in (f-i). In STRA regions, RIME processes are negligible and are therefore, not shown.

cooling were then calculated for all levels where latent heating rates were greater than 0.1 K hr^{-1}. Percentage changes in the mean and maximum latent heating rates between lifecycle stages are provided for reference in Tables 2.2 and 2.3.

Table 2.2. Changes in the CONV maximum and mean latent heating rates between MCS lifecycle stages. Latent heating rate vertical profiles are spatially averaged over the CONV region and then temporally averaged over each lifecycle stage. From these profiles, the maximum and mean values are assessed over the main regions of warming and cooling, as seen in Figure 2.8. The two left columns represent maximum and mean latent heating values during the development stage, while the right four columns represent percentage changes in these values to the mature and decay stages.

	Development Stage LH Rate (K hr^{-1})		Mature Stage LH Rate (% Change from Development Stage)		Decay Stage LH Rate (% Change from Development Stage)	
	Maximum	Mean	Maximum	Mean	Maximum	Mean
Latent Warming	34.4	14.1	-21	-13	-45	-45
Latent Cooling	7.8	6.1	-26	-27	-42	-43
Process Level						
D-S Warming	23.8	6.7	-31	6	-57	-33
D-S Cooling	3.4	2.3	-12	-6	-52	-59
C-E Warming	29.6	17.9	-19	-16	-35	-55
C-E Cooling	7.8	6.1	-26	-27	-42	-43
MELT Cooling	8.1	3.1	17	22	-9	-19
RIME Warming	3.0	1.8	-13	-15	-43	-43

Table 2.3. Same as Table 2.2, but for the STRA region.

	Development Stage LH Rate (K hr^{-1})		Mature Stage LH Rate (% Change from Development Stage)		Decay Stage LH Rate (% Change from Development Stage)	
	Maximum	Mean	Maximum	Mean	Maximum	Mean
Latent Warming	2.7	1.3	116	81	421	168
Latent Cooling	4.2	3.0	35	4	201	-8
Process Level						
D-S Warming	3.1	1.4	121	55	93	64
D-S Cooling	3.3	2.1	-15	-24	-38	-39
C-E Warming	1.1	0.8	373	282	1206	644
C-E Cooling	3.2	2.3	5	2	233	-3
MELT Cooling	2.8	1.2	5	4	0	0

2.6.1. Convective (CONV) Regions

The latent heating and cooling rates in the CONV region generally decreased in magnitude throughout the MCS lifecycle (Fig. 2.8a, Table 2.2). Maximum latent cooling rates below the cloud base decreased by ~20% in each progressive stage (see Table 2.2). This reduction in evaporative cooling (Fig. 2.8c) was due to increases in the low-level relative humidity, which were driven by increased water vapor concentrations and decreased temperatures. *Schlemmer and Hohenegger* [2015] recently demonstrated using a CRM simulation that water vapor advection is the dominant contributor to moistening cold pool edges (i.e., the convective region of MCS cold pools) within convective systems over land. This moisture advection into the CONV region, along with continued, though weakening, rates of precipitation evaporation and surface latent heat flux all contribute to CONV sub-cloud moistening. Decreased temperatures below the cloud base were in part a result of evaporation, the advection of cooler air, and diurnal-based cooling.

CONV latent warming from deposition, condensation, and riming all decreased throughout the MCS lifetime (Fig. 2.8b,c,e, respectively) with relatively similar rates of ~15-30% per stage (see Table 2.2), suggesting that these heating rates are tied to a similar forcing. To a first order, vertical velocity dictated these changes in latent warming, since stronger and more frequent updrafts are associated with increased supersaturation, enhanced hydrometeor collision efficiencies, and greater vertical flux of water within the cloud. Throughout the MCS lifetime, the frequency of the strongest CONV vertical motions decreased (Fig. 2.9a-c). While the mature stage had more frequent moderate updrafts (~1-8 m s^{-1}) between ~3 and 10 km AGL (Fig. 2.9b), the MCS had an increased propagation speed during the mature phase, which led to a larger, storm-relative horizontal component to the CONV updrafts (i.e., ascending, front-to-rear flow),

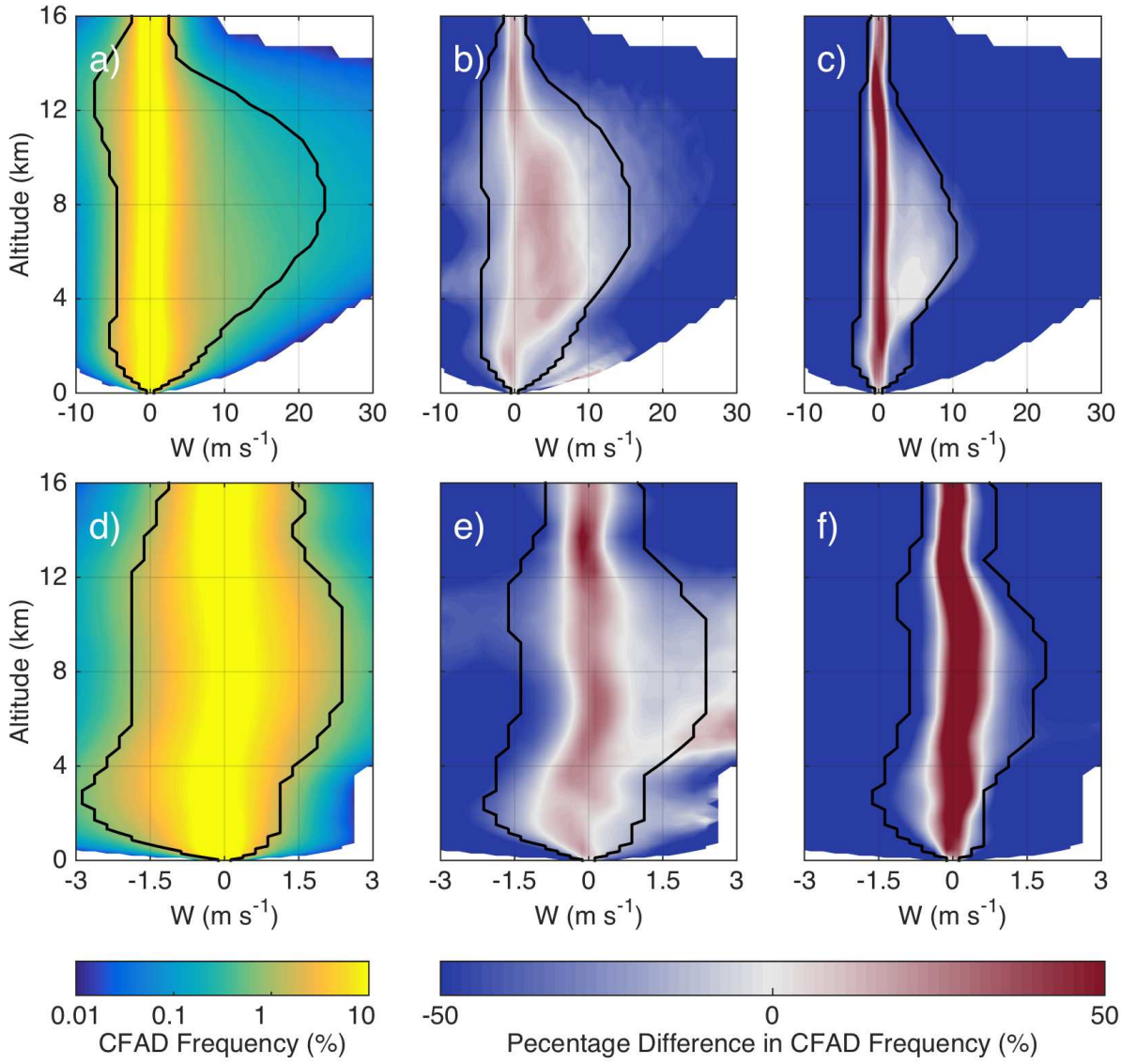

Figure 2.9. Vertical velocities within CONV and STRA regions for the MCS lifecycle stages. Contour frequency by altitude diagrams [*Yuter and Houze*, 1995; CFADs] of vertical velocity are shown for the CONV region (a-c) and the STRA region (d-f). The left panels represent data during the development stage, while the center and right panels represent percentage differences in CFAD frequency from the development stage to the mature and decay stages, respectively. CONV region bin spacing is 1 m s^{-1}, and stratiform bin spacing is 0.25 m s^{-1}. At each vertical level, 95% of the data fall within the black contours.

which can be seen in the cross sections shown in Figure 2.10. In the development stage cross section (Fig. 2.10a,d), the MCS convective updrafts were more upright with a large, forward component to the motion in the southeast part of the MCS cross section, forming a more

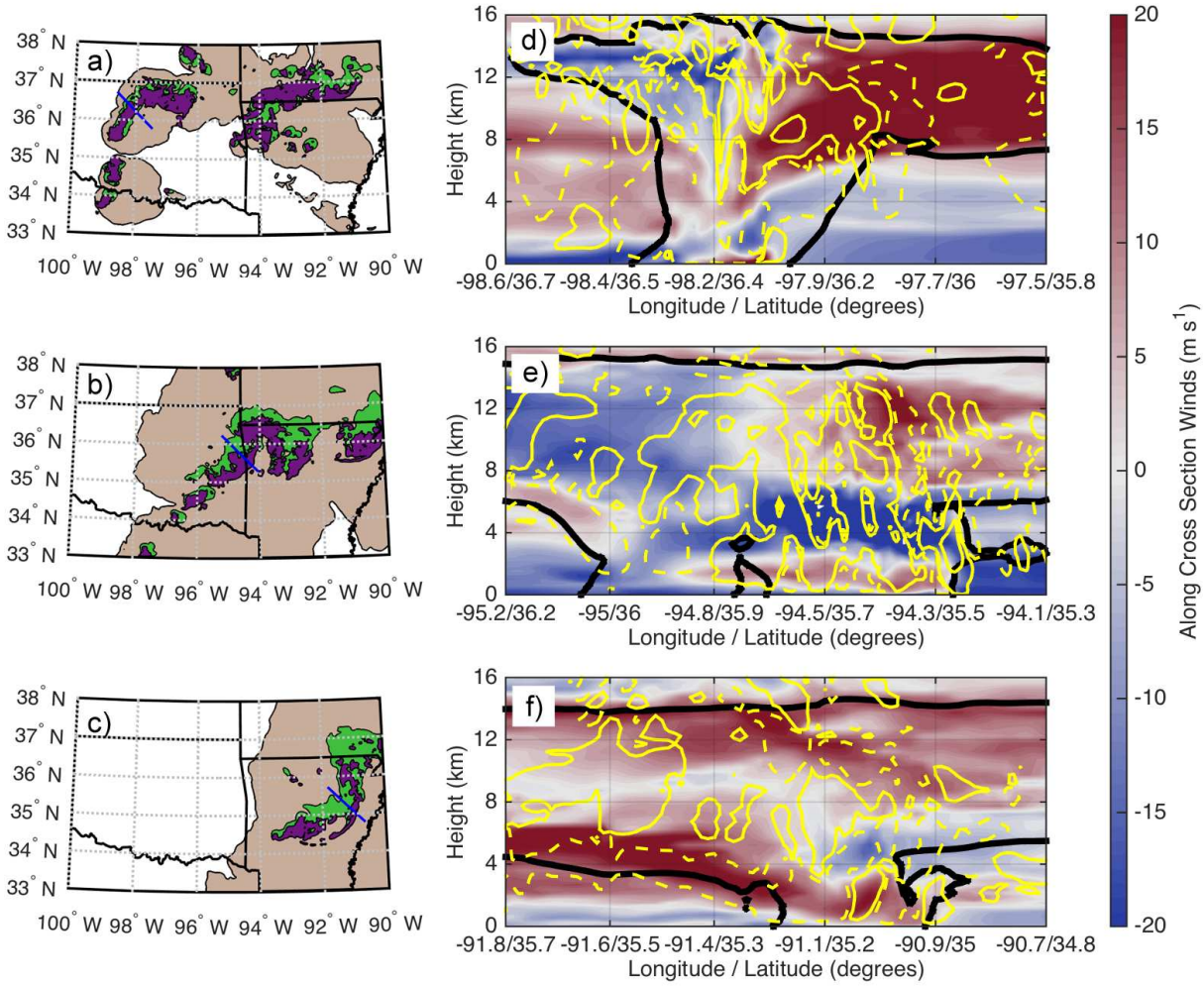

Figure 2.10. MCS flow patterns shown in a 100 km cross section through the MCS during the different lifecycle stages. The locations of cross sections are shown by a blue, solid line in (a-c) and occur at 2300 UTC May 23, 0300 UTC May 24, and 0700 UTC May 24, respectively. Shading in (a-c) represents convective, stratiform, and anvil regions as shown in Figure 2.6. Cross sections of vertical winds and horizontal winds in the direction along the cross section are shown in (d-f) for the development, mature, and decay stages, respectively. The black, solid contour represents 0.1 g kg^{-1} total condensate mixing ratio. The yellow, dashed contours represent -0.5 and -5.0 m s^{-1} vertical motions, while the yellow, solid contours represent +0.5 and +5.0 m s^{-1} vertical motions. The shaded areas represent storm-relative winds that are parallel to the cross sections. Storm motion was 7.4 m s^{-1}, 16.6 m s^{-1}, and 5.6 m s^{-1} for the development, mature, and decay stage cross sections, respectively.

extensive forward anvil, as compared to the rearward anvil. In the mature stage cross section (Fig. 2.10b,e), the MCS propagation speed increased from the development stage cross section (~7 m s^{-1}) to ~17 m s^{-1}, assisting the development of a continuous front-to-rear, ascending flow.

In the decay stage (Fig. 2.10c,f), the MCS also demonstrated a front-to-rear, ascending flow that was similar to the mature stage, although significantly weaker, in part due to a weaker MCS propagation speed of 5.6 m s^{-1}. Propagation speeds were estimated during each cross section based on the locations of the maximum surface precipitation gradient (i.e., leading edge of the intense MCS precipitation) at the model output time before and after the cross sections.

The combination of less frequent intense vertical motions and increased front-to-rear flow out of the CONV region lowered the amount of water mass reaching the upper levels of the CONV region throughout the analysis period (Fig. 2.11), which both weakened the magnitude of latent warming (Table 2.2) and assisted in the decrease in altitude of the most intense deposition, condensation, and riming rates by 1-2 km with time (Fig. 2.8b,c,e). While peak warming processes lowered in altitude, the altitude where peak melting occurred increased in altitude by ~1 km. This was due to a decrease in the magnitude of sublimational cooling rates.

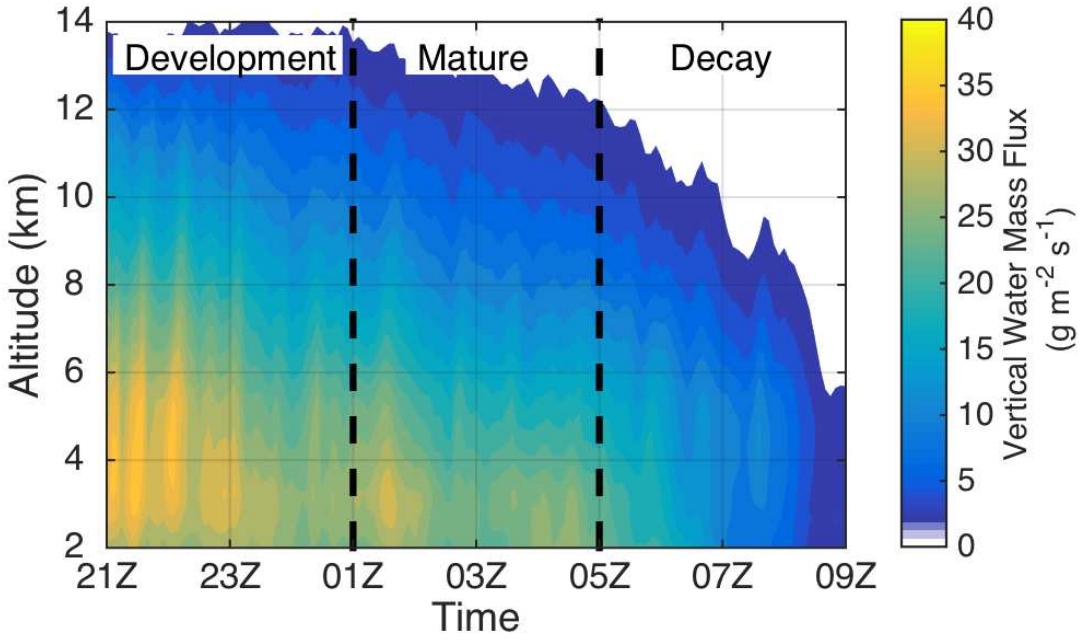

Figure 2.11. CONV vertical water mass flux throughout the MCS lifecycle stages. Vertical water mass flux is calculated by multiplying vertical velocity, air density, and total water mixing ratio at all locations where w is positive, and spatially averaging these values over classified CONV regions.

2.6.2. Stratiform (STRA) Regions

The temporal evolution of the STRA latent heating profile includes a distinct transitional period between 24 May 0000 UTC and 0200 UTC (Fig. 2.8f-h). In the development stage, latent cooling was present below 6 km AGL, and latent warming above this level, with peak warming of 2.7 K hr^{-1} and peak cooling of 4.2 K hr^{-1} occurring at ~7 km and ~3 km AGL, respectively (Fig. 2.8f, Table 2.3). However, as the MCS entered the mature phase, a prevailing storm-relative, front-to-rear flow and a descending rear-inflow jet above and below 4 km AGL, respectively, developed. The differences in the storm structure and flow pattern between the development and mature stages of the MCS can be seen in the cross section of Figure 2.10. This changing flow pattern was not limited to this cross section, as indicated by the increase in the frequency of positive vertical motions between 4 and 8 km AGL and negative vertical motions below 4 km AGL in Figure 2.9e. These processes shifted the altitude of the transition between net latent warming and cooling to near 4 km AGL (Fig. 2.8f).

The shift in transition altitude was also associated with increases in STRA precipitation processes, which acted to moisten the mid-levels (~3-6 km AGL) and resulted in decreasing mean sublimation-based latent cooling throughout the MCS lifecycle (Fig. 2.8g, Table 2.3). During the mature stage, this mid-level moistening allowed for more precipitation to reach the low-levels (~0-3 km AGL). Following the enhanced mature-stage precipitation, low-level moistening and the eventual weakening of stratiform precipitation rates quickly reduced evaporation-based latent cooling in the decay stage (Fig. 2.8h). Similar to the CONV region, decreases in the magnitudes of sublimation-based cooling allowed peak melting rates to increase in altitude by ~1 km throughout the analysis period (Fig. 2.8g,i).

In-cloud, STRA latent warming, which was most frequently caused by deposition throughout the majority of the MCS lifecycle (recall Fig. 2.7b,f), approximately doubled between the development and mature stages (Fig. 2.8g, Table 2.3), assisted by enhanced water flux from the CONV region, as well as the generation of supersaturation from the ascending, front-to-rear flow that developed (Fig. 2.10e). During the decay stage, stratiform vertical motions weakened (Fig. 2.9f and Fig. 2.10f), which led to decreased depositional heating rates. However, a spike in condensation and evaporation rates occurred in the decay stage near 4 km AGL, which led to increases in maximum latent heating and cooling of several hundred percent from the development stage (see Table 2.3). This spike in latent heating was focused in the large stratiform area in the northern region of the MCS (Fig. 2.12a). A descending rear-inflow jet toward the northern edge of the STRA region converged with southerly flow in the lower levels (Fig. 2.12b). This convergence (Fig. 2.12c) was associated with weak upward motions and an expansive region of cloud development. This spike in both condensation and evaporation, and the resulting gradient in diabatic heating, can assist in the development of MCVs in the late stages of an MCS's lifetime [e.g., *Fritsch et al.*, 1994]. For the May 23-24 event, this process may have contributed to an observed vorticity maximum (and a potential MCV) that travelled eastward after the MCS decayed and assisted in the initiation of new convection in Tennessee and Kentucky between 1400 UTC and 1800 UTC on 24 May 2011.

2.6.3. Anvil (ANVL) Regions

ANVL latent heating had minimal changes throughout the MCS lifetime (not shown), as compared to the STRA and CONV regions. While peak cooling from sublimation occurred at the same altitude (~6 km AGL) with the same magnitude (~0.5 K hr^{-1}) throughout the analysis

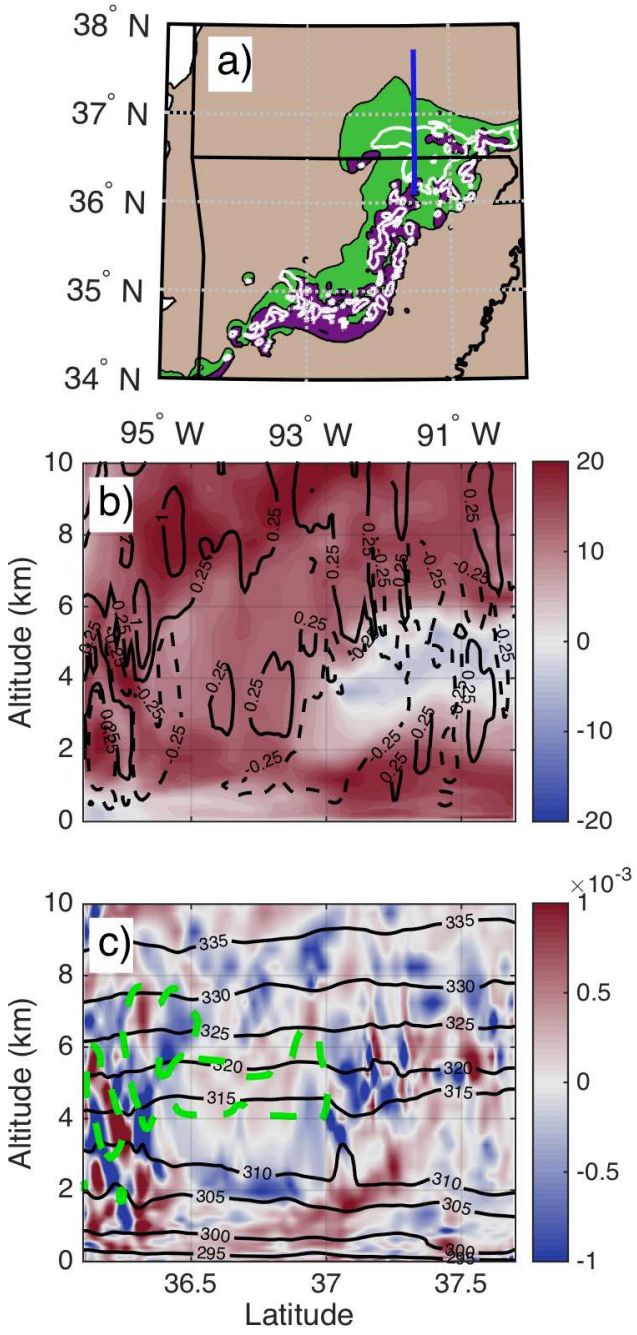

Figure 2.12. Cross section through simulated May 23-24 MCS at 24 May 2011 0600 UTC. In (a), purple, green, and brown regions represent CONV, STRA, and ANVL regions of the MCS, respectively. White contours represent condensation rates of 1 g kg^{-1} 5-min^{-1} at ~4 km AGL. (b) and (c) represent cross sections through the blue line shown in (a). In (b), meridional winds (m s^{-1}) are shaded, positive vertical winds (m s^{-1}) are contoured with solid, black lines, and negative vertical winds (m s^{-1}) are contoured with dashed, black lines. In (c), horizontal divergence is shaded (s^{-1}), potential temperature (K) is contoured with solid, black lines, and cloud mixing ratio of 0.1 g kg^{-1} is contoured with dashed, green lines.

period, the amount of latent cooling above this peak level decreased most significantly from the mature stage to the decay stage, which was associated with the weakening vertical motions and water mass flux in the decay stage, as shown in Figures 2.9, 2.10, and 2.11.

2.7 Conclusions and Implications

In this study, the vertical structure and evolution of MCS latent heating rates and the contributing microphysical processes within CONV, STRA, and ANVL regions are assessed using CRM simulations. Such simulations prove useful in this regard since observation-based methods of estimating latent heating rates have not been able to resolve such details. This study focuses on two LLTS, midlatitude, continental MCS events (20 May 2011 and 23-24 May 2011) that occurred during MC3E. Using the cloud-resolving RAMS, 3D simulations of these two events were conducted and compared to a suite of observations. The simulated accumulated precipitation totals for both events are within ~10% of the observations. Weak to moderate convective updraft strengths were well represented, however, the strongest updrafts (95^{th} percentile) were overpredicted, particularly in the May 23-24 event simulation. Overestimation of MCS updrafts by CRMs has also recently been observed for both tropical and midlatitude MCSs [*Varble et al.*, 2014; *Fan et al.*, 2015]. In spite of the shortfalls in simulating the strongest updrafts, the RAMS model was able to reproduce many of the key features of these two observed MCS events, including the storm development and propagation. Therefore, these simulations were used to assess the key microphysical processes that contributed to latent heating and the evolution of these processes.

Temporally averaged latent heating rates over a 12-hour period beginning with the initial convection associated with the MCSs were used to assess the latent heating rates due to various

microphysical processes. CONV regions had peak evaporation-based latent cooling rates below cloud base of comparable magnitude to stratiform regions (3-4 K hr^{-1}). CONV regions also had peak condensation-driven latent warming rates of 15-30 K hr^{-1} between 4 and 8 km AGL. However, this latent warming from condensation between 2 and 5 km can be offset significantly by in-cloud melting and sublimation. While CONV latent heating was dominated by condensational growth in the mid-levels, vapor deposition produced comparable latent heating rates in the upper levels of deep convection (10-20 K hr^{-1}).

In STRA regions, a bimodal latent warming structure with peak latent warming of ~5-8 K hr^{-1} (temporally averaged) near 5 and 7 km AGL was present. Peak sublimation, melting, and evaporation rates were ~2-3 K hr^{-1}, with the dominant process depending on the altitude. In both CONV and STRA regions, peak melting rates occurred ~1 km below the freezing level due to sublimation. Riming and nucleation processes had a limited impact on latent heating, regardless of the MCS region. The key process driving latent cooling in the non-precipitating anvil region was net sublimation, and these cooling rates were at least one order of magnitude smaller than STRA and CONV processes.

The shapes of the vertical profiles and the magnitude of net latent heating rates were very similar between the two simulated events and were generally in keeping with prior observation-based studies of midlatitude, continental MCSs [*Gallus and Johnson*, 1991; *Braun and Houze*, 1996], except for the convective regions where observations can be impaired by aliasing biases. This suggests that information from these simulations may be applicable to similarly structured MCSs in comparable environments.

This research has also demonstrated that the typical latent heating magnitudes and profile shapes within MCS regions can change substantially over the MCS lifetime (Fig. 2.13).

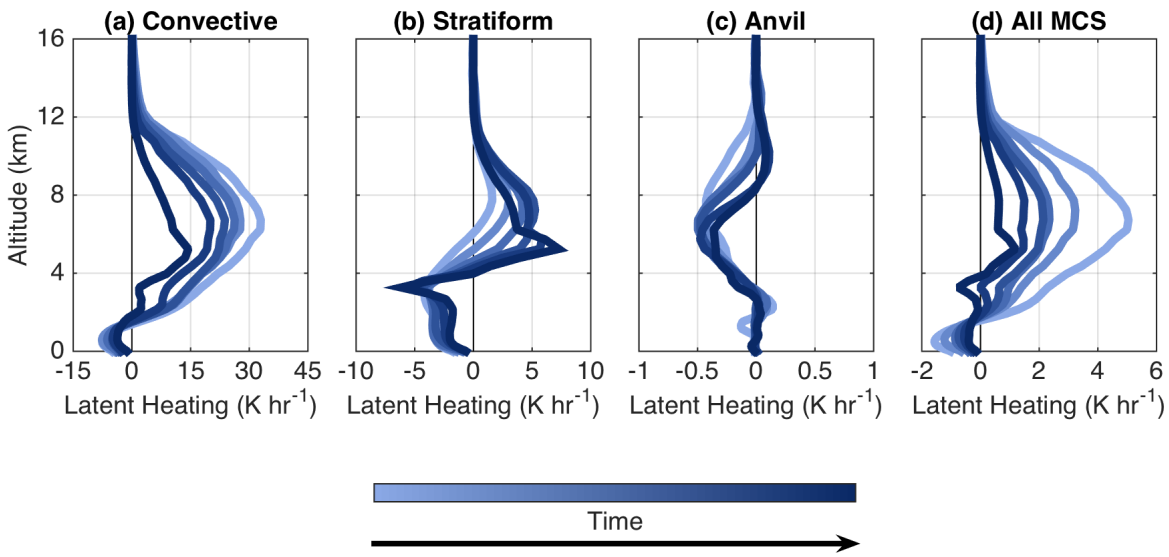

Figure 2.13. Schematic of the latent heating profile changes with MCS evolution. Profiles are shown for CONV (a), STRA (b), and ANVL (c) regions, as well as the entire MCS (d). Profiles are calculated from the 23-24 May 2011 simulation data and is smoothed using a 5-point moving average.

Throughout the simulations of both MCS events, CONV latent warming and cooling magnitudes changed in an approximately linear manner, decreasing by over 40% from the development stage to the decay stage. In the STRA region, deviations in both the latent heating magnitudes and profile shapes occurred. As the MCS transitioned from the development stage to the mature stage, increased storm propagation speeds resulted in more intense ascending, front-to-rear flow within the MCS, which more than doubled deposition and condensation rates in the STRA region, yet weakened the latent heating from these processes in the CONV region. In the decay stage, weaker updrafts reduced both the magnitude and altitude of peak latent warming in CONV regions. In the STRA region, deposition-based latent heating also weakened during the decay stage, but condensation and evaporation rates spiked near 4 km AGL, where widespread cloud formation was forced from the convergence of the descending rear inflow jet and front-to-rear flow. In both CONV and STRA regions, sublimation- and evaporation-based latent cooling from

precipitating hydrometeors generally decreased with time due to atmospheric moistening and cooling from a variety of processes. ANVL regions were subject to minimal changes in latent heating throughout the simulation, as compared to CONV and STRA regions.

As latent heating evolves throughout the lifetime of the MCS, the forcing that MCS latent heating imposes on the storm system itself and its ambient environment will also vary. The changing latent heating magnitudes and profile shapes in both CONV and STRA regions will alter the structure of the gravity waves that form, and how they couple with each other and the environment. Weakening rates of latent cooling in both sub-cloud CONV and STRA regions will also impact how the MCS cold pool develops, and subsequently, how the MCS will propagate and force new convection. The couplet of intense condensation and evaporation that intensifies the latent heating vertical gradient in the STRA region during the decay stage can create more favorable conditions for MCV development. Large-scale models that have not been designed to reproduce the complex structure of latent heating profiles within MCSs and its temporal variability will be unable to properly reproduce these and other downstream effects of MCS latent heating. *Del Genio et al.* [2012] argued that given the organized nature of MCSs, GCM parameterizations require a "mesoscale memory" to properly represent the evolution of these systems. The results provided in this study support that argument and demonstrate the dynamic yet regulated nature of MCS latent heating throughout the MCS lifecycle.

CRMs continue to be one of the best tools to assess this temporal evolution of latent heating and microphysical process rates. For this reason, latent heating algorithms for TRMM [e.g., *Tao et al.*, 2006; *Shige et al.*, 2009] have all been based, to some degree, on CRM simulations. CRM simulations continue to improve with more sophisticated parameterizations and enhanced grid resolutions, thus offering more confident guidance to the development of

improved convective parameterizations and satellite algorithms that require cloud-scale information, such as latent heating rates. However, further observations are needed to assist in the validation of CRM microphysical processes and the dynamic motions driving them.

CHAPTER 3: THE RELATIVE ROLES OF MIDDLE- AND LOWER-TROPOSPHERIC AEROSOL ON MATURE MCS PRECIPITATION RATES

3.1 Introduction

During the warm season in the central United States, mesoscale convective systems (MCSs) are the highest contributors to surface accumulated precipitation [*Fritsch et al.*, 1986]. Also, under certain atmospheric conditions, individual MCS events can also produce high amounts of precipitation that lead to flooding [e.g., *Doswell et al.*, 1996; *Schumacher and Johnson*, 2005; *Stevenson and Schumacher*, 2014], such as the extreme 1993 Floods in the Mississippi Valley [*Kunkel et al.,* 1994]. As such, understanding changes to MCS precipitation due to perturbations in the environment is important.

Each year, expansive biomass burning events occur in Mexico and Central America (Fig. 3.1). The wind patterns that are responsible for providing favorable MCS conditions in the central United States during the spring and summer months (i.e., warm and moist air, wind shear) are also frequently responsible for transporting high aerosol particle concentrations from these large biomass burning events in Central America and Mexico into the central United States [*Rogers and Bowman*, 2001; *Gebhart et al.*, 2001; *Duncan et al.*, 2003; *Wang et al.*, 2006]. Observations from the Department of Energy's Atmospheric Radiation Measurement Program's Southern Great Plains site (ARM-SGP; 36.6^{o}N, 97.5^{o}W) have shown that biomass burning aerosol particles are frequent in the spring and summer months [*Peppler et al.*, 2000; *Sheridan et al.*, 2001; *Andrews et al.*, 2004]. *Peppler et al.* [2000] further reported that while biomass burning aerosol particles were confined to the boundary layer in the first few weeks of May 1998, that later in the month the biomass burning particles were observed in a layer between 3

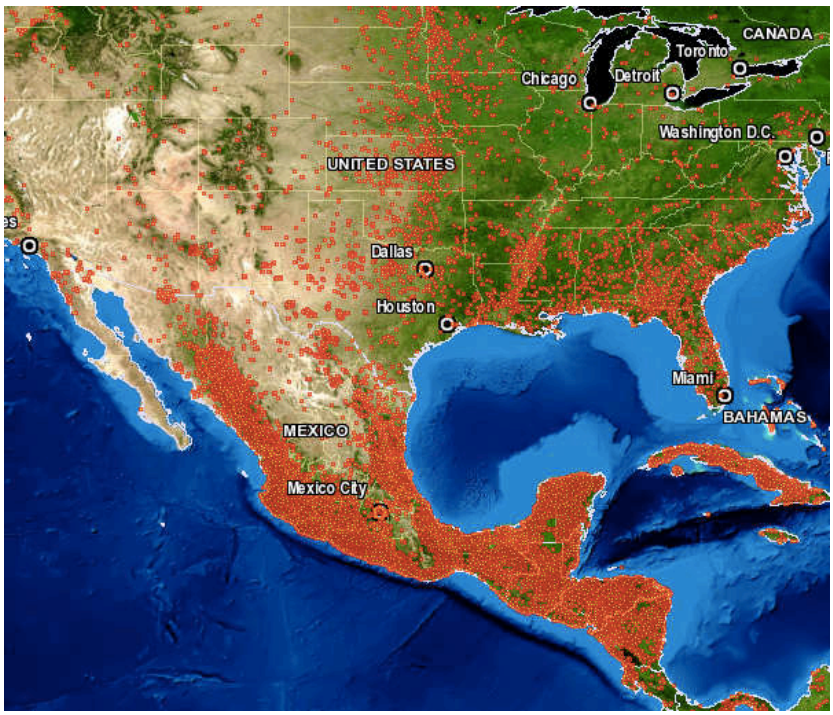

Figure 3.1. Active fires during MC3E (22 April through 6 June 2011) retrieved from the MODIS sensor. The data were from the MOD14/MYD14 Fire and Thermal Anomalies product, and the image was generated from firms.modaps.eosdis.nasa.gov/firemap/.

and 6 km, thus demonstrating the variability in the altitude of primary transport pathways. Smoke aerosol particle mass concentrations predicted from the Navy Aerosol Analysis and Prediction System (NAAPS, Fig. 3.2) further demonstrate that biomass burning aerosol particles can be transported into the southern United States both within the lower troposphere and the middle troposphere, and that there can be regions with higher concentrations of transported aerosol particles in the middle troposphere as compared to the lower troposphere (i.e., Great Lakes Region in Fig. 3.2). This influx of biomass burning aerosol particles into the central United States has also been suggested by numerous studies to be linked to an increased frequency and intensity of severe weather in the region, although these studies have focused more on lightning, hail, and tornadoes and less on the impacts of aerosol particles on MCS precipitation [*Lyons et al.*, 1998; *Murray et al.*, 2000; *Wang et al.*, 2009; *Saide et al.*, 2015].

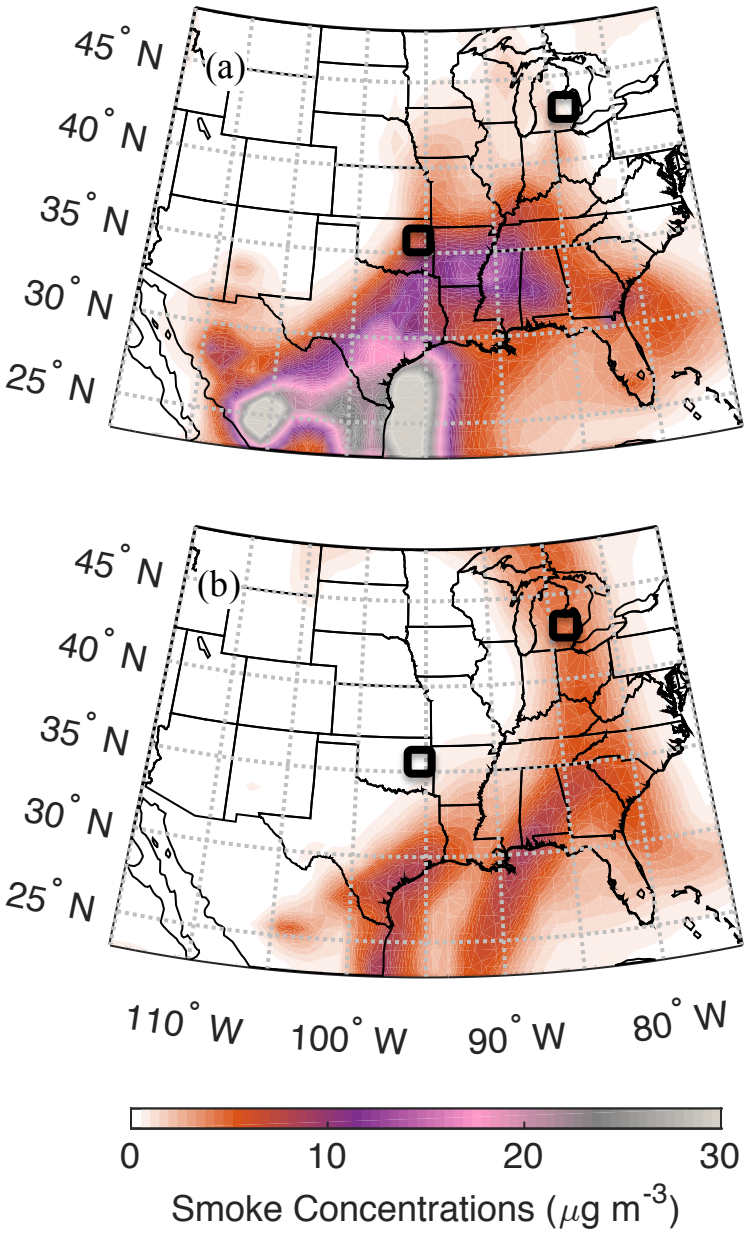

Figure 3.2. NAAPS model smoke mass concentrations from 20 May 2011 0000 UTC at (a) ~1 km AGL and (b) ~5 km AGL. The black boxes represent the areas used to create sensitivity aerosol profiles for the model initialization, as described in Section 2.2. The data was retrieved from www.datafed.net.

Most modeling studies that have focused on the impact of aerosol particle concentration perturbations on MCS precipitation have been conducted by running a suite of simulations, whereby the number concentrations of aerosol particles near the surface or throughout the total

atmospheric column were altered by some factor [*Khain et al.*, 2005; Wang, 2005; *Tao et al.*, 2007; *Lee et al.*, 2008; *Li et al.*, 2009; *Lebo and Morrison*, 2014]. These studies have shown that under increased aerosol concentrations, MCS total surface accumulated precipitation can increase, decrease, or remain relatively unchanged [*Tao et al.*, 2012]. The differences between these studies may be due to many factors, including differences in the model configurations used in the respective studies (e.g., grid spacing, physical parameterizations) and differences in the environmental factors of the MCS events simulated [e.g., *Tao et al.*, 2007; *Khain et al.*, 2008; *Fan et al.*, 2009].

On the other hand, only a couple of studies [*Fridlind et al.*, 2004, herein F04; *Lebo*, 2014, herein L14] have assessed how the vertical variation of aerosol particle number concentrations impacts deep convection, which is especially relevant for regions where aerosol particles can be transported from distant sources (e.g., biomass burning aerosol transport into the central United States). F04 demonstrated using both simulations and measurements from the Cirrus Regional Study of Tropical Anvils and Cirrus Layers–Florida Area Cirrus Experiment (CRYSTAL-FACE) that middle-tropospheric aerosol particles can become entrained into strong, convective updrafts and impact the cloud droplet spectrum and anvil properties in tropical convection. L14 used idealized numerical simulations of a squall line to assess the impact of the vertical location of aerosol particles on many aspects of a squall line, including precipitation. L14 presented that the simulation initialized with high concentrations of aerosol particles in the middle-to-upper-troposphere was most similar to the simulation with high aerosol particle concentrations throughout the entire atmospheric column in terms of precipitation and overall MCS structure (e.g., convective updraft mass flux, hydrometeor amounts), suggesting that perturbations to the middle-tropospheric aerosol concentrations may have a more significant impact on MCS

intensity than perturbations to the lower-tropospheric aerosol concentrations. However, one limitation of L14 is that the vertically integrated aerosol mass between the sensitivity aerosol profiles was not constant, such that the initial aerosol profile with greater particle concentrations in the middle-to-upper troposphere had ~1.8 times more vertically integrated aerosol mass (based on a standard atmosphere density profile) than the profile with peak aerosol concentrations in the lower troposphere. As such, the differences between the L14 simulations could be attributed to the differences in aerosol mass and number present rather than to the location of the aerosol. Another limitation of the L14 study is that only one idealized MCS was simulated, and therefore, that study was unable to provide guidance as to whether the results were applicable to MCSs occurring across a range of environments.

In this study, we compared the results of several simulations that only varied in the aerosol profile used to initialize the simulation, in order to assess the relative roles of middle-tropospheric and lower-tropospheric cloud-activating aerosol particles on MCS precipitation during the mature stage. However, in this study, the vertically integrated aerosol total mass and number remained constant among the sensitivity aerosol profiles. Therefore, differences between the simulations were directly attributable to the changes in the vertical locations of the peak aerosol concentrations rather than to the differences in the total environmental aerosol concentrations. Furthermore, simulations conducted in this study represent specific MCS events that took place during the Midlatitude Continental Convective Clouds Experiment (MC3E), which occurred concurrently with expansive biomass burning in Mexico and Central America (Fig. 3.1). Therefore, both the simulations and sensitivity aerosol profiles used in this study were constrained by observations, as described in Sections 3.2.1 and 3.2.2. The focus of this study is on the mature stages of two MCS events that occurred on 20 May 2011 and 23-24 May 2011.

The mature stage was chosen since the majority of MCS precipitation falls during this stage with significant contributions from both the convective and stratiform regions [e.g., *Houze,* 1977; *Watson et al.*, 1988]. These May 20 and May 23-24 MC3E events were summarized in Chapter 2. We discuss results from the May 20 event simulations in Section 3.3, with Section 3.4 providing a comparison between the two MCS events. The study is summarized in Section 3.5.

3.2 Experimental Design

3.2.1. Model Description

Simulations of the two MCS events were conducted with the Regional Atmospheric Modeling System (RAMS). RAMS is a 3D, non-hydrostatic cloud-resolving model that utilizes a two-moment, bin-emulating bulk microphysics that prognoses eight hydrometeor species [*Meyers et al.*, 1997; *Cotton et al.*, 2003; *Saleeby and Cotton*, 2004; *Saleeby and van den Heever*, 2013]. This bin-emulating scheme utilizes lookup tables to calculate more accurate cloud droplet nucleation, hydrometeor collection efficiencies, and hydrometeor fall speeds than other bulk microphysics parameterizations. RAMS can therefore be used to study MCS precipitation with a more reasonable computational expense, as compared to simulations with traditional bin schemes. This simulation time reduction is especially useful when running a suite of simulations or when simulating atmospheric features with long lifetimes. The model is initialized with aerosol number concentrations at each model grid point, with the same underlying size distribution throughout the domain. All aerosol particles are available to act as cloud condensation nuclei (CCN), which can be activated to form cloud droplets based on the specified particle sizes, specified particle hygroscopicity, and model-predicted environmental conditions, including vertical velocity, temperature, and aerosol particle number concentrations.

Therefore, the terms aerosol particles and CCN will be used interchangeably in this manuscript. RAMS also computes aerosol particle advection and tracking. Aerosol particles can be removed via cloud droplet nucleation, wet scavenging, and dry deposition, and can be returned to the atmosphere via the evaporation and sublimation of hydrometeors. RAMS also computes ice nucleation from separate, specified profiles of potential ice nuclei (IN) [*Saleeby and van den Heever*, 2013].

In these experiments, vertical profiles of aerosol concentrations were initialized as horizontally homogenous across the model domain. No sources of aerosol were introduced throughout the simulation time period, although aerosol were able to be advected between grids. The aerosol particles used in all of the simulations were specified to have a soluble mass fraction of 0.2 (corresponding to a hygroscopicity parameter, κ, of 0.15) and to follow a lognormal distribution for number concentrations with a geometric mean diameter of 120 nm and a standard deviation (σ_g) of 1.8. These values were determined in a manner such that the integrated lognormal aerosol distribution matched both CCN number concentration measurements and chemical speciation measurements at ARM-SGP during MC3E polluted periods. IN concentrations were kept fixed between the simulations and were based on vertical profiles of aerosol particle concentrations with diameters larger than 500 nm from airborne observations during MC3E, as well as surface concentrations of aerosol particles with diameters larger than 500 nm at ARM-SGP [*Saleeby et al.*, 2016]. These IN were activated in the model simulations based on the ice nucleation scheme developed in *DeMott et al.* [2010]. Aerosol particles were not allowed to be radiatively active, in order to isolate the microphysical impacts of aerosol particles on MCS precipitation.

Simulations were conducted with three nested grids, with the innermost grid spanning from approximately 33°N to 38°N and -102°W to -90°W with 1.2 km horizontal grid spacing. The Global Data Assimilation System (GDAS-FNL) re-analysis data from 20 May 2011 were used to initialize and provide lateral boundary conditions for the May 20 event, while the Rapid Update Cycle (RUC) analysis data was used for the May 23-24 event. The simulations were initialized at 0000 UTC and 1600 UTC, respectively. Additional details about the simulation dimensions, initialization datasets, and model parameterizations follow Chapter 2 and can be found in Table 2.1.

3.2.2. Aerosol Sensitivity Profiles

For each MCS event four simulations were conducted that varied the initial horizontally homogenous aerosol concentration profile in order to assess the impacts of the vertical distribution of aerosol on MCS precipitation. These four profiles are displayed in Figure 3.3. The

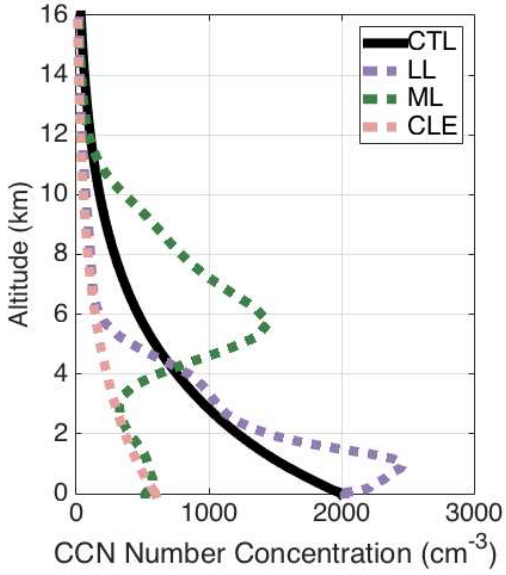

Figure 3.3. Cloud condensation nuclei (CCN) vertical profiles used at model initialization for the sensitivity simulations.

control case (CTL, black line) utilized a profile that had surface aerosol number concentrations of 2000 cm^{-3} and that decreased the aerosol number concentration exponentially with a scale height of 7 km. The surface concentrations used for the CTL simulations were based on CCN concentrations measured at 1% supersaturation from ARM-SGP at the onset of both events (Fig. 3.4). In the hours leading up to both MCS events the CCN concentrations measured at ARM-SGP were relatively constant. They subsequently decreased sharply as precipitation associated with the MCSs began to affect the area. To keep the CCN initializations consistent between the different event simulations, 2000 cm^{-3} was used as a representative, surface CCN concentration.

Profiles in which the aerosol concentrations in the lower-tropospheric levels and middle-tropospheric levels were enhanced (Fig. 3.3, LL and ML, respectively) were used to test the

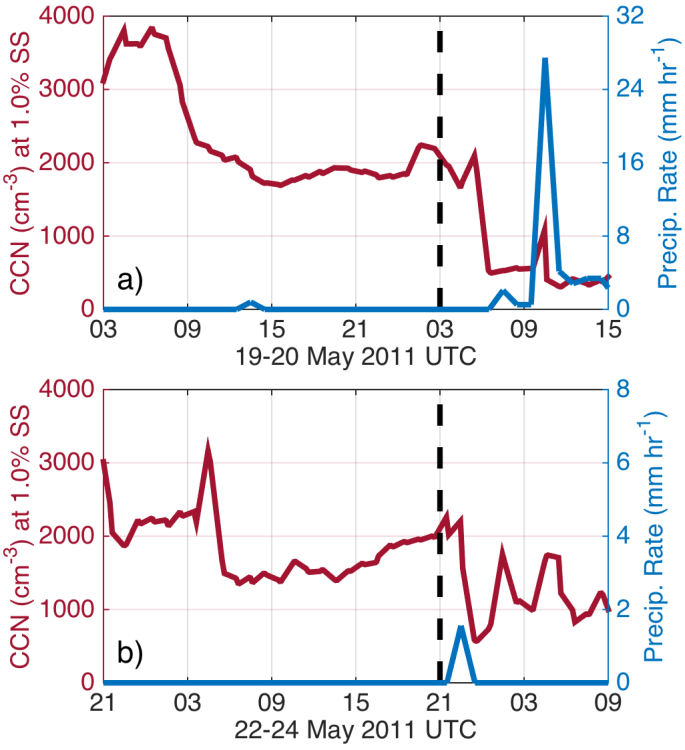

Figure 3.4. Time series of CCN number concentrations measured at approximately 1.0% supersaturation and precipitation rate at ARM-SGP for (a) the May 20 event and (b) the May 23-24 event. The dashed, black line represents the approximate time when the initial storms from both MCS events began to form in the region.

impacts of increased aerosol in the lower troposphere (~0-3 km AGL) and the middle troposphere (~4-9 km AGL). The LL and ML profiles have the same vertically integrated aerosol mass as the CTL profile, and therefore, changes between the simulations can be directly attributed to changes in the vertical location of aerosol concentrations as opposed to the changes in the total amount of aerosol mass (or number). Simulated aerosol fields during MC3E from NAAPS were used to develop the LL and ML profiles. NAAPS is a global model that predicts the mass concentrations for several different aerosol types, including smoke/soot and sulfate. A detailed description of the NAAPS model is provided in *Witek et al.* [2007]. On 22 May 2011 0000 UTC, NAAPS predicted a smoke plume entering the central United States from Central America and Mexico. Average vertical profiles of smoke/soot and sulfate mass concentrations were calculated over a 2^{o} x 2^{o} area from the NAAPS output. These average profiles were calculated in two different regions of the central United States in order to better represent the range of the aerosol profiles that an MCS may encounter (see Fig. 3.2). The average profiles were divided by the total vertically integrated aerosol mass within the profile to create fractions at each level, and these fractions were then applied to the total integrated aerosol mass from the CTL profile in order to ensure that the total integrated aerosol mass (and number) were constant between the three sensitivity aerosol profiles (CTL, LL, and ML) at initialization.

A fourth profile was used that had relatively clean, background aerosol concentrations throughout the vertical profile (CLE, pink line). Since this CLE profile had very similar aerosol concentrations to the ML profile from the surface to ~3 km AGL, features that occur in the ML simulations that are significantly different from the CLE simulations can be used to infer the relative impact of middle-tropospheric aerosol on the MCS.

3.2.3. Cross Section Analysis

The air flows and structure of mature leading line, trailing stratiform (LLTS) MCSs can often be approximated as two-dimensional [e.g., *Rutledge and Houze*, 1987; *Fovell and Ogura*, 1988]. Therefore, cross sections through MCSs are frequently used to create a simplified understanding of the kinematic and microphysical processes within the different regions of these systems. In this study, composite cross sections during the mature stage of the simulated MCSs were created relative to the propagating cold pool boundary. The cold pool boundary was defined in the model based on wind shifts and gradients in density potential temperature (θ_ρ). Density potential temperature was defined as

$$\theta_\rho = \theta * \frac{1 + \frac{r_v}{\varepsilon}}{1 + r_T}$$

where θ is the potential temperature (K), r_v is the water vapor mixing ratio ($kg_{water}\ kg_{air}^{-1}$), r_T is the total water mixing ratio ($kg_{water}\ kg_{air}^{-1}$), and ε is 0.622 and represents the ratio of the dry air gas constant to the water vapor gas constant.

Both wind shifts and temperature gradients are commonly associated with cold pool passages and have been used when trying to determine cold pool boundary passages in observations [e.g., *Charba*, 1974; *Wakimoto*, 1982; *Engerer et al.,* 2008]. For these simulations, the cold pool boundary was defined at locations that had a surface wind direction shift greater than 45^o over a 10-minute period and a surface $\nabla\theta_\rho$ that was greater than a specified threshold that varied between 1.5 K km^{-1} to 0.1 K km^{-1} depending on the cold pool lifetime; the lowest threshold values were associated with the decaying stages of the MCS event. The $\nabla\theta_\rho$ threshold at each time was calculated based on the values of $\nabla\theta_\rho$ along the cold pool boundary at the prior

time step. The cold pool boundary detection was also insensitive to the specific value of wind direction shift within a reasonable range (25^{o}-65^{o}).

Since MCS cold pool boundaries can often extend for several hundred kilometers, an along-boundary cold pool center was determined in order to ensure that the composite cross sections were calculated on similar samples along the detected cold pool boundary. This cold pool boundary center was based on the centroid of the 500 m density potential temperature behind the cold pool boundary, and therefore, focused the cross section analysis on the most intense region of the cold pool in each simulation at each time step. This methodology is similar to *Trier et al.* [2006], who used the approximate centroids of the leading line convection to determine the center location for cross-section computations for many MCSs. In this study, this centroid calculation was confined to a 10 km distance perpendicular to the propagation direction from the center point at the prior analysis time (5 minutes). Therefore, it was assumed that the cold pool center point does not move more than 5 km in the along-line direction during the 5-minute period between simulated data output. This confinement ensured that a continuous evolution of the same region of the cold pool was assessed. The initial location of the cold pool boundary center point was specified at the same location at the first analysis time for all the simulations. Once the cold pool boundary was determined, composite cross sections relative to the cold pool boundary were created. These cross sections were created by first averaging over 50 km in the along-boundary direction and centered at the calculated cold pool boundary center point, and then averaging the cross sections temporally over a 4-hour time period, beginning approximately when the leading convective lines begin to propagate. These time periods were 0600-1000 UTC for the May 20 event and 0100-0500 UTC for the May 23-24 event. The cross sections were also defined to extend 250 km behind the cold pool boundary and 100 km ahead of

the cold pool boundary, thus, creating a 100 km x 350 km sub-domain that traveled with the leading edge of the MCS convective line. Cross sections created from data within this sub-domain were used in the following sections.

3.3 MCS Event on 20 May 2011

3.3.1. Precipitation Cross Section

The mean hourly precipitation rates for the suite of May 20 simulations are shown as cross sections in Figure 3.5a. A composite cross section of vertical motions and rain mixing ratios for the CTL simulation is shown in Figure 3.5b as a context for the MCS structure, which was largely similar among all the sensitivity simulations. Intense rain rates of ~20-30 mm hr^{-1} occurred within the first 20 km behind the leading cold pool boundary, where convective cells initiated along the cold pool boundary. These initial convective cells developed into mature convective updrafts around ~25 km behind the leading cold pool boundary. These mature convective cells began to weaken and develop into the mesoscale updraft between 50 and 75 km behind the leading cold pool boundary where an expansive stratiform region then extended for another 75 km towards the rear of the MCS.

From Figure 3.5a, the total precipitation amounts over the entire MCS cross section were within 2% of each other for CTL, LL, and ML, and all these simulations produced ~10% more precipitation than CLE. The difference in total, cross section precipitation between the CLE and ML suggests that middle-tropospheric aerosol can become entrained within the MCS and alter precipitation amounts. However, local trends within the cross sections differed from the collective trend summed over the entire cross section. For example, near the cold pool boundary, ML and CLE had more intense precipitation rates than CTL and LL (Fig. 3.5a). Therefore, the

following sections focus on analysis of the microphysical processes active at varying locations within the MCS cross sections.

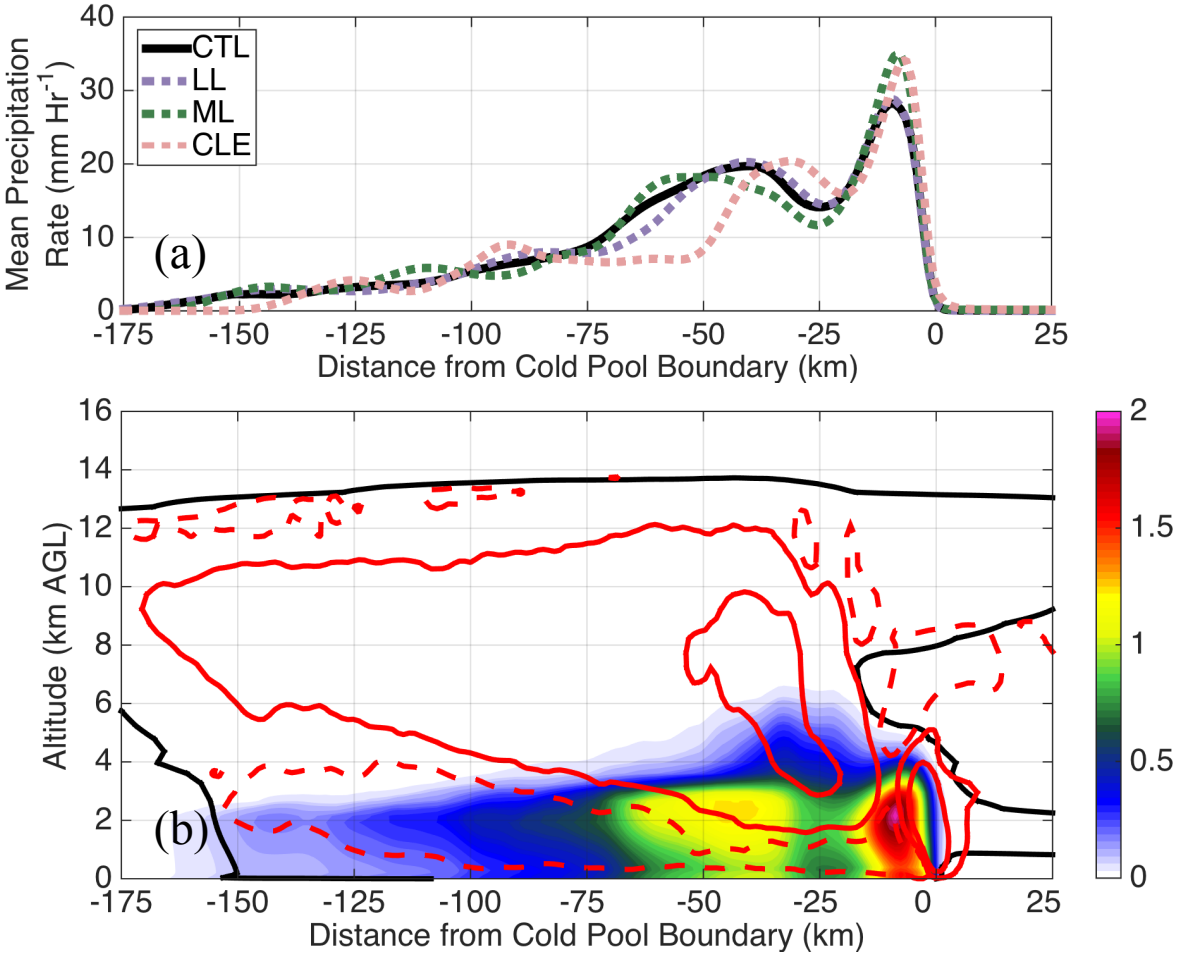

Figure 3.5. (a) Composite cross sections of surface, hourly precipitation rates for the May 20 event simulations. (b) Composite cross section from the May 20 CTL simulation of rain mixing ratio (shaded, g kg^{-1}), with contours of the 0.1 g kg^{-1} total condensate mixing ratio (solid black lines), 0.25 and 1.5 m s^{-1} updrafts (solid red lines), and 0.1 m s^{-1} downdrafts (dashed red lines).

3.3.2. Initial Convective Cells

The first 20 km behind the leading cold pool boundary (i.e., the initial convective cells) contributed between 26% and 33% of the total surface precipitation for the suite of simulations. ML had the highest precipitation rate within this region, which was locally ~24% and ~21%

higher than the maximum precipitation rates in CTL and LL, respectively, while only ~2% higher than the maximum precipitation rate in CLE (Fig. 3.5a). Similarly, the percentage difference in the total precipitation from CTL over this region was +1%, +13%, and +10% for LL, ML, and CLE, respectively. The similarities between CLE and ML and between CTL and LL within the initial convective cells demonstrate that lower-tropospheric aerosol had a stronger influence on precipitation than middle-tropospheric aerosol in this region of the MCS. With fewer aerosol particles, fewer cloud droplets were activated, and these cloud droplets grew faster from condensation to larger sizes, which created higher collision efficiencies and increased drizzle and rain production. This more efficient conversion of cloud mass to rain mass (warm-rain process) in regions with lower aerosol concentrations has been reported in numerous studies

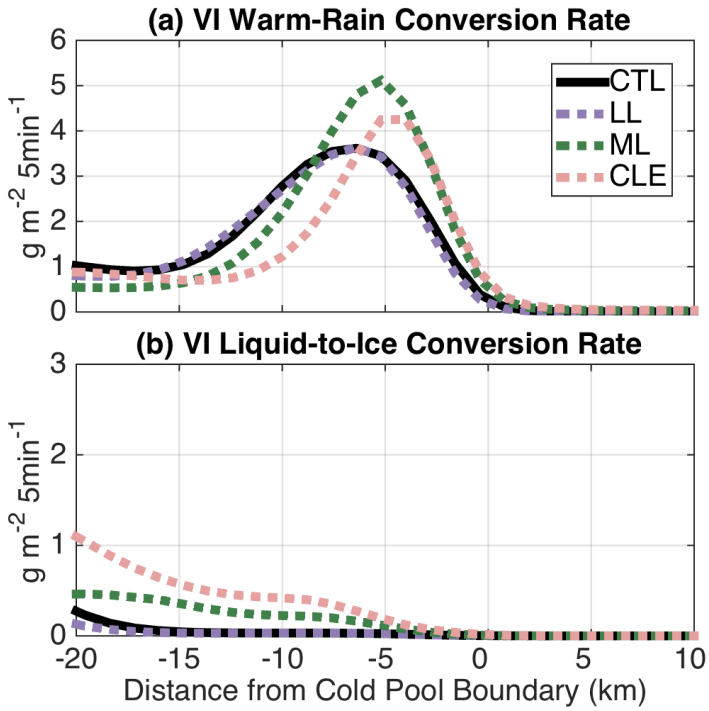

Figure 3.6. Composite cross sections of vertically integrated (VI) microphysical process rates near the cold pool leading boundary for the May 20 event simulations. (a) represents collision coalescence (the conversion of cloud mass to rain mass), and (b) represents riming (the collection of liquid water by ice hydrometeors).

[e.g., *Albrecht*, 1989]. Evaluating the microphysical processes independently (Fig. 3.6) demonstrates that the warm-rain process is predominantly responsible for the increases in intense precipitation rates that were simulated in ML and CLE (Fig. 3.6a), while ice processes played a negligible role (Fig. 3.6b). In LL and CTL, warm-rain processes were not only weaker in magnitude than CLE and ML, but were also shifted several km rearwards from the leading cold pool boundary due to the increased time needed to form rain and the front-to-rear, storm-relative air flow in the propagating MCS.

3.3.3. Convective Updrafts

In order to understand whether middle-tropospheric aerosol were able to become entrained within convective updrafts, as was shown by F04 for tropical convection, mean vertical profiles of cloud properties and processes were calculated at each vertical level over all grid points where the vertical velocity was greater than 10 m s^{-1} (Fig. 3.7). The trends in Figure 3.7 were largely insensitive to a range of the vertical velocity thresholds (e.g., 2-15 m s^{-1}). Within ~0-3 km AGL, the trends in cloud droplet number concentration, diameter, and mixing ratio (Fig. 3.7a-c) follow the changes to warm-rain processes as described in the prior section. With fewer lower troposphere aerosol particles, there were lower concentrations of cloud droplets that grew to larger sizes and were more efficiently converted to rain. However, above 3 km AGL, cloud droplet number concentrations increased with height in ML, while they decreased in height for the other three simulations. This finding suggests that middle-tropospheric aerosol can become entrained within strong convective updrafts and thus initiate secondary nucleation. Between 6 and 9 km AGL, ML had ~50% more cloud droplets within the convective updrafts than CTL and LL. With more cloud droplets (Fig. 3.7a) and similar values of cloud mixing ratio when

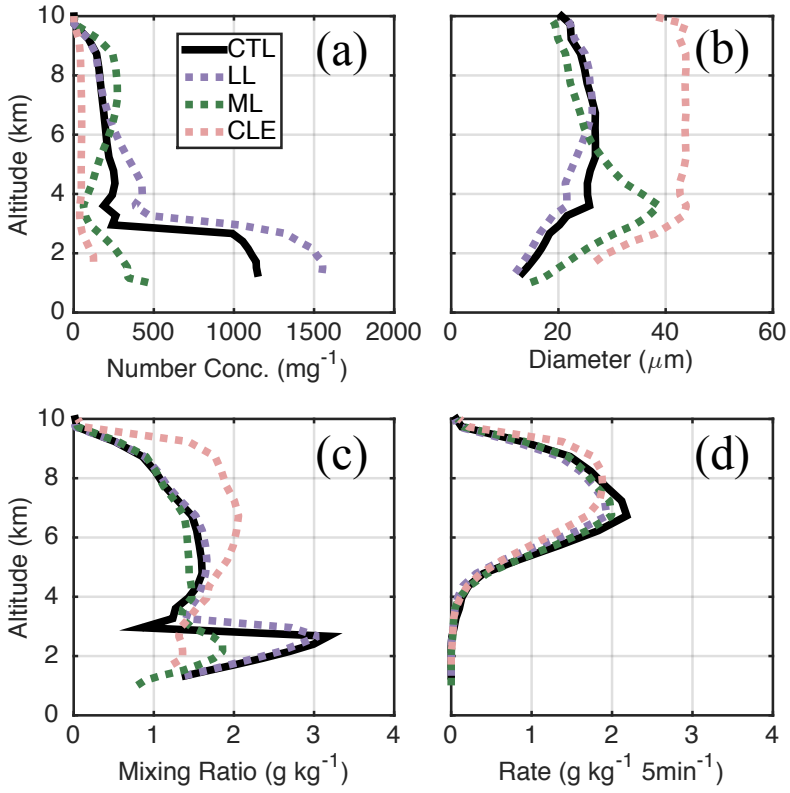

Figure 3.7. Vertical profiles of (a) cloud droplet number concentrations, (b) mean cloud droplet diameter, (c) cloud liquid mixing ratio, and (d) the riming rate of cloud water within the convective updrafts for the May 20 event simulations. Quantities were averaged over all grid points where the vertical velocity was greater than 10 m s^{-1} at each model level in order to represent the averages only over convective updrafts.

compared with the LL and CTL cases (Fig. 3.7c), ML cloud diameters were ~10% smaller than those in LL and CTL within 6 and 9 km AGL (Fig. 3.7b). Due to the large number concentrations of cloud droplets in the LL, CTL, and ML simulations and still sizeable cloud droplet mean diameters (~25 microns), these three simulations had enhanced riming rates (~15-25% higher) compared to CLE between 5 and 7 km AGL (Fig. 3.7d). As a result, more cloud water mass was converted to ice hydrometeors that then precipitated out of the convective updrafts. This process was consistent with the decrease in the precipitation between 50 and 75 km behind the leading cold pool boundary in the CLE simulation (Fig. 3.5a). In CLE, lower

riming rates between 4 and 7 km AGL, led to more cloud water being lofted into the upper portions of the MCS anvil (Fig. 3.7c), where it was converted to pristine ice and was less likely to be collected by other hydrometeors or grow to precipitating ice hydrometeor sizes due to lower supersaturation levels in the upper portions of the cloud. This balance between cloud droplet concentrations and diameters in terms of its impact on riming efficiencies is discussed in greater depth in *Saleeby et al.* [2016]. It is important to note that the rate of the increase of cloud water with height is in part due to the per-mass units, as air density decreases exponentially with height.

3.3.4. Stratiform and Convective Precipitation Processes

Within the composite cross section, a large region of relatively weak precipitation was present 75-175 km behind the leading cold pool boundary (Fig. 3.5a). Due to its expansive size, this region accounted for 22-24% of the total precipitation within the cross section, depending on the simulation. However, due to the small variation in precipitation rates among the simulations, this region's impact on the differences in total precipitation among the simulations was at most 1.5% (difference between CLE and CTL). Due to this minimal impact, the region between 75 and 175 km behind the leading cold pool boundary will not be examined any further in this study.

The region between 20 and 75 km behind the leading cold pool boundary accounted for 48-54% of the total precipitation and had more significant variations among the suite of simulations (Fig. 3.5a). The precipitation within this region was dominated by precipitating ice hydrometeors from the mature and dissipating convective updrafts, although warm-rain processes also contributed to producing rain in this region. The ML and LL simulations both had

precipitation amounts within 5% of CTL over this region, while CLE had ~21% less precipitation than CTL (Fig. 3.5a). Also, the CLE simulation had peak precipitation rates located closer to the leading cold pool boundary, while CTL, ML, and LL had more similar spatial distributions. The general similarities in precipitation rates between ML, LL, and CTL and the difference between ML and CLE demonstrate that middle-tropospheric aerosol can have significant microphysical impacts on MCS precipitation. For this suite of simulations, middle-tropospheric aerosol (ML) produced a similar precipitation response as lower-tropospheric aerosol within this region.

To better understand these changes in precipitation rates, microphysical process rates that were vertically integrated over the depth of the model within the region 20-75 km behind the leading cold pool boundary are shown in Figure 3.8. Condensation, warm-rain production, deposition, and riming rates were all greatest in the CTL simulation (Fig. 3.8a-d). The ML and LL process rates were ~15-25% smaller, depending on the process. More intense updrafts can assist in generating greater magnitudes of supersaturation that would enhance deposition and condensation rates, as well as increase the collision efficiencies of hydrometeors. It is therefore possible that changes in vertical velocities between CTL, LL, and ML may be responsible for these consistent trends in process rates. Figure 3.9 shows vertical profiles of updrafts averaged over all grid points with positive vertical motions within the region from 20 to 75 km behind the leading cold pool boundary. Below 6 km AGL, CTL had the strongest positive vertical motions on average within this region, while above 6 km AGL, CTL had stronger updrafts than LL, but weaker updrafts than ML. These data generally support that stronger vertical motions in CTL were associated with the enhanced precipitation processes. Despite the relatively large decreases in the microphysical process rates in LL and ML as compared to CTL (Fig. 3.8a-d), the total

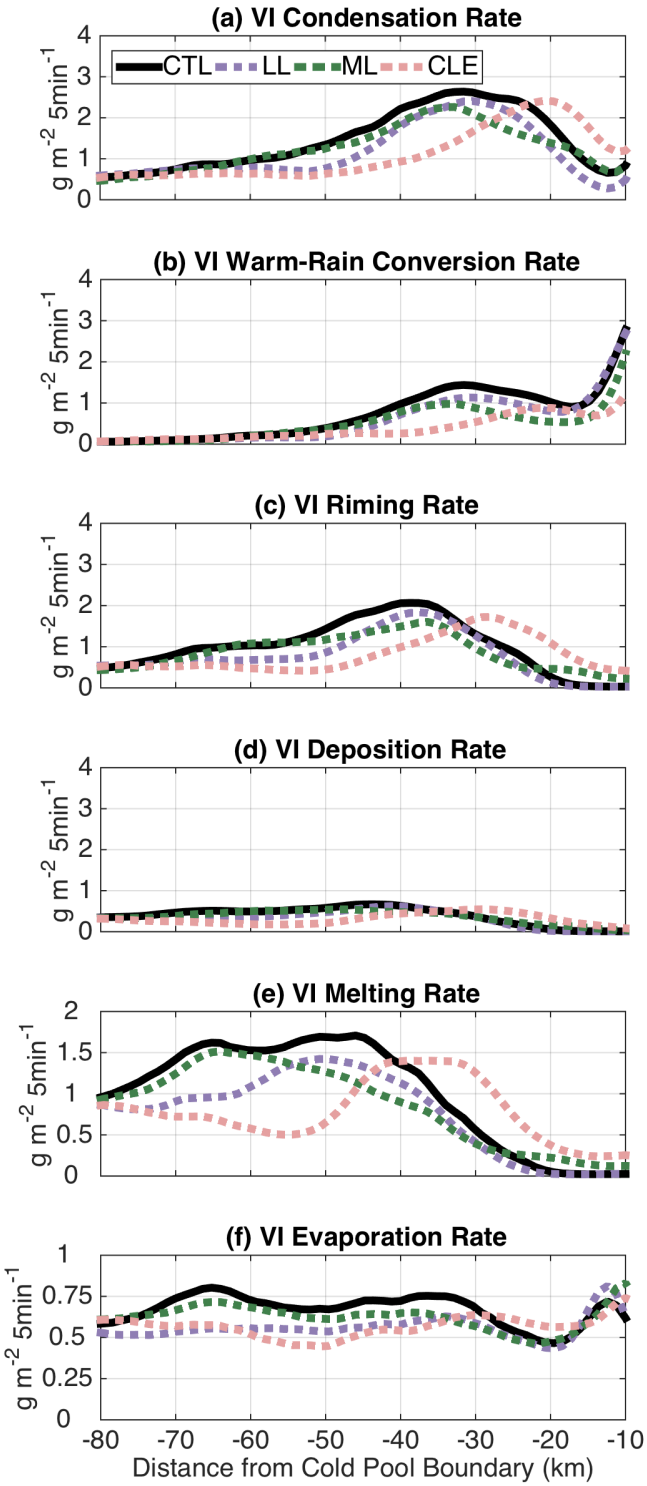

Figure 3.8. Composite cross sections of vertically integrated (VI) microphysical process rates between 10 and 80 km behind the leading cold pool boundary for the May 20 event simulations. (a-f) represent condensation, conversion of cloud water to rain water, the collection of liquid water by ice hydrometeors, deposition, melting, and evaporation, respectively.

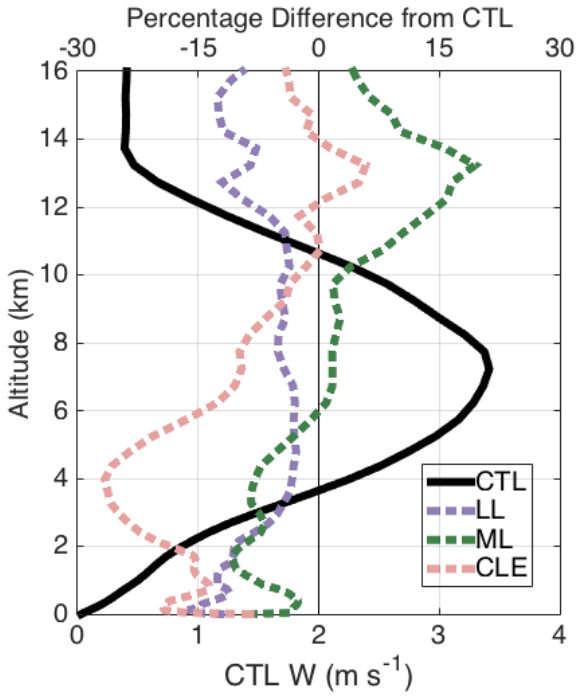

Figure 3.9. Mean vertical profiles of positive vertical velocities (m s^{-1}) averaged between 20 and 75 km behind the leading cold pool boundary for the May 20 event simulations. The bottom axis represents the mean vertical velocity for the CTL simulation (black line), while the top axis represents percentage changes from CTL for the LL, ML, and CLE simulations.

changes in precipitation within this region were less than 5% (Fig. 3.5a). This can partly be explained by the increased evaporation rates that occur in CTL (Fig. 3.8f), which dampened the differences between the in-cloud precipitation processes to create smaller differences in the accumulated surface rainfall.

Averaged over the 20-75 km region, the differences in the precipitation processes rates were even larger (generally, 25-35% decreases) for CLE as compared to CTL (Fig. 3.8a-e). These processes were also generally located ~10-20 km closer to the leading cold pool boundary, consistent with the surface precipitation trends. Lower cloud droplet number concentrations (~80%) and increased cloud water flux into the upper levels of the MCS (Fig. 3.7), as well as the weaker updraft speeds (Fig. 3.9), assisted in reducing these precipitation processes within CLE. While CLE had the smallest raindrops below cloud base within this region (not shown),

evaporation rates were weakest in CLE, demonstrating that to a first order, the rate of evaporation was controlled by the amount of rain produced, as opposed to the size distribution of rain drops.

3.3.5. Cold Pool Feedbacks

Changes to precipitation processes and hydrometeor characteristics can alter the cold pool characteristics, which then can have significant dynamical feedbacks within MCSs [*Tao et al.,* 2007; *Lee et al.*, 2008; *Seigel et al.,* 2013; *Lebo and Morrison*, 2014]. Figure 3.10 shows composite cross sections of density potential temperature (θ_ρ) within the lowest 4 km of the cross section for LL, ML, and CLE as differences from CTL. CLE has positive θ_ρ perturbations from CTL upwards of 0.5 K throughout the first 100 km behind the leading cold pool boundary, while the LL and ML simulations had θ_ρ values that were generally within 0.25 K of CTL throughout the entire cold pool. In this suite of simulations, similarities in the total rainfall amounts among the CTL, LL, and ML resulted in the similar cold pool intensities, while CLE had lower precipitation rates, weaker melting and evaporation rates (i.e., Fig. 3.8e,f), and therefore, a less dense cold pool. It is also hypothesized that a faster and drier rear-inflow jet that was simulated in CLE may have also assisted in creating the warmer cold pool via more intense subsidence warming within the descending portions of the rear-inflow (not shown).

Warmer cold pools propagate at slower speeds as they have weaker temperature gradients across the cold pool boundary, and therefore, weaker pressure gradients that drive the cold pool boundary propagation [*Benjamin*, 1968]. Consistent with this density current theory, the CLE cold pool boundary propagated at slower speeds, as is evident in Figure 3.11, which shows the locations of the cold pool boundary using the tracking methods explained in Section 3.2.3. With

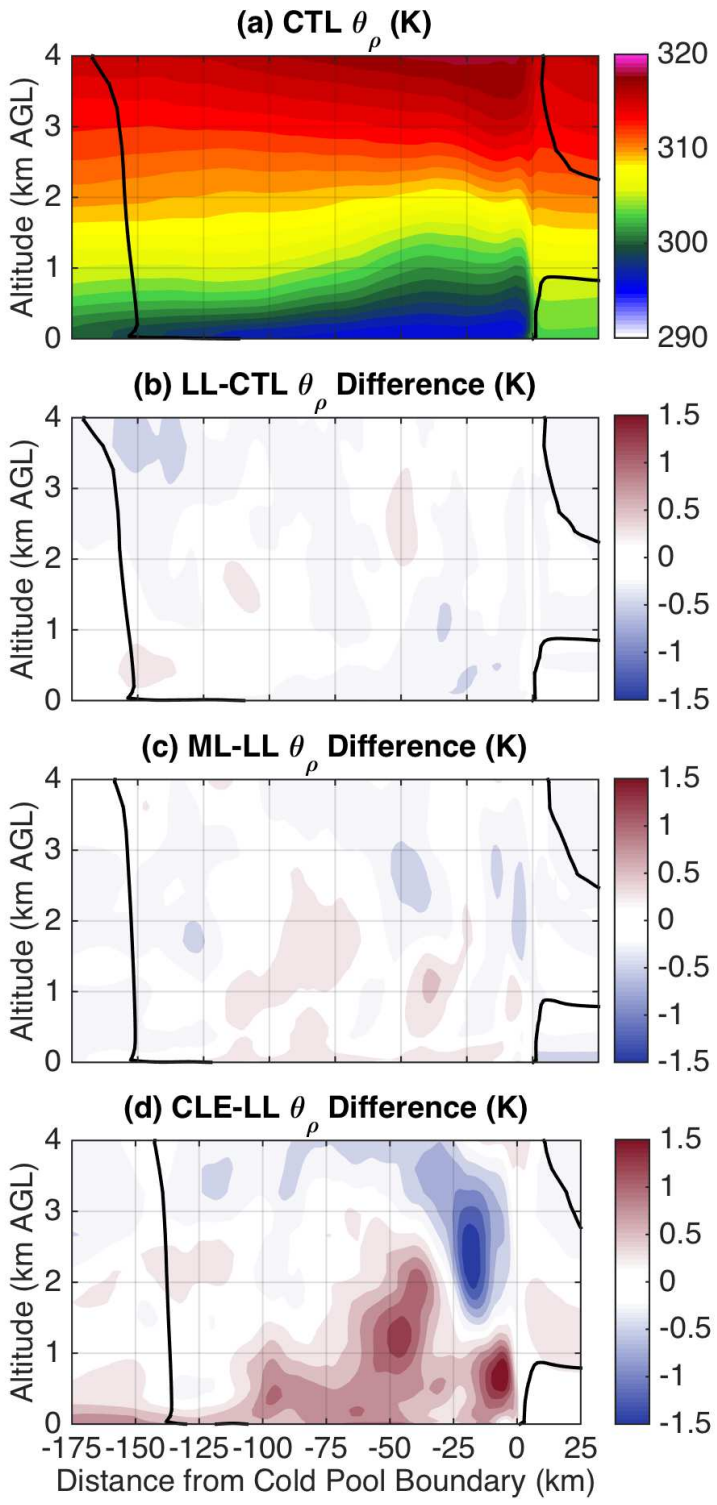

Figure 3.10. Composite cross sections of density potential temperature (θ_ρ) in K for the May 20 simulations. (a) represents θ_ρ for CTL, while (b-d) represent differences in θ_ρ from CTL for LL, ML, and CLE, respectively. The black contour represents the 0.1 g kg^{-1} total condensate mixing ratio.

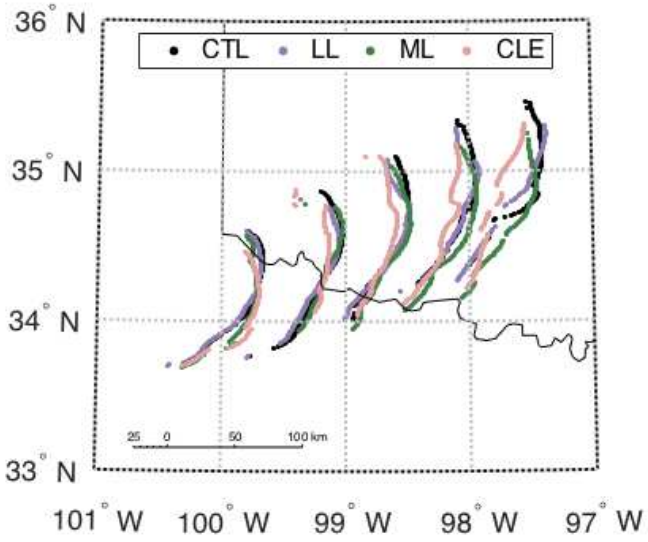

Figure 3.11. Locations of the cold pool leading boundary for the May 20 event simulations, based on the tracking algorithm explained in Section 2.3. Data is shown at hourly intervals beginning with 20 May 0600 UTC. The thin black line is the state border between Texas and Oklahoma.

faster system propagation, the front-to-rear, storm-relative flow was more intense in the CTL, LL, and ML simulations, compared to the CLE simulation. Therefore, more water vapor, condensate, and vertical momentum was transported from the mature convective updrafts rearwards. Updrafts that were more erect throughout the depth of the cloud system in CLE, as can be seen in Figure 3.12, are further evidence of this. Faster cold pool propagation speeds in CTL, ML, and LL also enhanced rearward transport of both vertical momentum and water from the convective updrafts into the region between 20 and 75 km behind the leading cold pool boundary, which largely explained the enhanced region of precipitation in CTL, ML, and LL, as compared to CLE.

While the trends above represent the primary variations in precipitation and cold pool feedbacks through cross section composites, it is also important to understand changes to the spatial distribution of precipitation associated with these simulated MCSs. Figure 3.13 shows maps of accumulated precipitation for all four events during the mature stage analyzed here.

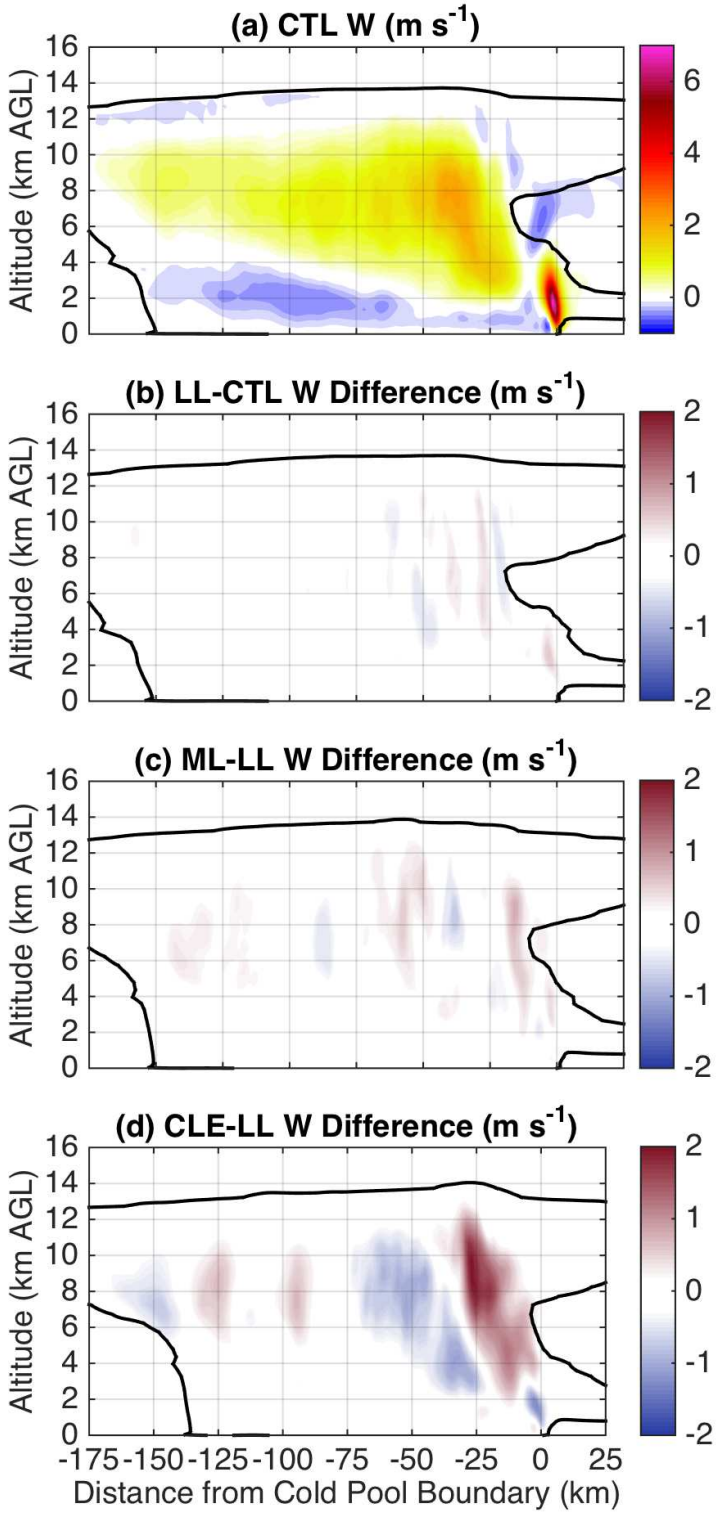

Figure 3.12. Composite cross sections of vertical velocity (m s^{-1}) for the May 20 simulations. (a-d) represent data from CTL, LL, ML, and CLE, respectively. The black contour represents 0.1 g kg^{-1} total condensate mixing ratio.

Consistent with the above analysis, CLE (Fig. 3.13d) had lower accumulated precipitation than CTL, LL, and ML. However, along the southern edge of the leading MCS boundary, there was enhanced precipitation in both the ML and CLE cases. This result is also consistent with Figure 3.11, which depicts that along the southernmost boundary of the cold pool leading edge, the ML and CLE cold pool locally propagates faster than CTL and LL. The enhanced, southern precipitation in ML and CLE was present from the beginning of the time period analyzed here and may be associated with enhanced warm-rain processes and an earlier development of the cold pool when the initial storms associated with this MCS formed. Since this MCS generally

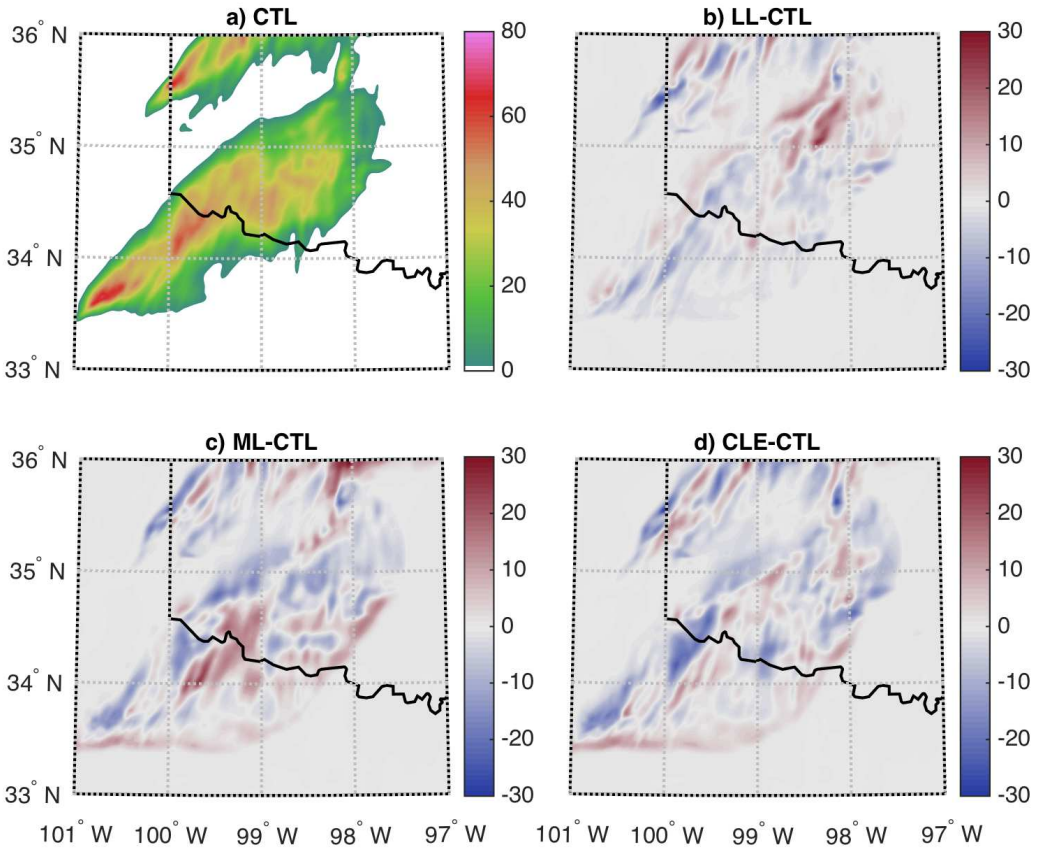

Figure 3.13. Maps of accumulated precipitation (mm) from 0600 UTC through 1000 UTC on 20 May for (a) CTL, (b) LL difference from CTL, (c) ML difference from CTL, and (d) CLE difference from CTL.

propagates northeastward during the initial and mature stages, enhanced precipitation and cold pool development at the early stages may favor the southern region of the MCS. This spatial shift in precipitation and cold pool intensity further demonstrates the complexity of microphysical-dynamical feedbacks within MCSs.

3.4 Comparisons to the 23-24 May 2011 event

A second MCS event that occurred on 23-24 May 2011 during MC3E was simulated to assess whether the changes in MCS precipitation from vertically varying aerosol profiles found for the May 20 case study can be more broadly applied to other MCS events. A cross section of precipitation rates for the May 23-24 simulations is shown in Figure 3.14, as well as a cross

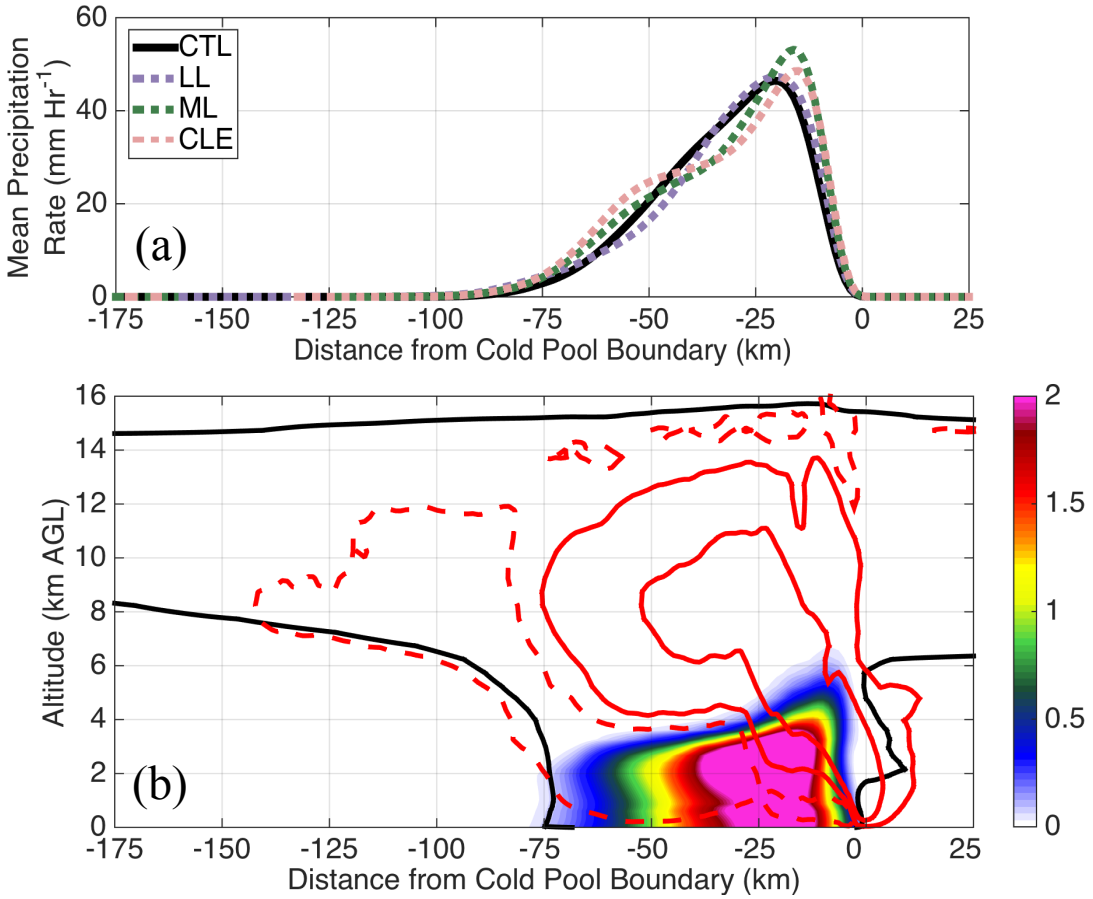

Figure 3.14. Same as Figure 3.5, but for the May 23-24 event simulations.

section of the MCS structure from the May 23-24 CTL simulation. The total change in the cross section precipitation for this event when compared with CTL was +1.3%, +7.5%, and +8.0% for LL, ML, and CLE, respectively. Therefore, for the May 23-24 event simulations, the ML and CLE were much more alike in terms of total precipitation changes (~0.5%), as compared to the May 20 event, where they differed by ~10%. This difference in trends suggests that the role of middle-tropospheric aerosol on MCS precipitation may be highly dependent on the specific MCS event.

Despite the fact that these two MCSs both had leading-line, trailing-stratiform structures during their mature stage, formed in a similar region, and occurred only a few days apart, their structures were very different (compare Fig. 3.5b and Fig. 3.14b). These structural differences can be largely explained by differences in their environments (Table 3.1). The mature May 23-24 MCS propagated into an environment with lower convective available potential energy

Table 3.1. Environment characteristics ahead of the MCS leading cold pool boundary for both event simulations. Values were computed from composite cross sections and were based on the mean profiles within the region 25-50 km ahead of the leading cold pool boundary for the CTL simulations.

	May 20 MCS	May 23-24 MCS
Most Unstable CAPE (J kg^{-1})	2574	1599
Convective Inhibition (J kg^{-1})	3.5	23.4
Surface temperature (K)	297.8	303.7
Surface water vapor (g kg^{-1})	17.1	13.5
0.5-3.0 km shear (m s^{-1})	7.2	15.1
0.5-6.0 km shear (m s^{-1})	10.1	21.3
Lifting Condensation Level (km)	1.2	1.8

(CAPE) but stronger unidirectional wind shear than the May 20 event, which caused more intense and erect updrafts throughout the depth of the cloud system as seen in Figure 3.14b, as compared to the mature May 20 MCS (Fig. 3.5b). The stratiform region was much smaller in the May 23-24 MCS, and convective precipitation processes contributed the majority of total

precipitation in the simulated May 23-24 event. Also, the May 23-24 MCS cloud base occurred at ~2 km AGL versus ~1 km AGL for the May 20 event, while the freezing levels were ~4 km AGL for both events. Therefore, the depth of the warm-phase region for the May 20 event was larger. The differences in environmental conditions between the May 20 and May 23-24 events assist in explaining the differences in aerosol effects on precipitation between these two MCS events. This finding is consistent with other studies that have shown in more idealized settings that the impacts of aerosol particles on deep convection are highly dependent on the environmental conditions [e.g., *Tao et al.*, 2007; *Khain et al.*, 2008; *Fan et al.*, 2009; *Storer et al.*, 2010].

However, there were also several similarities between the two simulations that suggest some generality of the roles of lower-tropospheric and middle-tropospheric aerosol on MCS precipitation. Near the cold pool leading boundary, similar magnitudes and trends of warm-rain

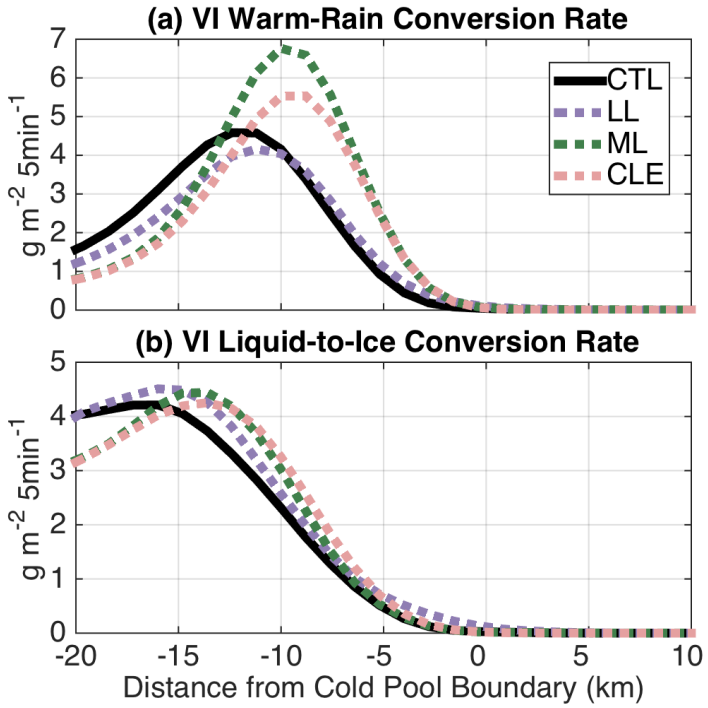

Figure 3.15. Same as Figure 3.6, except for the May 23-24 event simulations.

processes among the sensitivity simulations occurred between the two MCS events (Figs. 3.6 and 3.15). However, due to the more upright updrafts lifted from the cold pool boundary through the upper levels of the May 23-24 MCS (see Fig. 3.14b), ice processes played a more significant role within the region near the leading cold pool boundary (compare Fig. 3.15b and Fig. 3.6b), which enhanced precipitation rates.

It also appears that middle-tropospheric aerosol particles were entrained within the convective updrafts of the May 23-24 MCS (Fig. 3.16), though to a lesser extent than the May 20 event (compare Fig. 3.7 with Fig. 3.16). This may be in part due to the fact that the May 23-24 MCS event had updrafts that were less susceptible to entrainment, as they were more upright and intense [e.g., *Gregory,* 2001]. Another factor that may have impacted the lower cloud droplet

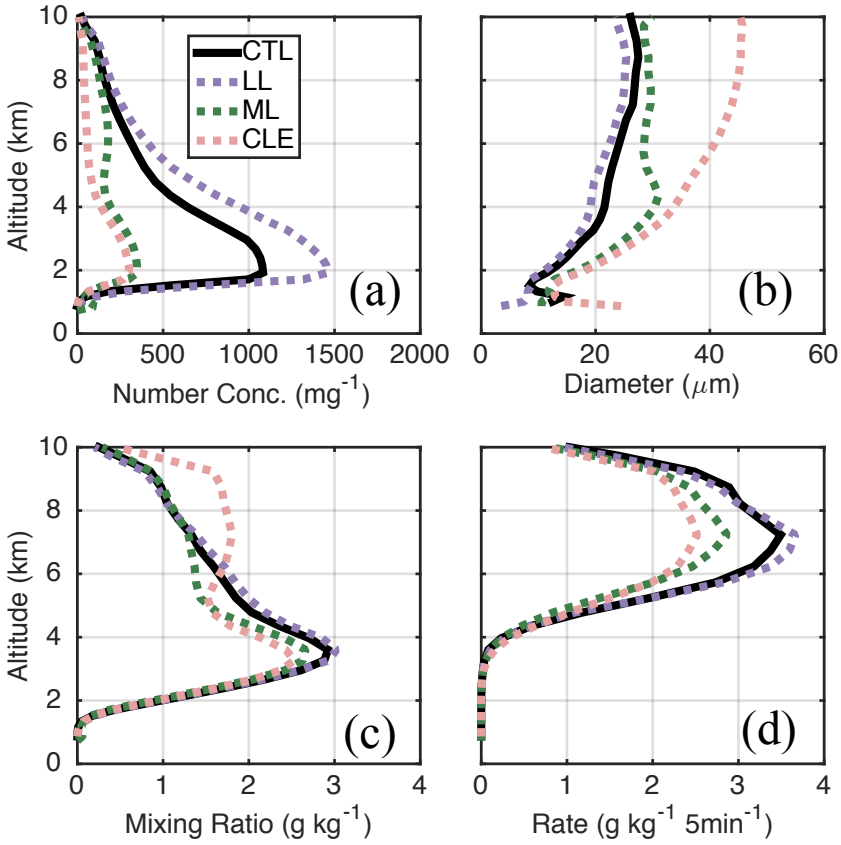

Figure 3.16. Same as Figure 3.7, except for the May 23-24 event simulations.

number concentrations within the ML convective updrafts for the May 23-24 event (Fig. 3.16a), as compared to the May 20 event, was a more significant removal of middle-tropospheric aerosol in the environment ahead of the leading cold pool boundary (Fig. 3.17). Between 4 and 9 km, the vertically integrated aerosol mass in the environment ahead of the cold pool boundary was reduced to ~56% and ~41% of the initialization values, for the May 20 and May 23-24 events, respectively. Therefore, there was ~15% fewer aerosol particles in the middle-to-upper troposphere in the May 23-24 simulation, as compared to the May 20 simulation.

Despite still significant middle-tropospheric aerosol particle entrainment within the convective updrafts (Fig. 3.16), the total precipitation response in the ML simulation was very similar to CLE. This suggests that for the May 23-24 event, lower-tropospheric aerosol concentrations were a more important control on MCS precipitation than middle-tropospheric aerosol concentrations. Furthermore, despite similar differences in precipitation among the May 23-24 and May 20 event simulations, the varying cold pool feedbacks that was examined in

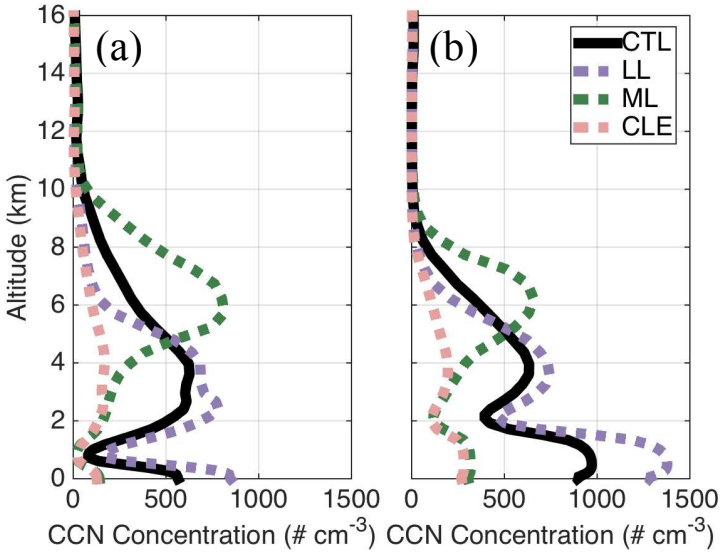

Figure 3.17. Cloud condensation nuclei (CCN) vertical profiles ahead of the mature MCS cold pool leading boundary for (a) the May 20 event and (b) the May 23-24 event simulations. These profiles were computed as an average from the composite cross section over the region 25 to 50 km ahead of the cold pool leading boundary.

Section 3.3.5 for the May 20 event simulations were not present in the May 23-24 event simulations. Collectively, these trend differences between the two simulated MCS events suggest that the impact of middle-tropospheric and lower-tropospheric aerosol on total MCS precipitation is largely controlled by the structure of the MCS and the ambient environmental conditions.

3.5 Conclusions

The goal of this study was to assess the relative roles of middle-tropospheric and lower-tropospheric aerosol on MCS precipitation during the mature stage of the storm lifecycle. Two leading convective line, trailing stratiform MCSs from the MC3E field campaign (May 20 and May 23-24 events) were simulated with RAMS. These MC3E MCS events were especially relevant for this study since expansive biomass burning events in Central America and Mexico occurred concurrently with MC3E, and biomass burning aerosol particles from this region were advected into the southern United States within both the lower and middle troposphere.

Meteorological reanalysis and aerosol data during MC3E were used to constrain the MCS simulations. For each MCS event, simulations were initialized with different aerosol profiles in which the vertical location of the aerosol particle number concentrations was varied, while keeping the total vertically integrated aerosol mass constant. In this way, changes to MCS precipitation between the simulations could be more directly attributed to the vertical variations in aerosol particle concentrations, as opposed to the amount of aerosol. Composite cross sections relative to the propagating, leading cold pool boundary were used to quantify and understand changes in precipitation between the simulations.

Several aerosol-induced impacts on precipitation were evident in both case studies that may also be applicable to other MCSs. It was found that lower-tropospheric aerosol had a consistent microphysical control on precipitation directly behind the leading cold pool boundary for both simulated events, regardless of different dynamic feedbacks that were evident in the simulations. Fewer aerosol generally caused enhanced precipitation rates in the first 20 km behind the leading cold boundary during the mature stage of the MCS event. This precipitation rate intensification was primarily a result of warm-rain processes, but was further enhanced by ice processes in the May 23-24 event. A second consistent trend between the two MCS events was that middle-tropospheric aerosol were entrained within convective updrafts, thus altering the cloud droplet properties in a similar manner to simulations with peak aerosol concentrations in the lower troposphere.

Despite these similarities in the two case studies, the trends in total mature-stage MCS precipitation differed between the two MCS events. For the May 20 event, the CTL, ML, and LL all had very similar precipitation totals, being driven by precipitation rates within and rearwards of the mature convective updraft region. Although the accumulated precipitation differed little between CTL, ML, and LL, the distribution of precipitation within the cross section was more variable, especially within the first 20 km behind the cold pool leading boundary, where the ML and CLE simulations produced 10-15% more surface rainfall. For the May 23-24 MCS, the ML simulation produced precipitation trends that were more similar to CLE, suggesting that middle-tropospheric aerosol, despite becoming entrained within the convective updrafts, had a less significant impact on total precipitation. It is hypothesized that these differences are due to changes in the MCS structure between the two event simulations, which were largely controlled by changes in the environmental conditions.

Microphysics-dynamics feedbacks were also important factors in the precipitation changes between the simulations. For the May 20 event, the CLE simulation had lower precipitation amounts, which caused weaker cold pools, which resulted in less rearward transport of vertical momentum and water, and thus continued lower precipitation amounts. Such strong feedbacks were not discernable in the May 23-24 event, despite similar changes in precipitation amounts between the simulations, further highlighting the complexities introduced by MCS structure and environmental conditions in the relationships between aerosol particle concentrations and MCS precipitation.

Lastly, this study demonstrates that aerosol-induced precipitation changes within leading line, trailing stratiform MCSs can vary depending on the distance from the cold pool boundary. The air flows and precipitation processes within leading line, trailing stratiform MCSs have been widely studied for decades [e.g., *Fritsch and Forbes*, 2001; *Houze*, 2004], and assessing aerosol impacts along these well-understood air flows or within specific MCS regions (i.e., convective versus stratiform) may provide additional insights of the aerosol-precipitation interactions within leading line, trailing stratiform MCSs.

Each year, significant biomass burning events transport smoke aerosol particles into the southern United States, and the vertical location of the primary aerosol particle transport pathway varies. This scenario of aerosol particle transport at varying vertical levels is ubiquitous across the globe [e.g., *Berg et al.*, 2016]. While aerosol particles in the middle and upper troposphere can have significant radiative effects on clouds and the environments in which clouds develop [e.g., *Ackerman et al.*, 2000], this study, along with others [*Fridlind et al.*, 2004; *Lebo*, 2014] have shown that these aerosol particles can also become entrained within deep convective updrafts and alter the microphysical and dynamical processes within deep convective systems.

Future work should assess the magnitudes and feedbacks of both radiative and microphysical impacts of middle-tropospheric and upper-tropospheric aerosol particles on deep convective systems, as has been done for lower-tropospheric aerosol particles [e.g., *Seigel et al.*, 2013].

CHAPTER 4: CONCLUDING REMARKS

4.1 Main Conclusions

Mesoscale convective systems (MCSs) have local, regional, and global impacts on weather and climate. For this reason, it is important to accurately represent these systems in atmospheric models. However, large-scale atmospheric models, such as global climate models (GCMs), have had difficulties simulating MCSs and their impacts on the Earth system, which is primarily due to the convective parameterizations that are used in these models. The Midlatitude Continental Convective Clouds Experiment (MC3E) was organized to provide an observational dataset that can be used to better understand the physical processes underlying these convective systems in order to assist in the improvements of these parameterizations [*Jensen et al.*, 2015]. The overarching objective of the research presented here, which was aligned with the motivations behind MC3E, was to provide an enhanced understanding of the microphysical processes within MCSs.

Within this thesis, simulations of two MCS events (20 May 2011 and 23-24 May 2011) that occurred during the MC3E were conducted using the Regional Atmospheric Modeling System (RAMS) and investigated. Although they evolved in diverse environments, both MCSs developed a leading-line, trailing stratiform structure and produced extensive rainfall and severe weather over the southern Great Plains region of the United States. Comparing simulated precipitation, convective updraft strengths, and MCS convective and stratiform areas to observations from MC3E, it was concluded that these two simulations reasonably reproduced the observed MCS events and could therefore be used to gain insights into the microphysical processes within these convective systems.

Latent heating within MCSs was the focus of Chapter 2. The vertical profiles of latent heating within different regions of MCSs (i.e., convective and stratiform) have markedly different structures [e.g., *Kuo and Anthes*, 1984; *Gallus and Johnson*, 1991]. These differences in convective and stratiform latent heating profiles induce many of the internal processes within MCSs and the impacts that MCSs have on the ambient environment. To better understand this vertical structure of latent heating within MCSs, mean profiles of latent heating were computed for convective, stratiform, and anvil regions for the two simulated MCSs over a 12-hour period. These latent heating profiles were further separated into the different microphysical processes that generated the latent heating. From this analysis it was found that condensation and deposition were the primary causes of positive latent heating or latent warming. Evaporation, melting, and sublimation each caused similar peak latent cooling (i.e., negative latent heating) rates, which occurred at varying altitudes depending on the process. Riming and cloud and ice nucleation processes played relatively negligible roles in latent heating over the entire MCS system.

The evolution of MCS latent heating was also assessed. Development, mature, and decay stages were classified from the 12-hour analysis period. Latent heating rates within convective regions decreased from the development stage through the decay stage at an approximately linear rate, while stratiform regions demonstrated more abrupt changes to the latent heating profiles with time, which were associated with changes to the flow regimes within the different stages of the MCS lifecycle. As the MCS transitioned from the development to the mature stage, front-to-rear, ascending, storm-relative flow increased, which strengthened stratiform latent warming rates and lowered the altitude of stratiform latent cooling. In the decay stages, the descending rear-inflow jet of the MCS assisted in creating increased stratiform cloud development, which

induced an intense vertical gradient in latent heating in the middle troposphere. This vertical gradient in latent heating has implications for the development of mesoscale convective vortices.

In Chapter 3, the relative roles of cloud-nucleating aerosol particles in the lower and middle troposphere on mature-stage MCS precipitation were explored. The mature stage was chosen, since the majority of precipitation from MCSs occurs during the mature stage [e.g., *Houze,* 1977; *Watson et al.*, 1988]. For each MCS event, three simulations were conducted with different initialization aerosol profiles that varied only in the vertical location of peak aerosol concentrations. These three aerosol profiles had the same vertically integrated aerosol mass and number at initialization, such that trends in the simulations could be more directly attributed to the vertical variation of aerosol particles, as opposed to the total mass and number of aerosol particles. These aerosol profiles were initialized horizontally-homogenously throughout the domain, and the aerosol particles were chosen to be radiatively inactive so as to isolate microphysical impacts. A fourth simulation that was initialized with an aerosol profile consisting of fewer aerosol was also run for each MCS event and was used as a benchmark to assist in the analysis.

The simulations demonstrated that lower-tropospheric aerosol particles controlled precipitation within the first 20 km behind the leading cold pool boundary, which was primarily a result of the changes to warm-rain production rates. In both MCS events, evidence that middle-tropospheric aerosol particles were entrained and nucleated within the MCS system was present. However, the ultimate effect on total surface precipitation from the MCSs was inconsistent between the two simulations. This inconsistency was attributed to the differences in the storm structure and environments between the two MCS events. Microphysical-dynamical feedbacks

within MCSs further inhibited the ability to generalize how aerosol particles ultimate change the surface accumulated precipitation within mature MCSs.

4.2 Applications

The results of Chapters 2 and 3 can ultimately be used to assist in the development of parameterizations within atmospheric models. CRM simulations have often been used as a tool in developing parameterizations, providing that the simulations accurately represent the atmospheric phenomenon of interest [e.g., *Alexander and Cotton*, 1998; *Del Genio et al.*, 2012]. Therefore, since the two MCS event simulations reasonably reproduced the observed MCS events (Chapter 2), these simulations can also be used to assist in the development of parameterizations.

Figures 1 and 2 in *Del Genio et al.* [2012] demonstrate inconsistencies between GCM and satellite-derived latent heating rates in the tropics. Latent heating rates are fundamental to a variety of atmospheric processes [e.g., *Hartmann et al.*, 1984; *Mapes*, 1993], and therefore, latent heating rates are often used as a benchmark to test the validity of GCM simulations. As GCM parameterizations are further developed to include additional prognostic variables that incorporate the mesoscale development of cloud systems, as proposed in *Del Genio et al.* [2012], the latent heating rate evolution described in Chapter 2 could also provide a useful benchmark for these parameterizations.

How aerosol particles interact with clouds continues to be a large source of uncertainty in climate models [*Intergovernmental Panel on Climate Change* (*IPCC*), 2013]. Chapter 3 of this thesis demonstrated that both lower-tropospheric and middle-tropospheric, cloud-nucleating aerosol particles can significantly impact MCS precipitation and cloud properties. Many GCMs

have parameterizations that incorporate aerosol particle activation to cloud droplets; however, this cloud droplet nucleation calculation occurs at cloud base [e.g., *Lohmann et al.*, 1999]. Aerosol particles can become laterally entrained within MCS convective updrafts at altitudes above cloud base as shown in Chapter 3 of this thesis and in other studies [*Fridlind et al.*, 2004; *Lebo* 2014]. Therefore, for atmospheric models to properly simulate cloud characteristics and processes, these models should incorporate the cloud-nucleating ability of middle-tropospheric and upper-tropospheric aerosol particles.

4.3 Future Work

This work can be extended along various pathways that would enhance either the understanding of convective cloud processes or the representation of cloud processes within atmospheric models. In the prior section, several applications towards the improvement of cloud parameterizations were provided. Future work could involve collaborations with the developers of these parameterizations. More specifically, other variables, in addition to latent heating rates, could be calculated that would be necessary for a comprehensive, convective parameterization, such as moisture and heat sinks and sources, vertical velocities, and hydrometeor mixing ratio, as suggested in *Del Genio et al.*, [2012]. Other MCS events from MC3E and other field campaigns could also be simulated, in order to create a larger sample of events on which to base these parameterization efforts.

These results presented in this thesis have also demonstrated that both cloud-nucleating aerosol particles in the lower troposphere and middle troposphere can become ingested into MCSs and alter MCS mature-stage precipitation. However, the specific trajectories that these aerosol particles follow as they become entrained within the MCS are less clear. Answering

questions such as what fraction of aerosol particles enter the MCS from different atmospheric levels and what role the rear-inflow jet plays in advecting aerosol particles from the rear of these MCSs would provide further insights on the impacts of middle-tropospheric and upper-tropospheric cloud-nucleating aerosol particles on MCS microphysical processes. Tracers and/or trajectory analysis can be implemented within RAMS to assist in answering these questions, as was done for idealized, tropical convection in *McGee and van den Heever* [2014].

The cloud-nucleating aerosol particles in these simulations were chosen to be radiatively inactive in order to isolate the microphysical impacts of the aerosol particles on the MCSs. However, aerosol particles absorb, scatter, reflect, and emit radiation, which have also been shown to play important roles in cloud development [e.g., *Ackerman et al*., 2000]. Furthermore, aerosol layers in the middle and upper troposphere, such as in the ML simulations in Chapter 3, can radiatively impact the stability of the environment and resulting atmospheric and cloud dynamics [*Koch and Del Genio*, 2010]. Future work could involve running a similar suite of simulations as was done in Chapter 3, but with radiatively active aerosol particles in order to determine the relative microphysical, radiative, and synergistic impacts of aerosol particles on MCSs, as has been done for lower-tropospheric aerosol particles [*Seigel et al.*, 2013].

The vertical variation of cloud-nucleating aerosol particles was studied in the context of biomass burning events in this thesis. It is has also been observed that other aerosol species, such as dust, can also be transported great distances from their source regions in the middle and upper levels of the troposphere [e.g., *Prospero and Lamb*, 2003]. Furthermore, dust particles are also efficient ice-nucleating particles [*DeMott et al.*, 2003]. Therefore, additional work could incorporate the changes to ice nuclei number concentrations for the suite of simulations in Chapter 3 and investigate the resulting implications on MCS cloud properties and processes.

This future work section demonstrates the complexities involved in understanding the ultimate impact of aerosol particles on MCSs. In a review of aerosol impacts on convective clouds, *Tao et al.* [2012] stated that "While individual endeavors have advanced our understanding [of aerosol-cloud-precipitation interactions] substantially, it is highly recommended that a collective approach incorporating the strengths of all individual approaches while minimizing their limitations be undertaken to tackle the problem."

REFERENCES

Ackerman, A. S. (2000), Reduction of Tropical Cloudiness by Soot, *Science*, *288*(5468), 1042–1047.

Adams-Selin, R. D., and R. H. Johnson (2013), Examination of Gravity Waves Associated with the 13 March 2003 Bow Echo, *Mon. Weather Rev.*, *141*(11), 3735–3756.

Adams-Selin, R. D., S. C. van den Heever, and R. H. Johnson (2013b), Sensitivity of Bow-Echo Simulation to Microphysical Parameterizations, *Weather Forecast.*, *28*(5), 1188-1209.

Albrecht, B. A. (1989), Aerosols, cloud microphysics, and fractional cloudiness, *Science*, *245*, 1227–1230.

Alexander, G. D., and W. R. Cotton (1998), The Use of Cloud-Resolving Simulations of Mesoscale Convective Systems to Build a Mesoscale Parameterization Scheme, *J. Atmos. Sci.*, *55*(12), 2137–2161.

Andrews, E. (2004), In situ aerosol profiles over the Southern Great Plains cloud and radiation test bed site: 1. Aerosol optical properties, *J. Geophys. Res.*, *109*(D6), D06208.

Augustine, J. A., and F. Caracena (1994), Lower-Tropospheric Precursors to Nocturnal MCS Development over the Central United States, *Weather Forecast.*, *9*(1), 116–135.

Benjamin, T. B. (1968), Gravity currents and related phenomena, *J. Fluid Mech.*, *31*, 209–248.

Berg, L. K. et al. (2016), The Two-Column Aerosol Project: Phase I-Overview and impact of elevated aerosol layers on aerosol optical depth, *J. Geophys. Res.*, *121*(1), 336–361.

Braun, S. A., and R. A. Houze (1996), The Heat Budget of a Midlatitude Squall Line and Implications for Potential Vorticity Production, *J. Atmos. Sci.*, *53*(9), 1217–1240.

Bretherton, C. S., and P. K. Smolarkiewicz (1989), Gravity Waves, Compensating Subsidence and Detrainment around Cumulus Clouds, *J. Atmos. Sci.*, *46*(6), 740–759.

Caniaux, G., J.-L. Redelsperger, and J.-P. Lafore (1994), A Numerical Study of the Stratiform Region of a Fast-Moving Squall Line. Part I: General Description and Water and Heat Budgets, *J. Atmos. Sci.*, *51*(14), 2046–2074.

Charba, J. (1974), Application of Gravity Current Model to Analysis of Squall-Line Gust Front, *Mon. Weather Rev.*, *102*(2), 140–156.

Cheng, W. Y. Y., and W. R. Cotton (2004), Sensitivity of a Cloud-Resolving Simulation of the Genesis of a Mesoscale Convective System to Horizontal Heterogeneities in Soil Moisture Initialization, *J. Hydrometeorol.*, *5*(5), 934–958.

Churchill, D. D., and R. A. Houze (1984), Development and Structure of Winter Monsoon Cloud Clusters On 10 December 1978, *J. Atmos. Sci.*, *41*(6), 933–960.

Collis, S., A. Protat, P. T. May, and C. Williams (2013), Statistics of Storm Updraft Velocities from TWP-ICE Including Verification with Profiling Measurements, *J. Appl. Meteorol. Climatol.*, *52*(8), 1909–1922.

Cotton, W. R., G. D. Alexander, R. Hertenstein, R. L. Walko, R. L. McAnelly, and M. Nicholls (1995), Cloud venting — A review and some new global annual estimates, *Earth-Science Rev.*, *39*(3-4), 169–206.

Cotton, W. R., G. H. Bryan, and S. C. van den Heever (2011), Storm and Cloud Dynamics, 809 pp., 2nd ed., Academic Press, San Diego, Calif.

Cotton, W. R. et al. (2003), RAMS 2001: Current status and future directions, *Meteorol. Atmos. Phys.*, *82*(1), 5–29.

Cram, J. M., R. A. Pielke, and W. R. Cotton (1992), Numerical Simulation and Analysis of a Prefrontal Squall Line. Part II: Propagation of the Squall Line as an Internal Gravity Wave, *J. Atmos. Sci.*, *49*(3), 209–225.

Davis, C. A., D. A. Ahijevych, and S. B. Trier (2002), Detection and Prediction of Warm Season Midtropospheric Vortices by the Rapid Update Cycle, *Mon. Weather Rev.*, *130*(1), 24–42.

DeMott, P. J. (2003), African dust aerosols as atmospheric ice nuclei, *Geophys. Res. Lett.*, *30*(14), 1732.

DeMott, P. J., A. J. Prenni, X. Liu, S. M. Kreidenweis, M. D. Petters, C. H. Twohy, M. S. Richardson, T. Eidhammer, and D. C. Rogers (2010), Predicting global atmospheric ice nuclei distributions and their impacts on climate, *Proc. Natl. Acad. Sci.*, *107*(25), 11217–11222.

Dolan, B., and S. A. Rutledge (2010), Using CASA IP1 to Diagnose Kinematic and Microphysical Interactions in a Convective Storm, *Mon. Weather Rev.*, *138*(5), 1613–1634.

Donner, L. J. (1993), A Cumulus Parameterization Including Mass Fluxes, Vertical Momentum Dynamics, and Mesoscale Effects, *J. Atmos. Sci.*, *50*(6), 889–906.

Donner, L. J., C. J. Seman, R. S. Hemler, and S. Fan (2001), A Cumulus Parameterization Including Mass Fluxes, Convective Vertical Velocities, and Mesoscale Effects: Thermodynamic and Hydrological Aspects in a General Circulation Model, *J. Clim.*, *14*, 3444–3463.

Doswell, C. A., H. E. Brooks, and R. A. Maddox (1996), Flash Flood Forecasting: An Ingredients-Based Methodology, *Weather Forecast.*, *11*(4), 560–581.

Duncan, B. N., R. V. Martin, A. C. Staudt, R. Yevich, and J. A. Logan (2003), Interannual and seasonal variability of biomass burning emissions constrained by satellite observations, *J. Geophys. Res.*, *108*(D2), 4040.

Engerer, N. A., D. J. Stensrud, and M. C. Coniglio (2008), Surface Characteristics of Observed Cold Pools, *Mon. Weather Rev.*, *136*(12), 4839–4849.

Fan, J., T. Yuan, J. M. Comstock, S. Ghan, A. Khain, L. R. Leung, Z. Li, V. J. Martins, and M. Ovchinnikov (2009), Dominant role by vertical wind shear in regulating aerosol effects on deep convective clouds, *J. Geophys. Res.*, *114*(D22), D22206.

Fan, J., Y. Liu, K. Xu, K. North, S. Collis, X. Dong, G. J. Zhang, Q. Chen, P. Kollias, and S. J. Ghan (2015), Improving representation of convective transport for scale-aware parameterization: 1. Convection and cloud properties simulated with spectral bin and bulk microphysics: CRM Model Evaluation, *J. Geophys. Res.*, *120*(8), 3485–3509.

Feng, Z., X. Dong, B. Xi, C. Schumacher, P. Minnis, and M. Khaiyer (2011), Top-of-atmosphere radiation budget of convective core/stratiform rain and anvil clouds from deep convective systems, *J. Geophys. Res.*, *116*(D23), D23202.

Fovell, R. G., and Y. Ogura (1988), Numerical Simulation of a Midlatitude Squall Line in Two Dimensions, *J. Atmos. Sci.*, *45*(24), 3846–3879.

Fridlind, A. M. et al. (2004), Evidence for the predominance of mid-tropospheric aerosols as subtropical anvil cloud nuclei., *Science*, *304*(5671), 718–22.

Fritsch, J. M., and R. E. Carbone (2004), Improving quantitative precipitation forecasts in the warm season: A USWRP research and development strategy, *Bull. Am. Meteorol. Soc.*, *85*(7), 955–965.

Fritsch, J. M., and G. S. Forbes (2001), Mesoscale convective systems, *Meteorol. Monogr.*, 28, 323–357.

Fritsch, J. M., R. J. Kane, and C. R. Chelius (1986), The Contribution of Mesoscale Convective Weather Systems to the Warm-Season Precipitation in the United States, *J. Clim. Appl. Meteorol.*, *25*(10), 1333–1345.

Fritsch, J. M., J. D. Murphy, and J. S. Kain (1994), Warm Core Vortex Amplification over Land, *J. Atmos. Sci.*, *51*(13), 1780–1807.

Futyan, J. M., and A. D. Del Genio (2007), Deep Convective System Evolution over Africa and the Tropical Atlantic, *J. Clim.*, *20*(20), 5041–5060.

Gallus, W. A., and R. H. Johnson (1991), Heat and Moisture Budgets of an Intense Midlatitude Squall Line, *J. Atmos. Sci.*, *48*(1), 122–146.

Gebhart, K. A, S. M. Kreidenweis, and W. C. Malm (2001), Back-trajectory analyses of fine particulate matter measured at Big Bend National Park in the historical database and the 1996 scoping study, *Sci. Total Environ.*, *276*(1-3), 185–204.

Davis, C. A., K. W. Manning, R. E. Carbone, S. B. Trier, and J. D. Tuttle (2003), Coherence of Warm-Season Continental Rainfall in Numerical Weather Prediction Models, *Mon. Weather Rev.*, *131*(11), 2667–2679.

Del Genio, A. D., J. Wu, and Y. Chen (2012), Characteristics of Mesoscale Organization in WRF Simulations of Convection during TWP-ICE, *J. Clim.*, *25*(17), 5666–5688.

Gregory, D. (2001), Estimation of entrainment rate in simple models of convective clouds, *Q. J. R. Meteorol. Soc.*, *127*(571), 53–72.

Grim, J. A., G. M. McFarquhar, R. M. Rauber, A. M. Smith, and B. F. Jewett (2009), Microphysical and Thermodynamic Structure and Evolution of the Trailing Stratiform Regions of Mesoscale Convective Systems during BAMEX. Part II: Column Model Simulations, *Mon. Weather Rev.*, *137*(4), 1186–1205.

Hamilton, D. W., Y.-L. Lin, R. P. Weglarz, and M. L. Kaplan (1998), Jetlet Formation from Diabatic Forcing with Applications to the 1994 Palm Sunday Tornado Outbreak, *Mon. Weather Rev.*, *126*(8), 2061–2089.

Harrington, J. Y. (1997), The effects of radiative and microphysical processes on simulated warm and transition season artic stratus, Ph.D. Dissertation, Colorado State University, 289 pp.

Hartmann, D. L., H. H. Hendon, and R. A. Houze (1984), Some Implications of the Mesoscale Circulations in Tropical Cloud Clusters for Large-Scale Dynamics and Climate, *J. Atmos. Sci.*, *41*(1), 113–121.

Heymsfield, A. J., A. Bansemer, M. R. Poellot, and N. Wood (2015), Observations of Ice Microphysics through the Melting Layer, *J. Atmos. Sci.*, *72*(8), 2902–2928.

Holben, B. N. et al. (1998), AERONET—A Federated Instrument Network and Data Archive for Aerosol Characterization, *Remote Sens. Environ.*, *66*(1), 1–16.

Hou, A. Y., R. K. Kakar, S. Neeck, A. A. Azarbarzin, C. D. Kummerow, M. Kojima, R. Oki, K. Nakamura, and T. Iguchi (2014), The Global Precipitation Measurement Mission, *Bull. Am. Meteorol. Soc.*, *95*(5), 701–722.

Houze, R. A. (1977), Structure and Dynamics of a Tropical Squall–Line System, *Mon. Weather Rev.*, *105*(12), 1540–1567.

Houze, R. A. (2004), Mesoscale convective systems, *Rev. Geophys.*, *42*(4), RG4003.

Houze, R. A., B. F. Smull, and P. Dodge (1990), Mesoscale Organization of Springtime Rainstorms in Oklahoma, *Mon. Weather Rev.*, *118*(3), 613–654.

Intergovernmental Panel on Climate Change (IPCC) (2007), Climate Change: The Physical Science Basis, edited by S. Solomon et al., 996 pp., Cambridge Univ. Press, Cambridge, U. K.

Jensen, M. P. et al. (2015), The Midlatitude Continental Convective Clouds Experiment (MC3E), *Bull. Am. Meteorol. Soc.*, 151221073208006.

Johnson, R. H., and G. S. Young (1983), Heat and Moisture Budgets of Tropical Mesoscale Anvil Clouds, *J. Atmos. Sci.*, *40*(9), 2138–2147.

Kain, J., and J. M. Fritsch (1993), Convective Parameterization for Mesoscale Models: The Kain-Fritsch Scheme, in *The Representation of Cumulus Convection in Numerical Models SE - 16*, edited by K. Emanuel and D. Raymond, pp. 165–170, American Meteorological Society.

Khain, A. P., N. BenMoshe, and A. Pokrovsky (2008), Factors Determining the Impact of Aerosols on Surface Precipitation from Clouds: An Attempt at Classification, *J. Atmos. Sci.*, *65*(6), 1721–1748.

Khain, A., D. Rosenfeld, and A. Pokrovsky (2005), Aerosol impact on the dynamics and microphysics of deep convective clouds, *Q. J. R. Meteorol. Soc.*, *131*(611), 2639–2663.

Klemp, J. B., and R. B. Wilhelmson (1978), The Simulation of Three-Dimensional Convective Storm Dynamics, *J. Atmos. Sci.*, *35*(6), 1070–1096.

Koch, D., and A. D. Del Genio (2010), Black carbon semi-direct effects on cloud cover: review and synthesis, *Atmos. Chem. Phys.*, *10*(16), 7685–7696.

Kunkel, K. E., S. A. Changnon, and J. R. Angel (1994), Climatic Aspects of the 1993 Upper Mississippi River Basin Flood, *Bull. Am. Meteorol. Soc.*, *75*(5), 811–822.

Kuo, Y.-H., and R. A. Anthes (1984), Mesoscale Budgets of Heat and Moisture in a Convective System over the Central United States, *Mon. Weather Rev.*, *112*(8), 1482–1497.

Lang, S. E., W.-K. Tao, J.-D. Chern, D. Wu, and X. Li (2014), Benefits of a Fourth Ice Class in the Simulated Radar Reflectivities of Convective Systems Using a Bulk Microphysics Scheme, *J. Atmos. Sci.*, *71*(10), 3583–3612.

Leary, C. A., and R. A. Houze (1979), Melting and Evaporation of Hydrometeors in Precipitation from the Anvil Clouds of Deep Tropical Convection, *J. Atmos. Sci.*, *36*(4), 669–679.

Lebo, Z. J. (2014), The Sensitivity of a Numerically Simulated Idealized Squall Line to the Vertical Distribution of Aerosols, *J. Atmos. Sci.*, *71*(12), 4581–4596.

Lebo, Z. J., and H. Morrison (2014), Dynamical Effects of Aerosol Perturbations on Simulated Idealized Squall Lines, *Mon. Weather Rev.*, *142*(3), 991–1009.

Lee, S. S., L. J. Donner, V. T. J. Phillips, and Y. Ming (2008), Examination of aerosol effects on precipitation in deep convective clouds during the 1997 ARM summer experiment, *Q. J. R. Meteorol. Soc.*, *134*(634), 1201–1220.

Li, G., Y. Wang, K.-H. Lee, Y. Diao, and R. Zhang (2009), Impacts of aerosols on the development and precipitation of a mesoscale squall line, *J. Geophys. Res.*, *114*(D17), D17205.

Lin, Y., and K. E. Mitchell (2005), The NCEP Stage II/IV hourly precipitation analyses: development and applications, *Prepr. 19th Conf. Hydrol. Am. Meteorol. Soc. San Diego, CA, 9-13 January 2005, Pap. 1.2*, 2–5.

Liu, Y., J. Fan, G. J. Zhang, K. Xu, and S. J. Ghan (2015), Improving representation of convective transport for scale-aware parameterization: 2. Analysis of cloud-resolving model simulations, *J. Geophys. Res.*, *120*(8), 3510–3532.

Lohmann, U., J. Feichter, C. C. Chuang, and J. E. Penner (1999), Prediction of the number of cloud droplets in the ECHAM GCM, *J. Geophys. Res.*, *104*(D8), 9169.

Lyons, W. A. (1998), Enhanced Positive Cloud-to-Ground Lightning in Thunderstorms Ingesting Smoke from Fires, *Science*, *282*(5386), 77–80.

Mapes, B. E. (1993), Gregarious Tropical Convection, *J. Atmos. Sci.*, *50*(13), 2026–2037.

McFarquhar, G. M., M. S. Timlin, R. M. Rauber, B. F. Jewett, J. A. Grim, and D. P. Jorgensen (2007), Vertical Variability of Cloud Hydrometeors in the Stratiform Region of Mesoscale Convective Systems and Bow Echoes, *Mon. Weather Rev.*, *135*(10), 3405–3428.

McGee, C. J., and S. C. van den Heever (2014), Latent Heating and Mixing due to Entrainment in Tropical Deep Convection, *J. Atmos. Sci.*, *71*(2010), 816–832.

Mellor, G. L., and T. Yamada (1974), A Hierarchy of Turbulence Closure Models for Planetary Boundary Layers, *J. Atmos. Sci.*, *31*(7), 1791–1806

Mesinger, F., and A. Arakawa (1976), Numerical methods used in atmospheric models, volume 1, in *Global Atmospheric Research Program World Meteorological Organization, Geneva (Switzerland).*, Vol. 1.

Meyers, M. P., R. L. Walko, J. Y. Harrington, and W. R. Cotton (1997), New RAMS cloud microphysics parameterization. Part II: The two-moment scheme, *Atmos. Res.*, *45*(1), 3–39.

Morrison, H., G. Thompson, and V. Tatarskii (2009), Impact of Cloud Microphysics on the Development of Trailing Stratiform Precipitation in a Simulated Squall Line: Comparison of One- and Two-Moment Schemes, *Mon. Weather Rev.*, *137*(3), 991–1007.

Murray, N. D., R. E. Orville, and G. R. Huffines (2000), Effect of pollution from Central American fires on cloud-to-ground lightning in May 1998, *Geophys. Res. Lett.*, *27*(15), 2249–2252.

Nicholls, M. E., R. A. Pielke, and W. R. Cotton (1991), Thermally Forced Gravity Waves in an Atmosphere at Rest, *J. Atmos. Sci.*, *48*(16), 1869–1884.

Olsson, P. Q., and W. R. Cotton (1997), Balanced and Unbalanced Circulations in a Primitive Equation Simulation of a Midlatitude MCC. Part II: Analysis of Balance, *J. Atmos. Sci.*, *54*(4), 479–497.

Pandya, R. E., and D. R. Durran (1996), The Influence of Convectively Generated Thermal Forcing on the Mesoscale Circulation around Squall Lines, *J. Atmos. Sci.*, *53*(20), 2924–2951.

Park, M.-S., and R. L. Elsberry (2013), Latent Heating and Cooling Rates in Developing and Nondeveloping Tropical Disturbances during TCS-08: TRMM PR versus ELDORA Retrievals*, *J. Atmos. Sci.*, *70*(1), 15–35.

Parker, M. D., and R. H. Johnson (2000), Organizational Modes of Midlatitude Mesoscale Convective Systems, *Mon. Weather Rev.*, *128*(10), 3413–3436.

Peppler, R. A. et al. (2000), ARM Southern Great Plains Site Observations of the Smoke Pall Associated with the 1998 Central American Fires, *Bull. Am. Meteorol. Soc.*, *81*(11), 2563–2591.

Pielke, R. A. et al. (1992), A comprehensive meteorological modeling system – RAMS, *Meteorol. Atmos. Phys.*, *49*(1-4), 69–91.

Prospero, J. M., and P. J. Lamb (2003), African Droughts and Dust Transport to the Caribbean: Climate Change Implications, *Science*, *302*(5647), 1024–1027.

Randall, D., M. Khairoutdinov, A. Arakawa, and W. Grabowski (2003), Breaking the Cloud Parameterization Deadlock, *Bull. Am. Meteorol. Soc.*, *84*(11), 1547–1564.

Raymond, D. J. (1984), A Wave-CISK Model of Squall Lines, *J. Atmos. Sci.*, *41*(12), 1946–1958.

Raymond, D. J., and H. Jiang (1990), A Theory for Long-Lived Mesoscale Convective Systems, *J. Atmos. Sci.*, *47*(24), 3067–3077.

Rodwell, M. J. et al. (2013), Characteristics of Occasional Poor Medium-Range Weather Forecasts for Europe, *Bull. Am. Meteorol. Soc.*, *94*(9), 1393–1405.

Rogers, C. M., and K. P. Bowman (2001), Transport of smoke from the Central American fires of 1998, *J. Geophys. Res.*, *106*(D22), 28357–28368.

Rogers, R. F., and J. M. Fritsch (2001), Surface Cyclogenesis from Convectively Driven Amplification of Midlevel Mesoscale Convective Vortices, *Mon. Weather Rev.*, *129*(4), 605–637.

Rutledge, S. A., and R. A. Houze (1987), A Diagnostic Modeling Study of the Trailing Stratiform Region of a Midlatitude Squall Line, *J. Atmos. Sci.*, *44*(18), 2640–2656.

Saide, P. E., S. N. Spak, R. B. Pierce, J. A. Otkin, T. K. Schaack, A. K. Heidinger, A. M. da Silva, M. Kacenelenbogen, J. Redemann, and G. R. Carmichael (2015), Central American biomass burning smoke can increase tornado severity in the U.S., *Geophys. Res. Lett.*, *42*(3), 956–965.

Saleeby, S. M., and W. R. Cotton (2004), A Large-Droplet Mode and Prognostic Number Concentration of Cloud Droplets in the Colorado State University Regional Atmospheric Modeling System (RAMS). Part I: Module Descriptions and Supercell Test Simulations, *J. Appl. Meteorol.*, *43*(1), 182–195.

Saleeby, S. M., and S. C. van den Heever (2013), Developments in the CSU-RAMS Aerosol Model: Emissions, Nucleation, Regeneration, Deposition, and Radiation, *J. Appl. Meteorol. Climatol.*, *52*(12), 2601–2622.

Satoh, M., T. Matsuno, H. Tomita, H. Miura, T. Nasuno, and S. Iga (2008), Nonhydrostatic icosahedral atmospheric model (NICAM) for global cloud resolving simulations, *J. Comput. Phys.*, *227*(7), 3486–3514.

Schlemmer, L., and C. Hohenegger (2015), Modifications of the atmospheric moisture field as a result of cold-pool dynamics, *Q. J. R. Meteorol. Soc.*, *142*(694), 30–42.

Schumacher, C., R. A. Houze, and I. Kraucunas (2004), The Tropical Dynamical Response to Latent Heating Estimates Derived from the TRMM Precipitation Radar, *J. Atmos. Sci.*, *61*(12), 1341–1358.

Schumacher, R. S., and R. H. Johnson (2005), Organization and Environmental Properties of Extreme-Rain-Producing Mesoscale Convective Systems, *Mon. Weather Rev.*, *133*(4), 961–976.

Seigel, R. B., and S. C. van den Heever (2013), Squall-Line Intensification via Hydrometeor Recirculation, *J. Atmos. Sci.*, *70*(7), 2012–2031.

Seigel, R. B., S. C. van den Heever, and S. M. Saleeby (2013), Mineral dust indirect effects and cloud radiative feedbacks of a simulated idealized nocturnal squall line, *Atmos. Chem. Phys.*, *13*(8), 4467–4485.

Shige, S., Y. N. Takayabu, S. Kida, W.-K. Tao, X. Zeng, C. Yokoyama, and T. L'Ecuyer (2009), Spectral retrieval of latent heating profiles from TRMM PR data. Part IV: comparisons of lookup tables from two-and three-dimensional cloud-resolving model simulations, *J. Clim.*, *22*(20), 5577–5594.

Simpson, J., R. F. Adler, and G. R. North (1988), A Proposed Tropical Rainfall Measuring Mission (TRMM) Satellite, *Bull. Am. Meteorol. Soc.*, *69*(3), 278–295.

Smagorinsky, J. (1963), General Circulation Experiments with the Primitive Equations I. The Basic Experiment, *Mon. Weather Rev.*, *91*(3), 99–164.

Smull, B. F., and R. A. Houze (1985), A Midlatitude Squall Line with a Trailing Region of Stratiform Rain: Radar and Satellite Observations, *Mon. Weather Rev.*, *113*(1), 117–133.

Steiner, M., R. A. Houze, and S. E. Yuter (1995), Climatological Characterization of Three-Dimensional Storm Structure from Operational Radar and Rain Gauge Data, *J. Appl. Meteorol.*, *34*(9), 1978–2007.

Stensrud, D. J., and J. L. Anderson (2001), Is Midlatitude Convection an Active or a Passive Player in Producing Global Circulation Patterns?, *J. Clim.*, *14*(10), 2222–2237.

Stevenson, S. N., and R. S. Schumacher (2014), A 10-Year Survey of Extreme Rainfall Events in the Central and Eastern United States Using Gridded Multisensor Precipitation Analyses, *Mon. Weather Rev.*, *142*(9), 3147–3162.

Storer, R. L., S. C. van den Heever, and G. L. Stephens (2010), Modeling Aerosol Impacts on Convective Storms in Different Environments, *J. Atmos. Sci.*, *67*(12), 3904–3915.

Tao, W., J. Chen, Z. Li, C. Wang, and C. Zhang (2012), Impact of aerosols on convective clouds and precipitation, *Rev. Geophys.*, *50*(2), RG2001.

Tao, W.-K., J. Simpson, C. H. Sui, B. Ferrier, S. Lang, J. Scala, M. D. Chou, and K. Pickering (1993), Heating, Moisture, and Water Budgets of Tropical and Midlatitude Squall Lines: Comparisons and Sensitivity to Longwave Radiation, *J. Atmos. Sci.*, *50*(5), 673–690.

Tao, W.-K. et al. (2006), Retrieval of Latent Heating from TRMM Measurements, *Bull. Am. Meteorol. Soc.*, *87*(11), 1555–1572.

Tao, W.-K., X. Li, A. Khain, T. Matsui, S. Lang, and J. Simpson (2007), Role of atmospheric aerosol concentration on deep convective precipitation: Cloud-resolving model simulations, *J. Geophys. Res.*, *112*(D24), D24S18.

Tao, W.-K., D. Wu, T. Matsui, C. Peters-Lidard, S. Lang, A. Hou, M. Rienecker, W. Petersen, and M. Jensen (2013), Precipitation intensity and variation during MC3E: A numerical modeling study, *J. Geophys. Res.*, *118*(13), 7199–7218.

Tollerud, E. I., and R. S. Collander (1993), A ten year summary of severe weather in mesoscale convective complexes, *Preprints, 17th Conf. on Severe Local Storms,* St. Louis, MO, Amer. Meteor. Soc., 533–537.

Trier, S. B., C. A. Davis, D. A. Ahijevych, M. L. Weisman, and G. H. Bryan (2006), Mechanisms Supporting Long-Lived Episodes of Propagating Nocturnal Convection within a 7-Day WRF Model Simulation, *J. Atmos. Sci.*, *63*(10), 2437–2461.

Varble, A., E. J. Zipser, A. M. Fridlind, P. Zhu, A. S. Ackerman, J. Chaboureau, S. Collis, J. Fan, A. Hill, and B. Shipway (2014), Evaluation of cloud-resolving and limited area model intercomparison simulations using TWP-ICE observations: 1. Deep convective updraft properties, *J. Geophys. Res.*, *119*(24), 13,891–13,918.

Wakimoto, R. M. (1982), The Life Cycle of Thunderstorm Gust Fronts as Viewed with Doppler Radar and Rawinsonde Data, *Mon. Weather Rev.*, *110*(8), 1060–1082.

Walko, R. L. et al. (2000), Coupled Atmosphere–Biophysics–Hydrology Models for Environmental Modeling, *J. Appl. Meteorol.*, *39*(6), 931–944.

Wang, C. (2005), A modeling study of the response of tropical deep convection to the increase of cloud condensation nuclei concentration: 1. Dynamics and microphysics, *J. Geophys. Res.*, *110*(21), 1–16.

Wang, J., S. A. Christopher, U. S. Nair, J. S. Reid, E. M. Prins, J. Szykman, and J. L. Hand (2006), Mesoscale modeling of Central American smoke transport to the United States: 1. "Top-down" assessment of emission strength and diurnal variation impacts, *J. Geophys. Res.*, *111*(D5), D05S17.

Wang, J., S. C. van den Heever, and J. S. Reid (2009), A conceptual model for the link between Central American biomass burning aerosols and severe weather over the south central United States, *Environ. Res. Lett.*, *4*(1), 015003.

Watson, A. I., J. Meitín, and J. B. Cunning (1988), Evolution of the Kinematic Structure and Precipitation Characteristics of a Mesoscale Convective System on 20,May 1979, *Mon. Weather Rev.*, *116*(8), 1555–1567.

Witek, M. L., P. J. Flatau, P. K. Quinn, and D. L. Westphal (2007), Global sea-salt modeling: Results and validation against multicampaign shipboard measurements, *J. Geophys. Res.*, *112*(8), 1–14.

Wolf, B. J., and D. R. Johnson (1995), The Mesoscale Forcing of a Midlatitude Upper-Tropospheric Jet Streak by a Simulated Convective System. Part I: Mass Circulation and Ageostrophic Processes, *Mon. Weather Rev.*, *123*(4), 1059–1087.

Yanai, M., S. Esbensen, and J.-H. Chu (1973), Determination of Bulk Properties of Tropical Cloud Clusters from Large-Scale Heat and Moisture Budgets, *J. Atmos. Sci.*, *30*(4), 611–627.

Yuter, S. E., and R. A. Houze (1995), Three-Dimensional Kinematic and Microphysical Evolution of Florida Cumulonimbus. Part II: Frequency Distributions of Vertical Velocity, Reflectivity, and Differential Reflectivity, *Mon. Weather Rev.*, *123*(7), 1941–1963.

Zhang, D.-L., and J. M. Fritsch (1987), Numerical Simulation of the Meso-β Scale Structure and Evolution of the 1977 Johnstown Flood. Part II: Inertially Stable Warm-Core Vortex and the Mesoscale Convective Complex, *J. Atmos. Sci.*, *44*(18), 2593–2612.

Zhang, G. J., and X. Song (2009), Interaction of deep and shallow convection is key to Madden-Julian Oscillation simulation, *Geophys. Res. Lett.*, *36*(9), 1–6.